Coherent X-ray diffraction imaging and ptychography on silicon-on-insulator nanostructures

A Dissertation

Presented to the Department of Physics and Astronomy
of University College London

in Partial Fulfillment of the Requirements for the Degree of
Doctor of Philosophy

By

Xiaowen Shi

BSc. University College London

M.Phil University of Cambridge

Supervisor: **Prof. Ian Robinson** (UCL Department of Physics and Astronomy & London Centre for Nanotechnology)

Second Supervisor: **Dr. Paul Warburton** (UCL Department of Electrical Engineering & London Centre for Nanotechnology)

DECLARATION

I, Xiaowen Shi, confirm that the work presented in this dissertation is my own. Where information has been derived from other sources, I confirm that this has been indicated in the dissertation.

Xiaowen Shi (石晓雯), 13th of December 2012

To my dear Father, Mother and all my friends (Jing Qiu, Gihan Weerasinghe, Jonathan Payne, Huan Wang, Zhenxing Feng etc.) who accompany me and help me through the most exciting period of my academic life. Thank you all for being there.

Abstract

My PhD project is on the use of coherent X-ray diffractive imaging (CDI) techniques to study strained Silicon-On-Insulator (SOI) and Strained-Silicon-On-Insulator (SSOI) nanostructures, which include nanowires and micro-squares. To understand and distinguish SOI wafer properties and compare and analyze different wafer bonding techniques, various SOI wafers with different bonding techniques were measured using CDI, and analysis shows inhomogeneity across all categories of SOI wafers. Furthermore, I discovered a radiation-induced bending effect causing SOI nanowires to exhibit highly strained characteristics in diffraction patterns in reciprocal-space. There is a trend of peak splitting of the central maximum of the diffraction patterns when increasing X-ray illumination dose, i.e. time of X-ray exposure. We are able to propose a model of radiation-induced bending of SOI model and our model is confirmed by simulations of calculated diffraction patterns and by a Finite-Element-Analysis tool (COMSOL Multiphysics). The results are in agreement with experimental measurements, which indicates that our model is a generally correct description of the X-ray radiation effect. We developed a Guided-Phase-Error-Reduction (GPER) algorithm to do diffraction data inversion, obtaining direct-space amplitude and phase of strong-bent SOI nanowires. Most importantly, we observe mechanical breakdown that causes various kinds of dislocations within the nanowire structure when the X-ray irradiation dose has reached a certain level. Beyond this dose, the nanowire begins to undergo plastic deformation.

The second part of my PhD project involves design and performance of experimental measurements of reflection Bragg-geometry ptychography at beamline 34-ID-C at the Advanced Photon Source. We have used both KB mirrors and zone-plate focused methods. Zone-plate based focusing method produces highly asymmetric curved-wave front X-ray illumination for studies on both Siemens-star test patterns and SOI micro- and nano squares. Our preliminary analyses have shown some promising results. We have performed series of measurements on Siemens-star test sample by using transmission-geometry Ptychography with various coherence properties of X-rays and oversampling ratios of Fourier-space diffraction intensities. In the long term, Bragg-geometry ptychography has great potential for imaging condensed matter structures and surface effects, aiming at better understanding of structural Physics, Materials sciences and Nanotechnology in general. Strains by various industrial processing of SOI based electronic devices, such as silicon-based MOSFETs, can be probed by either conventional Bragg CDI or Bragg-geometry ptychography. MOSFETs may behave differently under X-ray irradiation, because of this radiation effect, resulting to various strain states which could modify carriers mobility in semiconductor devices performance in general applications.

Acknowledgement

First, I would like to thank Prof. Ian K Robinson for his generous advises and help throughout my PhD, much of the work would not have been possible without his invaluable guidance and suggestions.

Secondly, I would like to thank my UCL research group (Fucai Zhang, Gang Xiong, Xiaojing Huang, Graeme Morrison, Jesse Clark, Mohammed Yusuf, Ana Estandarte, Nicolas Burdet, Bo Chen, Loren Beitra, Maria Civita, Laura Shemilt, Marianne Monteforte, Joerg Schwenke, Christophe Lynch, John Rodenburg and Malcolm Howells etc.) for providing excellent working and social environments, without which, much of the academic and philosophical inspirations would not have been possible.

Finally, I would thank scientists from other research groups, Paul Warburton, Tony Harker, Dorothy Duffy, Ana Sofia Vila Verde, Angie Ma, Isaac Peterson, Ian McNulty, Ross Harder, David Vine, Joan Vila-Comamala, Brian Abbey, Samuel Flewett and Zheng Gu etc. for their contributions to my work. My work would not have been productive without them, and they have provided help and suggestions in various fields of Physics and Engineering.

Table of Contents

TABLE OF FIGURES

1 Scientific applications of X-ray coherence

1.1 Introduction to Coherent X-ray Diffractive Imaging

Coherent X-ray Diffractive Imaging (CDI)[1-5], especially using phase-contrast, is one of the strongest contenders for investigating internal structures (both atomic density and displacement of atoms) of nano-crystalline materials. More conventional imaging techniques such as Transmission Electron Microscopy (TEM) can only probe very thin cross-sections of the specimen under study[6]. Any internal stresses could possibly be removed when samples are cross-sectioned to produce thin lamellar sections. On the contrary, with CDI, we can probe the 3-dimensional internal structure of entire samples without sectioning, which damages the internal strains and is required for imaging in high-resolution microscopes.

The Coherent X-ray diffractive imaging technique has better reconstructed real-space resolution, presently around 30nm, than direct real-space X-ray imaging methods because of the inversion procedure used for the reciprocal-space diffraction patterns. To be able to image structures in reciprocal-space, coherent diffractive imaging, in both hard X-ray and visible light, is expected to offer at least a factor of three better spatial resolution than than its traditional X-ray imaging counterpart such as Transmission X-ray Microscopy[7,8]. In theory it can reach sub-atomic resolution, and the technique is diffraction limited. Bragg CDI is able to investigate strains, seen as atomic displacements (from the ideal atomic position in a crystal lattice) of blocks of material with dimensions of 10nm to 1μm.

It allows measurements of strains of individual regions while most diffraction techniques obtain results by averaging arrays of similar structures[9]. Fig. 1 shows some typical frames of 3D rocking diffraction patterns of nano-crystals; interference fringes can be clearly observed when nano-crystals are smaller than the X-ray beam size. The visibility of interference fringes is related to the general coherence properties of X-rays. Fig. 2 illustrates a nice example of amplitude and phase reconstructions of coherent diffraction patterns of lead nano-particle by using appropriate CDI algorithms.

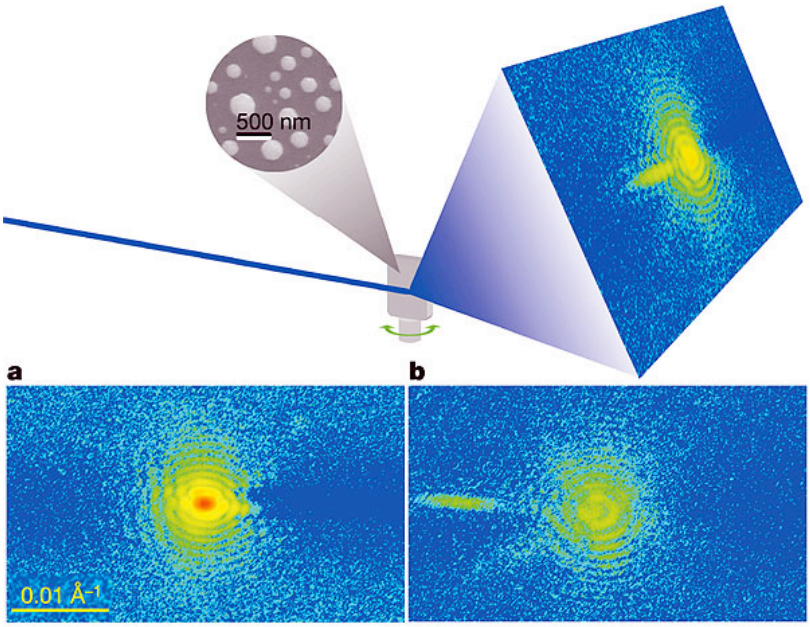

Figure 1 Image is from[4] Typical CDI experimental measurements of Pb nanoparticles, a and b images are two frames of the 3D rocking data frame collection, with scale-bar shown here representing the reciprocal-space lattice vector.

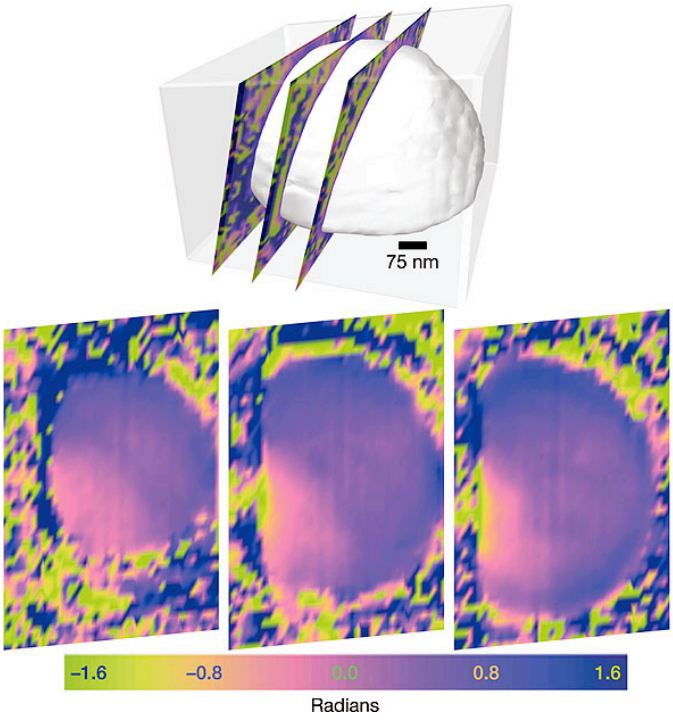

Figure 2 Image is from[4] reconstructed amplitude and phase of typical diffraction intensities of Pb nanoparticles by using iterative algorithms.

1:2 Coherence

Conventional X-ray diffraction with low degree of coherence is used to study specimen of highly crystalline structures. With introduction of X-ray studies with high coherence properties, specimen of non-crystalline or semi-crystalline kind can be also studied through interference patterns. These samples give speckled diffraction patterns and in principle could be inverted if necessary data acquisition and experimental conditions are to be met.

Coherence function of an X-ray beam can be regarded to be a multi-dimensional entity, with longitudinal and transverse coherence lengths defined as follows:

$$\xi_L = \frac{\lambda^2}{2\Delta\lambda}$$ [10] **Equation 1**

$$\xi_T = \frac{\lambda R}{2\sigma_{x,y}}$$ [10] **Equation 2**

Where λ is the wavelength of incident X-ray and Δλ is the difference in wavelength between different incident waves, and $\sigma_{x,y}$ is the finite source sizes of accelerated electrons from which synchrotron X-rays are produced, R being the distance the incident X-ray travels and it is considered that $R \gg \sigma_{x,y}$. Coherence length is regarded as the length at which two incident X-ray waves are just completely out of phase, i.e. out-of-phase by $\frac{\pi}{2}$. Longitudinal and transverse coherence lengths were measured to be $\xi_L = 0.66 \pm 0.22\,\mu\text{m}$ [11], but the transverse coherence length is significantly longer and it is estimated to be around 50 to 100μm at beamline 34-ID-C at the Advanced Photon Source (APS). The mutual coherence function (MCF) of the electric field is generally defined as:

$$\Gamma(\rho_1, \rho_2, \tau) = \left\langle \mathrm{E}(\rho_1, t)\mathrm{E}^*(\rho_2, t+\tau) \right\rangle$$ **Equation 3**

And the normalized mutual coherence function is usually described as the follows;

$$\gamma(\rho_1,\rho_2,\tau)=\frac{\langle \mathrm{E}(\rho_1,t)\mathrm{E}^*(\rho_2,t+\tau)\rangle}{\sqrt{\langle \mathrm{I}(\rho_1,t)\rangle}\langle \mathrm{I}(\rho_2,t)\rangle} \quad \text{Equation 4}$$

ρ_1 and ρ_2 are position vectors of two points at a particular wave front in which two points are located. $\mathrm{E}(\rho_1,t)$ and $\mathrm{E}^*(\rho_2,t+\tau)$ are electromagnetic fields at these two points which are separated by a specific time interval of τ, after some time t in the initial starting point of measurement. $\langle \mathrm{I}(\rho_1,t)\rangle$ and $\langle \mathrm{I}(\rho_2,t)\rangle$ are expectation values of intensity of electromagnetic field at these two points in the wave front. The value $\gamma(\rho_1,\rho_2,\tau)$ can be between 0 and 1, with value of 0 being complete incoherence and being 1 being complete coherence, which means any values of $\gamma(\rho_1,\rho_2,\tau)$ being between 0 and 1 indicate that the X-ray source is partially coherent. With this definition of mutual coherence function (MCF), one can calculate electromagnetic field strength at the second point at a particular wave front in the incoming X-ray source whenever the illumination is fully coherent, and in contrast, no information can be deduced on the electromagnetic field strength of the second point if the source is completely incoherent ($\gamma(\rho_1,\rho_2,\tau)$ is 0).

A recent review has indicated that the coherence properties of X-rays cannot be compared with those of visible light, i.e. laser, therefore limited coherence length results to partial coherence measurements and the possible effect of partial coherence properties

to CDI measurements[12]. By taking partial coherence effects into account, CDI reconstructions of gold nano-crystals can be improved by using approximate modified modulus projection/constraint operation with introduction of partial coherent function of X-rays. Multi-dimensional coherent functions of X-rays[13] in a sense indicate that there is a somewhat coherent property in all three spatial dimensions, i.e. there is an extra coherence length in the 3rd dimension, which differs from its longitudinal and transverse parts of coherence dimensions. Clark[12] has demonstrated the existence of this extra dimension of X-ray coherent function experimentally, which is explained in greater details in chapter 2.6, and the 3D partial coherence function is Gaussian-like as predicted by Nugent[13]. However, further experiments are needed to determine this extra dimension of the coherence function. One way to measure coherence function of X-ray is the Young's double-slit experiment with measurements of visibility of fringes in reciprocal-space as a function of slit separation, recent results shows such measurements by using the hard X-ray free electron laser at Linac Coherent Light Source (LCLS) at Stanford[14]. The estimation of coherence length comes from the slit separation for which the visibility of fringes in the measured diffraction patterns reduced to a standard value of e^{-1} of that of full visibility level with total coherence.

To describe electromagnetic wave propagation statistically, one needs to have generalized picture of coherence properties of propagating electromagnetic wave. Electromagnetic waves can be illustrated as single-mode or multi-mode, in either the

frequency domain or the spatial domain. For multi-mode wavefields in the frequency domain, which is usually called pink-beam wavefields, the wavefields are composed of coherent waves with multiple wavelengths with particular spectrum distribution. Several studies on pink-beam Coherent X-ray diffraction imaging have been reported and comparison between pink-beam CDI and conventional monochromatic CDI has been investigated. The other multi-mode wavefields are composed in the spatial domain, in which partially coherent X-ray wavefields are expressed with a generalized form of Mercer's Theorem as Hermitian functions of the form:

$$W(r_1, r_2, \omega) = \sum_n \alpha_n(\omega) \psi_n(r_1, \omega) \psi_n^*(r_2, \omega) \quad \text{Equation 5}$$

where $\alpha_n(\omega)$ and $\psi_n(r_1, \omega)$ are eigenvalues and eigen-functions of the generalized Hermitian function $W(r_1, r_2, \omega)$, where the eigenvalues illustrated here may represent occupancy numbers of associated optical mode. These eigenvalues, i.e. the optical modes are also solutions of Helmholtz differential equation and Fredholm integral equation.

The pink-beam modal formulation represents the wavefields as a superposition of spectral/temporal modes, in the direction of propagation of the wavefields, in both cases, temporal and spatial modal compositions, the overall intensity of propagating electromagnetic wavefields is a superposition of individual components of modal intensity, not amplitude, because they are considered incoherent.

For electromagnetic wavefields with full degree of coherence, one can relate the phase of the fully coherent complex wavefields to its Fourier Transform diffraction intensity distribution by introduction of transport of intensity equation in the following way[15]:

$$\nabla_{\perp}.\{\mathrm{I}_n(\mathrm{r}_{\perp},z)\,\nabla_{\perp}\phi_n(\mathrm{r}_{\perp},z)\ \}=-\mathrm{k}\frac{\mathrm{dI}_n(\mathrm{r}_{\perp},z)}{\mathrm{dz}} \quad \textbf{Equation 6}$$

where $\frac{\mathrm{dI}_n(\mathrm{r}_{\perp},z)}{\mathrm{dz}}$ is the derivative of the associated intensity distribution, $\mathrm{I}_n(\mathrm{r}_{\perp},z)$ is the intensity distribution, and $\phi_n(\mathrm{r}_{\perp},\mathrm{z})$ is the associated phase distribution.

The expression of transport of intensity equation can be expressed as a multi-modal ensemble, similar to modal expansion introduced in the expression of propagating of partially coherent electromagnetic wavefields.

$$\sum_k \alpha_k \left\{\nabla_{\perp}.\mathrm{I}_k(\mathrm{r}_{\perp},z)+k\frac{\mathrm{dI}_k(\mathrm{r}_{\perp},z)}{\mathrm{dz}}\right\}=0 \quad \textbf{Equation 7}$$

In order to fully solve this model-dependent mutual optical intensity equation, one has to consider all associated modes separately, which is difficult because the information obtained through diffraction intensity only exhibits averaged information. To understand the transport of intensity equation in an averaged approach, one needs to define a quantity

that is associated with magnitude and direction of flow of energy in the wavefield, the Poynting vector, of a quasi-monochromatic wavefield:

$$S(r)=\frac{1}{k}\mathrm{I}(r)\nabla\phi(r) \quad \textbf{Equation 8}$$

Due to conservation of energy theorem, the divergence of Poynting vector should be zero.

For partially coherent electromagnetic wavefields, an averaged Poynting vector needs to be defined, and the corresponding mutual optical intensity of partially coherent quasi-monochromatic wavefields is expressed differently from the mutual optical intensity of spatially fully coherent wavefields, with only single mode in spatial frequency because of the introduction of multiple modes expansion series in the total ensemble of the total wavefields formulation.

To fully understand partially coherent electromagnetic wavefields, one normally considers that the wavefields can be explained by Gaussian-Schell model[13] with ellipsoidal Gaussian amplitude for partially coherent X-ray sources such as those coming from a 3rd generation synchrotron radiation facility. Partially coherent electromagnetic wavefields can also be expressed in terms of separate mutual intensity functions in two Cartesian coordinates, usually x and y in the plane perpendicular in the direction of propagation. Recent studies on partially coherent X-ray diffraction imaging demonstrate the reliability of the Gaussian-Schell model of three-dimensional wavefield characterization application to improve reciprocal-space modulus constraint projection in

CDI[12].

The modal expansion for generalized form of wavefield ensemble with introduction of Gaussian-Schell modal of partially coherent electromagnetic propagation can be evaluated in analogy to the mathematical formulation of quantum mechanical harmonic oscillator problem.

The eigenfunctions of the partially coherent wavefield can be expressed in Hermite polynomials with associated eigenvalues calculated representing precise modal occupancies for wavefields with particular partially coherent properties.

The propagation theory of electromagnetic radiation can be used with iterative phase retrieval algorithms, which are utilized to solve for the relative phase structures of specimens. An electromagnetic wave-field of $\psi(r)$ can be propagated into $\psi(r')$, over a propagation distance d, where k is the wave-vector and the integral is performed three-dimensionally.

$$\psi(r') = \int \psi(r) e^{-ik(r-r')^2/2d} d^3r \quad \textbf{Equation 9}$$

Electromagnetic wavefunction at specific plane by propagation of wavefields in the longitudinal direction can be calculated and measured. A detector can be used to make intensity measurement of modulus squared of wavefields at particular detector planes.

Once an electromagnetic wavefield at a particular plane is known, one can propagate the wavefield to any plane in the longitudinal propagation direction, both upstream and downstream.

1:3 Coherence and Bragg's Law of X-ray Diffraction of Finite Crystals

A finite crystal structure is composed of unit cells. Each unit cell is defined as a group of atoms in such an arrangement that follows the symmetry of lattice points in the crystal structure[16].

The electron density function of a finite crystal can be expressed in the form of convolution of a unit cell of the crystal structure with the product of an infinite lattice and a crystal shape function.

$$\text{function(Finite Crystal)} = \text{function(Unit Cell)} \otimes [\text{function(Infinite Lattice)} \times \text{function(Shape Function)}]$$

Equation 10

Where the crystal shape function can be either real or complex. The value of the shape function represents three-dimensional structural information of the spatial extent of the

crystal, thus has a uniform value of 1 within the boundaries of the object and 0 outside. Phase is related to the imaginary part of the electromagnetic wavefunction, and it is also a measure of the degree of deviation of collection of atoms from the ideal crystal lattice points within the structure.

Consequently the Fourier Transform of the finite crystal function can be derived to be product of Fourier Transform of unit cell function of the crystal structure to the convolution of Fourier Transform of infinite lattice function with the Fourier Transform of crystal shape function, which can be expressed as follows;

$$\begin{aligned}&FT\{function(\text{ Finite Crystal})\}=\\&FT\{function(\text{Unit Cell})\}\times[FT\{function(\text{Infinite Lattice})\}\otimes FT\{function(\text{Shape Function})\}]\end{aligned}$$

Equation 11

Where FT indicates Fourier Transform operation.

Bragg's law of X-ray diffraction states that incoming coherent X-ray scatters from atoms in lattice planes of the crystal specimen, indicated by Miller indices of (h,k,l)[17]. Constructive or destructive interference occurs if and only if the path length differences of the X-ray waves scattered by each plane are of integer multiples of the wavelength of the incoming X-ray. If the angle between different lattice planes and the beam is the Bragg angle θ, then

$$2d \times Sin(\theta) = n \times \lambda$$ **Equation 12**

In order to fulfill Bragg condition of X-ray scattering, the wavelength of incoming X-ray has to be comparable to that of the lattice parameters of the crystal specimen. As a result, depending on crystal structures and lattice parameters of various crystals, the energy of X-ray could be carefully chosen to obtain appropriate range of Bragg diffraction peaks.

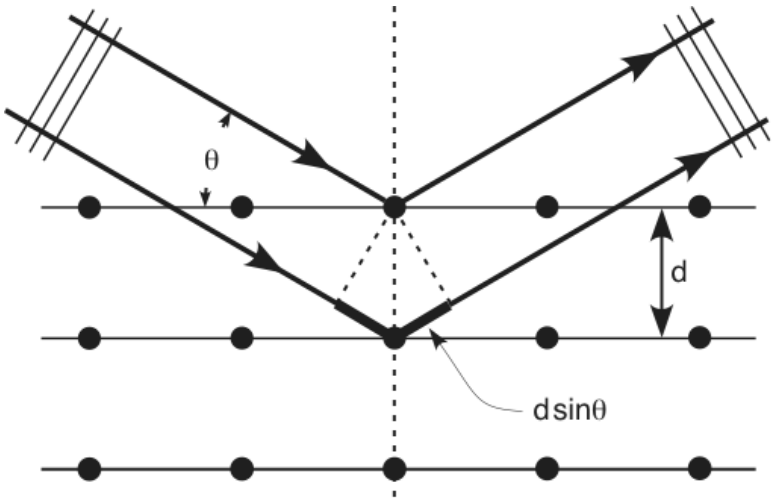

Figure 3 illustration of Bragg's law Of diffraction, Image is from Michael Hadmack, http://photonicswiki.org

When atoms in the finite crystal lattices deviate from their ideal positions or defects/impurities are present in the crystals, there will be displacements fields inside the finite crystals. The displacements can be converted into phases by calculating the scalar

product of their reciprocal-space vector Q of the specific Bragg diffraction peak with the displacements fields at each position. The magnitude of Q is calculated by 2π dividing the crystal lattice constant of specific Bragg peak. The derivation of the direct-space displacements and phase relationship has been addressed in details by Robinson et al[1]. The red lines indicated in Fig. 4 correspond to the total phase shifts of incoming X-ray relative to that of the crystal specimen, which can be calculated by $\vec{k}_f \bullet \vec{u} - \vec{k}_i \bullet \vec{u} = \vec{Q} \bullet \vec{u}$. Therefore, the phases shifts of Bragg scattering at the specific Bragg condition with reciprocal-space vector Q can be evaluated in this way, and this results in a complex direct-space object shape function. When object shape functions are complex, the corresponding diffraction patterns will be asymmetric.

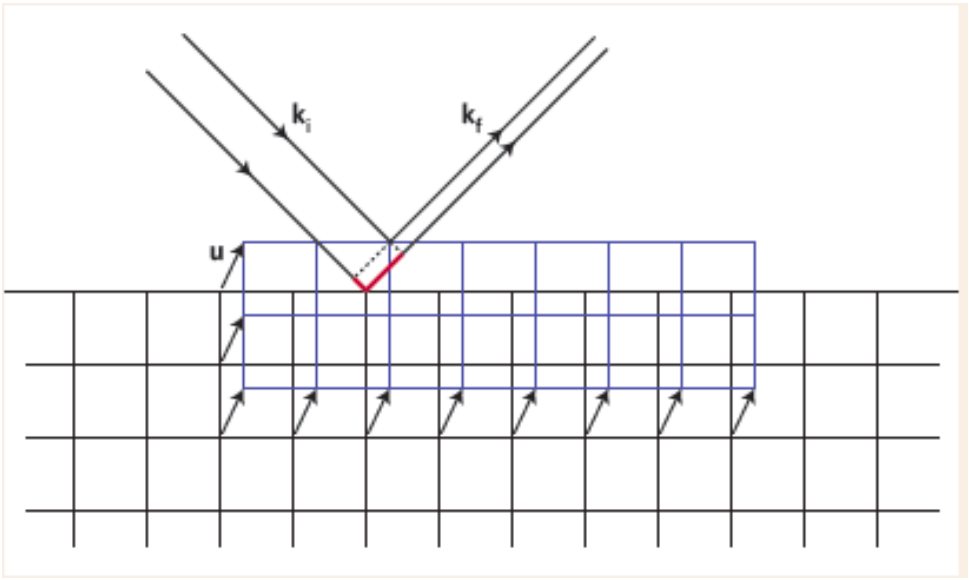

Figure 4 The red lines indicated correspond to the total phase shifts of X-rays relative to that of the crystal specimen, in Bragg reflection geometry, which can be calculated by $\vec{k}_f \bullet \vec{u} - \vec{k}_i \bullet \vec{u} = \vec{Q} \bullet \vec{u}$. Image from Ref[1]

$$\tilde{\rho}(r) = \rho(r)e^{i\Phi}$$ Equation 13

Where $\tilde{\rho}(r)$ is the complex crystal shape function and Φ is the phase.

The information obtained with X-ray diffraction can be used to evaluate the shape function of crystals, both real and complex, from experimental diffraction intensity, which is the squared modulus of the Fourier Transform of the scattered exit wave function of Bragg diffraction.

In general, the X-ray scattering process can be elastic or inelastic, or a combination of these. Elastic scattering (energies of both incident photon and scattered particle are maintained before and after the scattering), of low energy limit, which is when the kinetic energy of a incident photon is much lower than that of the scattered particle, which is also called Thomson scattering. Thomson scattering of a single electrons have a total cross-section described as follows:

$$\sigma_{\text{electron}} = 8\pi r_e^2 / 3 = 6.652 \times 10^{-29}\ \text{m}^2$$ Equation 14[18]

Where r_e is the classical radius of an electron.

The scattered electric field of electromagnetic radiation of an electron is expressed as follows:

$$E(R,t)=\frac{-r_e \exp(-ikR)}{R}\cos(2\theta)\times E_{in}$$ **Equation 15**

where R is the spatial coordinates of the observation point at the plane of polarization of incident electromagnetic wave-field; k is the wave-vector; θ is the polarization angle of the incident electric field, which is defined as the direction of propagation of the electromagnetic wavefield, and this direction is perpendicular to both the electric and magnetic fields propagation directions; and E_{in} is the time-dependent incident wave-field of the electric field.

The atomic form factor is defined to be the scattering probability of X-rays by electrons within a single isolated atom, which can be expressed as follows:

$$f^0(Q)=\int \rho(r)\exp(iQ.r)\,d^3r$$ **Equation 16**[18]

where Q is the reciprocal-space lattice vector, ρ(r) is the density distribution of electrons within an atom, and it is radial dependent because of the radial symmetry of an atom. The integral is performed over the whole three-dimensional space within an atom.

Scattering from atoms can be considered to be scattering of aggregate of electrons in atoms, which is a coherent scattering of all the electron, and the cross-section can be

generalized as follows:

$$\sigma_{\text{atom}} = 8\pi r_e^2 \int_{-1}^{1} \left| f(\theta) \right|^2 (1+\cos^2\theta)\, \mathrm{d}(\cos\theta) \quad \textbf{Equation 17}$$

Where θ is the scattering angle, and f(θ) is the complex atomic scattering factor, it is approximately independent scattering angles, and has its real part representing the effective density of scatters or scattering probability within atoms of particular kinds.

The total scattering length of an atom can be expressed as:

$$-r_0 f^0(Q) = -r_0 \int \rho(r) \exp(\mathrm{i}Q.r).\mathrm{d}r \quad \textbf{Equation 18}^{19}$$

Where is $f^0(Q)$ the atomic form factor and r_0 is the Thomson scattering length.

Detailed descriptions of diffraction by a three-dimensional lattice in crystal samples are illustrated in Ref[20], where W.L. Bragg's theorem of Bragg X-ray diffraction of lattice planes within crystals are discussed. To extend Bragg diffraction to three-dimensional structures from 1D or 2D is not straightforward, the diffraction patterns obtained mainly by X-ray diffraction of electrons within crystal samples, and several important factors for obtaining three-dimensional diffraction patterns. A two-dimensional infinite crystal is composed of a set of atomic positions, the convolution of the delta functions with the

electron density for a single atom. Infinite numbers of unit cells, within which atomic positions function repeats would lead to the definition of infinite crystals. To study a finite three-dimensional crystal sample, one needs to multiple the infinite crystal function by a three-dimensional shape function, in which all the external boundaries are appropriately defined. This leads to X-ray diffraction of finite crystal samples[20]. When samples are smaller than the coherent X-ray beam, Bragg diffraction leads to coherent fringes with fringe spacing inverse proportional to the spacing of direct-space dimensions of finite geometry in the corresponding directions. On the other hand, when the samples are bigger than the x-ray beam, speckle patterns are produced, and the sizes of the speckles are inverse proportional to the sizes of the crystals.

Scattering of finite crystals can be evaluated by Born-Oppenheimer approximation, the details of derivation and analysis was reported by C. Scheringer [21], from which we could extend scattering of finite crystals, and the expected value of scattered intensity of complex scattered exit wave function is proportional to the structural factor of crystallographic orientation of specific crystal structures.

The intensity of scattered wave-field can be expressed as modulus-squared of wave function ψ of scattered electric field, which is proportional to the structural factor $S(\vec{r})$ of a particular Bragg reflection in a particular crystal structure;

$$|\psi|^2 \propto S(\vec{r})$$ **Equation 19**

The measured intensity of the diffraction patterns I in experiments can be evaluated to be proportional to the modulus squared of complex scattered exit wave function $\tilde{A}$ as follows:

$$I \propto |\tilde{A}|^2$$ **Equation 20**

A detector placed in the downstream in experimental measurements can only detect the number of photons that hit the detector; it converts the photons count into digital signals through analog-to-digital conversion. Only magnitude of number of photons can be directly detected, while information on the directions of photons upon reaching the detector is lost and cannot be recovered directly. Details of the phase problem will be discussed in chapter 2.1.

There are a number of mathematical symmetries associated with Fourier Transform.

(1) Symmetry of shift of origin

When a function is to be translated along a particular axis, the Fourier Transform of the function will only differ from that of its un-translated one in phases, while the amplitude of its Fourier Transform result is the same. This can be derived as follows:

$$\mathrm{F}_1(q)=\int_{-\infty}^{\infty} f(x-x_0)\exp(-\mathrm{i}qx)\,\mathrm{d}x=\int_{-\infty}^{\infty} f(x')\exp[-\mathrm{i}q(x'+x_0)]\,\mathrm{d}x'=$$

$$\exp(-\mathrm{i}qx_0)\int_{-\infty}^{\infty} f(x')\exp(-\mathrm{i}qx')\,\mathrm{d}x' =\exp(-\mathrm{i}qx_0)\,F(q)$$

Which states that Fourier Transform of $f(x-x_0)$ only differs to that of original function $f(x)$ with phase factor $\exp(-iqx_0)$.

(2) Symmetry of shift of origin in q

When a function is to be translated in q, symmetry property of its Fourier Transform holds as follows:

$$\mathrm{F}_1(q)=\int_{-\infty}^{\infty} f(q-q_0)\exp(-\mathrm{i}(q)x)\,\mathrm{d}q=\int_{-\infty}^{\infty} f(q')\exp(-\mathrm{i}q'x)\exp(-\mathrm{i}q_0x)\,\mathrm{d}q'=$$

$$\exp(-\mathrm{i}q_0x)\int_{-\infty}^{\infty} f(q')\exp(-\mathrm{i}kq')\,\mathrm{d}q' =\exp(-\mathrm{i}q_0x)\,F(x)$$

The difference between $F_1(x)$ and $F(x)$ is also a phase factor, in this case $\exp(-iq_0x)$. It can be seen that the symmetry of shift of origin holds for Fourier Transform from direct-space to reciprocal-space and the opposite direction is also true.

(3) Inverse of Fourier Transform

The inversion symmetry states that the Inverse Fourier Transform of the Fourier Transform of a function is the function itself provided $\int_{-\infty}^{\infty} |f(x)|^2 dx$ is finite.

$$\mathrm{FT(function)} = \int_{-\infty}^{\infty} f(x)\exp(-\mathrm{i}Qx)\mathrm{d}x \quad \textbf{Equation 21}$$

$$f(x) = \frac{1}{2\pi}\int_{-\infty}^{\infty} \mathrm{FT(function)}\exp(\mathrm{i}Qx)\mathrm{d}q \quad \textbf{Equation 22}$$

Where FT(q) indicates the Fourier Transform operation.

Evaluation of Fourier Transform in a numerical way rather than with analytical/continuous approach is used for both real data analysis and simulation studies.

Firstly, reciprocal-space diffraction patterns have to be oversampled, which means the overall reciprocal-space sampling rate in 2D or 3D has to be equal or higher than twice than that of Nyquist frequency, and the detailed explanation can be found in chapter 2.2. Once the oversampling criterion is satisfied for either measured or simulated datasets, 2D or 3D diffraction intensities are to be represented into pixels, either in 2D or 3D arrays, which are positioned in correct coordinates. In order to successfully analyse data, additional procedures such as zero padding of arrays and cropping of data are needed.

Discrete Fourier Transform can be calculated as follows:

$$\mathrm{DFT}(q)=\sum_{n=0}^{N-1}\rho(r)_n .\exp(-i2\pi\frac{q}{N}n) \quad \textbf{Equation 23}$$

Where N is the number of pixels in dataset arrays, DFT method is used for Fourier Transform calculations of finite-size arrays.

(4) Friedel's law and beyond

Following Inversion symmetries of Fourier Transform, Friedel's law states that if a direct-space object function is real, then its amplitude of Fourier Transform is symmetric. This implies that, if a direct-space object function is complex, asymmetric Fourier Transform amplitude will be produced. In addition to these, our simulations show that the amplitude of Fourier Transform of a complex direct-space object function is asymmetric

if and only if the phases in the direct-space complex object function are asymmetric, otherwise, symmetric phases in the object function will result to symmetric amplitude of its corresponding Fourier Transform.

1:4 Experimental setups and optics for CDI

1:4:1 Experimental setups

CDI measurements for my PhD studies were all performed at beamline 34-ID-C of the Advanced Photon Source at Argonne National Laboratory, with X-ray of energy of 8.9keV (with Si (111) monochromator). The X-ray beam was cut to dimensions 30μm and 50μm using Roller-blade slits to preserve the X-ray coherence properties [22]. The coherent beam was then focussed with horizontal and vertical KB mirrors. The focus of beam was measured to be slightly less than 1.5μm in both directions using crossed Tungsten wires. Scanning X-ray beam along both directions of the transverse geometry across the Tungsten wire measures the absorption and transmission rate of X-ray beam along both directions due to the thickness of the Tungsten wire. In this way, the sizes of the X-ray beam can be estimated and quantified.

Fig. 5 shows the schematic plot of geometry of the 6 angles of Newport kappa diffractometer at 34-ID-C at APS. The sample stage and the detector part are combined with three angles each with six in total to perform experiments on Bragg geometry rocking-curve measurements. Control of the angles of the diffractometer was operated by the SPEC package at the beamline with selection of specific Bragg reflections for specific crystal structures.

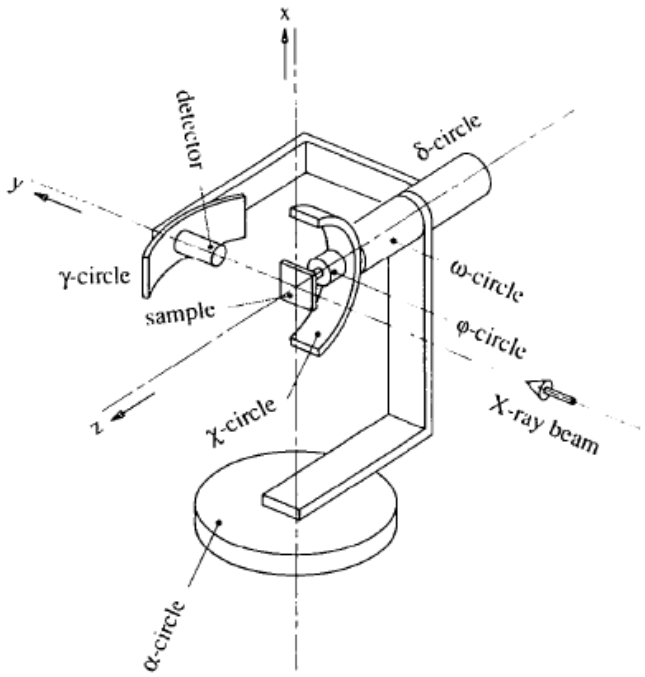

Figure 5 A typical schematic layout of a Newport Six-Axis Kappa diffractometer, image is from [23], this type of diffractometer is in use at the beamline 34-ID-C at APS

At the beamline 34-ID-C at Advanced Photon Source of Argonne National Laboratory, relatively accurate locations of nanowire structures are determined by a confocal microscope[24], and locations of specific spatial coordinates can be recorded so that those nanowires can be revisited in the future measurements. For most of our measurements, off-specular (111) reflections of Si nanowires were chosen and the SPEC control software installed at the beamline can be used to vary the incidence angle of X-ray beam, and the X-ray beam incidence angle was normally fixed to be a few degrees. A CCD detector with 20 μm pixels is used to measure far-field diffraction intensities, which is placed around 1 meter away from the sample, orientated at the corresponding (111) Bragg angle. The detector-to-sample distances can be selected depending on the specific

requirements of experimental measurements and oversampling ratios needed for particular experiments.

1:4:2 Slits in CDI

Slits are used in CDI experiments mainly to control coherence properties of incoming X-ray and also for adjustment of beam spot sizes on samples. Both horizontal and vertical slits are used in our experimental measurements for maintaining the transverse coherence of incoming X-ray beam hitting on samples. At 34-ID-C, both longitudinal and transverse coherence lengths are measured and analyzed[11], and the there is a trade-off between available total incoming coherent X-ray flux and the size of focusing spot. The bigger the slit size, the more available incoming X-ray flux, but there is a maximum slit size that over which coherence of X-ray beam is lost. The scattering divergence angle is bigger with smaller sample slits, therefore the X-ray beam spot sizes are bigger. Sample slits are used to define incident X-ray beam spot sizes, and the samples slits sizes are usually independent to the spatial resolution in CDI experiments. Bigger sample slits introduce additional modes of incident wavefields in spatial frequency, leading to illumination of partially coherent X-ray beam. This is likely to affect the coherent properties of incoming X-ray beam, which may result in reduced fringe visibility of diffraction data, therefore reducing the diffraction data quality. The optimum slit size that is chosen for measurements at 34-ID-C is 20 x 50 μm for horizontal and vertical directions respectively.

The beamline L5 slits located at the front-end hutch of section 34-ID are used to reduce the incoming X-ray beam width from several hundreds of microns to about 100 microns by insertion of reflective mirror to block the X-ray beam with 60 microns or bigger divergence radians, so that the unselected portion of beam that go directly past the focusing mirrors does not interfere with the focused beam during measureme

1:4:3 Kirkpatrick-Baez Mirror pairs

Kirkpatrick-Baez Mirror (KB mirror) pairs are used in the grazing-incidence angle geometry with specific orientation angles for both horizontal and vertical KB mirrors to achieve highly focused spots in the sample plane when X-ray beam propagating along the downstream direction. KB mirrors systems have much higher efficiency for coherent X-ray than Fresnel zone-plate based diffractive lenses. X-rays have small refractive index therefore use the grazing incidence of the horizontal and vertical mirrors to produce a focus. Fig. 6 illustrates a typical geometric layout of KB mirror pair, both horizontal and vertical focusing are performed in sequence, resulting to overall focusing in both horizontal and vertical directions of X-rays.

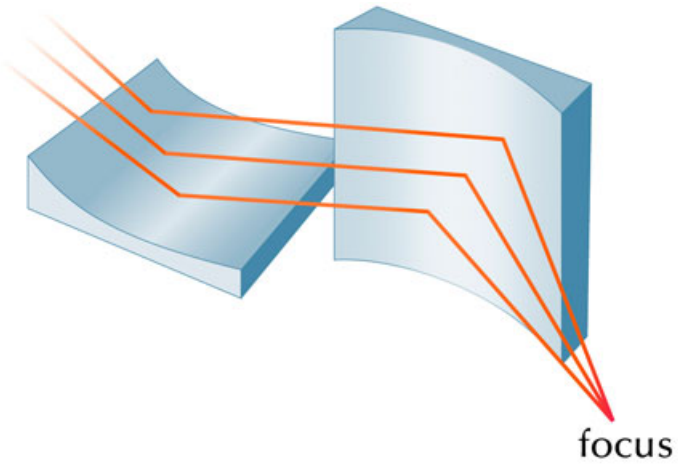

Figure 6 A typical Kirkpatrick-Baez Mirror system (horizontal and vertical mirrors pair), X-ray is focused into the focal point with high flux density. Image is from http://www.xradia.com/

1:4:4 Fresnel Zone-Plate for CDI

Fresnel zone-plates are diffractive lenses that act like circular diffraction gratings composed with alternating transparent and opaque (or phase-shifting) ring zones with density of the alternating ring zones increasing from the centre of the zone-plate. Fig. 7 shows a typical geometry of Fresnel Zone-plate, indicating the focal length and the most outer-zone-width of the zone-plate. Fresnel zone-plates are used primarily for focusing of incoming X-ray to very small beam spots, as small as a few nanometers, and the diameter of the focal spot is inversely proportional to the wavelength of X-ray; proportional to the diameter of the Fresnel zone-plate and the width of the most outer-zone of the Fresnel zone-plate. Fresnel zone-plates are used routinely in Transmission X-ray Microscope experiments, where the best achievable resolution is proportional to the optimum focal spot size.

Both Kirkpatrick-Baez Mirror pairs and Fresnel zone-plate diffractive lens produce curved-wavefronts upon incidence of plane-wave illumination, the degree of curvature of wavefronts is inverse proportional to the distance away from the focusing optics. At the actual focusing point, the wavefields become plane-wave with the strong curvature information encoded within the surrounding fringes at the focus point so that the overall wavefields features prevail.

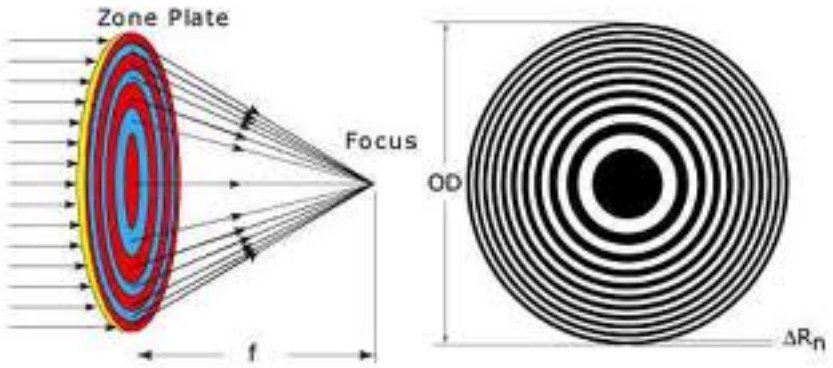

Figure 7 Typical Fresnel zone-plate diffractive lenses geometric layout. Image is from: http://www.esco.co.kr. left: f is the focal length of zone-plate, right: OD is the diameter of zone-plate and ΔRn is the most outer-zone-width of Fresnel zone-plate

Christian Schroer et al performed simulation studies[25] on focusing of X-ray by Fresnel zone-plate.

The two types of focusing optics are fundamentally different in both overall efficiency and aberrations effect.

The overall efficiency of a typical Fresnel zone-plate is rather low comparing to that of Kirkpatrick-Baez Mirror pairs, however, due to extremely small focal spot produced by Fresnel zone-plate, the X-ray flux density at the focal spot is relatively higher with Fresnel zone-plate, though with some sophisticatedly designed Kirkpatrick-Baez Mirror pairs the focal spot can be as tiny as a few nanometers[26].

Because Kirkpatrick-Baez Mirror pairs are reflective focusing optics, aberrations of the mirrors are much less than that of Fresnel zone-plates, which are transmission-geometry diffractive focusing lenses.

1:4:5 X-ray Detectors

A Princeton CCD detector has been used at 34-ID-C for quite a few years. A Medipix detector developed by international collaboration hosted by The European Organization for Nuclear Research (CERN) was recently installed in the hutch with higher dynamical range and lower instrumental noise than a conventional CCD detector. Various ranges of detectors are used in CDI measurements, while CCD and Pilatus detectors (developed by the Swiss Light Source) are the most popular ones among them. The pixel size in our CCD detector is around 20 μm, with Pilatus the pixel size is relatively larger, around 172 μm.

Several factors need to be taken into account when comes selection of detectors in CDI experiments. These include desired dynamical range, the energy range of X-ray, the

efficiency of detection at specific X-ray energy, the readout time, the maximum count rate and the pixel size etc. Details of properties of X-ray detectors are illustrated in the X-ray data booklet from Berkeley[18].

2 Theories of CDI

2:1 The Phase problem

2.1:1 Definition with its Quantum mechanical origin in general

The “Phase problem” has been a widely studied subject since middle of the last century; it is a general physics problem that is essential in most of applications of fundamental aspects of physics in various fields, ranging from applied mathematics to astronomy. Directly solving the phase problem without aid of known experimental constraints has been predicted to be impossible, due to its quantum mechanical nature. When one considers X-ray propagation in terms of electromagnetic wave with well-defined wave functions and eigen-vectors quantum mechanically, all the measureable quantities are to be described with probabilistic nature, therefore all the measured eigen-values are interpreted with probability with no absolute certainty of one single unit of object such as position of a single photon. Diffraction intensities with a collection of photons detected are only physically meaningful when described with expectation values. Since everything we measure in experiments is expressed into expectation value, the most-likely value in the probability distribution, the position of photon only makes sense when there are sufficient amount of photons to be detected and converted digitally efficiently. This results in an expectation value of number of detected photons at specific position measured with some degree of reliability at a detector downstream. New detector

capabilities have allowed single photons to be measured. The position of a single photon can be absolute determined on the detector because wave function of the single photon is collapsed when detection takes place.

The phase problem in crystallography is slightly different from the one that discussed here. In crystallography, diffraction patterns are recorded with intensities, where the phase information is lost. To fully determine three-dimensional electron density map, one has to approximate phase values, combining with the known amplitude of specific crystallographic orientations and volume of the whole structures, which can be determined by the spacing of the crystallographic reflections. In crystallography, the phase problem can be solved by the direct method[27] if the number of atoms in the molecular structures is less than 1000. When the number of atoms in the system is bigger than about 1000, the direct approximation becomes difficult.

Several attempts have been made for successfully for extracting phases from diffraction intensities, such as holography[28,29], both in electron[30], X-ray, and optical regime. This ability has revolutionized the imaging science, though several difficulties are present for utilizing holographic-based technique. Coherent X-ray diffraction imaging, which is a lensless imaging technique, has also opened up a new way of extracting phases by using various iterative algorithms, which can be done just with computers alone. Nevertheless, developments of various iterative algorithms have been ongoing for almost half century

since the first Gerchberg–Saxton Error-Reduction (ER) algorithm[31], which was introduced in both Electron Microscopy based imaging method, as well as X-ray imaging.

It is been widely discussed that the phase problem in Electron and X-ray sciences may not be directly-solvable because of its quantum mechanical nature, due to the fact that the direct-space and reciprocal-space space sets are of Fourier Transform relationship, which can be categorized to be complementarity pair, which have the relationship of being a conjugate pair of observables in quantum mechanics. Therefore, solutions to be satisfied to exact constraints in both direct and reciprocal-space are probably not attainable, although it is argued that the phase problem situation in Electron and X-ray sciences are not in the quantum mechanical scale. Consequently, Heisenberg uncertainty principle may not apply here.

2:1:2 Phase problem in general condensed matter physics

As discussed in section 2:1:1, the quantum mechanical version of the phase problem, in general condensed matter physics, phase is just one of the two essential parts of encoded information for extracting the electromagnetic wave-functions. Such functions are connected with the determination of information about systems under investigation, such as topology, internal and surface morphology, as well as spatial structures. Pierre Thibault has discussed the definition of the phase problem in condensed matter physics in his PhD thesis[32], where he describes that phase information has to be extracted in order to get a complete picture of the system under investigation. An external observer can never make quantitative observation of both photon position and phase of exit electromagnetic wave simultaneously due to its quantum mechanical nature, estimation of phases is just an extra procedure for understanding of experimental measured data for solving structures of objects of scientific interest in general.

2:2 Oversampling in CDI

It has been proven in mathematical articles that if recorded diffraction data satisfy oversampling conditions[1,33] they contain enough information to solve the phase problem, except for certain elementary symmetries of the solution. “Oversampling” is defined by the Nyquist-Shannon theorem[34]. Nyquist sampling frequency is defined to be twice the maximum frequency of the reciprocal-space information. Furthermore, this frequency is the sampling frequency of the reciprocal-space lattice point in a crystal. The Nyquist sampling criterion states that in order to retrieve a signal correctly from a set of sample points, the sampling frequency has to be higher than the Nyquist sampling frequency. Sayre went on to propose this criterion as a necessary condition for successful reconstructions of both electronic density and phase from measured reciprocal-space diffraction patterns of structures, one has to be able to acquire at least double amount of the sampling points of the reciprocal-space lattice frequency of measured structures[35], this proposal originates from the fact that both amplitude and phase information needs to be extracted, thus double the amount of unknowns have to be resolved compared with the number of reciprocal-space sampling points of the samples. It can be generally considered that to enable unique reconstructed solutions, good quality experimental measurements have to be obtained, which means the signal-to-noise-ratio (SNR) needs to be sufficiently high to gain useful data for reconstructions.

2:3 Uniqueness in CDI

The one-dimensional uniqueness problem in general has been carefully studied[36], and results suggest that for these systems an infinite number of solutions are to be found because there are infinite of answers that have the same auto-correlation function. For two-dimensional structures, studies suggest that non-unique solutions can only be found in deliberately-constructed symmetric systems with two-fold ambiguity[3738]. Miao[39] and Bates[4041] have investigated the uniqueness problem and their results are discussed in this section.

The "oversampling ratio", which is the ratio between the number of available data points in reciprocal-space and the direct-space sampling points, has a minimum value of $\sqrt[3]{2}$ or $\sqrt{2}$ for three or two-dimensional measurements respectively according to Sayre's original theory. Overall, the datasets have to have oversampling ratios of at least 2, which in theory is sufficient for experimental data with satisfactory quality to be uniquely reconstructed. The minimum required is cube root/square root of two which is less than 2 suggested by Sayre this comes from the fact that 2 and 3 dimensional problems are over-determined. The argument from Miao and Bates is that the Sayre criterion is too strong. Miao et al[39] has performed detailed calculations to demonstrate that for two or three-dimensional datasets, unique solutions can be found if the oversampling ratio in each direction reaches 2 or more.

For experimental datasets, the measured variables have to be equal to higher than the degrees of freedom in order for the solutions to be uniquely resolved. This is generally true for mathematical problems, where it is better to be over-defined rather under-defined to have reliable solutions that are uniquely defined.

The uniqueness of solutions during wave propagation approach has also been studied by John Spence et al[42] and Pierre Thibault et al[43], the former investigated the necessary conditions for uniqueness solutions to be obtained in the CDI method in general, and the latter worked on propagation uniqueness directly and analytic expressions for calculation of expected degradation as function of tightness of supports in the presence of experimental noise.

2:4 Propagation Uniqueness in far-field-geometry CDI

The uniqueness problem in Coherent Diffractive Imaging (CDI) has also been addressed by Rodenburg[44] and Huang[45], Huang has further confirmed the existence of non-unique solutions of far-field CDI data reconstructions with simulations[45]. Propagation of electromagnetic wave in far-field geometry is illustrated in the following mathematical formulation of wave propagation[45];

$$t'(r') = \int t(r) \mathrm{e}^{-\mathrm{i}k(r-r')^2/2d} \mathrm{d}r \quad \textbf{Equation 24}$$

Where d is the propagation distance of electromagnetic waves exiting from measured samples, i.e. the distances between different diffraction planes in the far field geometry. Both $t(r)$ and $t'(r')$ are complex wave-functions representing samples at positions d apart from each other, connected by propagation. The complex electromagnetic propagation exit wave from a sample can be propagated to an infinite number of planes, however in this case, measurements are only considered at two planes separated by distance d. As can be seen by propagating them to the far field, $t(r)$ and $t'(r')$ are both solutions for direct-space reconstructions because they have identical diffraction patterns in the Fourier domain. Which solutions obtained by a reconstruction algorithm depends on whichever constraints are applied in direct-space part of the algorithms, and different results are generated with different constraints, therefore, one has to have some a priori

knowledge of the samples in order to select specific constraints in iterative reconstructions.

Both Huang[45] and Newton[46] have proposed modified algorithms for better reconstructions of highly strained Bragg-geometry CDI measured data with improved three-dimensional electronic density. The problem arises from the fact that with highly strained objects, where a specific feature has significant strain in the sample that causes phase shifts exceeding 2π (which is called a "phase-wrap") between different parts of sample, might lead to reconstructions with amplitude having gaps in the phase-"wrap" regions. Newly invented constraints improve the quality of inversions resulting in most of gaps in "phase-wrap" positions being filled in according to simulation studies in chapter 3.

Possible solutions to the above non-uniqueness problem are proposed, the ones that have been most successful are curved wave-front illumination which was demonstrated to have better convergence successes[8] in reconstructions. These curved wave front are, for example, wave front illumination from zone-plates. The key to solving the twin ambiguity problem is to break the symmetry of between entrance and exit wave functions. This will more likely to achieve a unique solution in CDI in general.

2:5 Optical Path-Length-Difference (OPLD) problem in CDI

To fully utilize the properties of Coherent X-rays at Coherent beamlines in 3rd generation synchrotron facilities, one has to make sure that the longitudinal coherence lengths has to be larger than the optical path-length-difference of all paths through the samples under investigations. Leake and colleagues have demonstrated[11] not long ago that varying optical path-length-difference of coherent X-ray illumination, which involves both reflection and transmission in Bragg geometry, can influence the measurement of visibilities of reciprocal-space diffraction fringes. These experiments were performed by measuring different Bragg peaks of crystalline structures and also by recording varying coherent properties of incoming X-ray probe. Bean and colleagues have done detailed experimental work[47] on studying the relationship between fringe visibilities of reciprocal-space diffraction patterns and the overall optical-path-length-difference (OPLD) of the X-ray illumination. Nevertheless, the measurements do not quite agree with theoretical hypothesis in which the fringe visibilities decrease with increasing OPLD. The underlying basis for this hypothesis is rather subtle. Therefore, this hypothesis remains to be proven with possibly better experimental setups and instrumentations and data detections etc., which are needed to be developed further.

2:6 Partial coherence corrections in the reciprocal-space modulus constraint in CDI

A number of constraints can be applied in reciprocal-space diffraction data. Generally speaking, one can introduce modifications into the conventional reciprocal-space modulus constraint, for example, when considering the corrections of area detector's imperfect pixels by applying a data mask in Fourier space for data analysis and incorporation of various types of noise during experimental measurements[48] etc.

One can also introduce reciprocal-space partial coherence correction to modify the conventional modulus constraint, based on the actual experimental conditions when the illuminating X-ray beam has some degree of partial coherence. Application of this partial coherence results in much better data reconstructions.

Clark et al have demonstrated partial coherence correction can be used to successfully recover images in partially-coherent CDI[12] and Huang et al have demonstrated the importance of partial coherence effect in Ptychography[49] experimental measurements. This correction worked very well with gold nanocrystals and extended ZnO crystals.

Accumulated partial coherent intensities, which are the measured diffraction intensities during experiments, are the convolution of the average of mutual coherence intensities at the detector to the coherent intensities with fully coherent X-ray illumination. This partially coherent modification step is introduced into the reciprocal-space modulus constraint part of the iterative algorithm for phase retrieval, so that the contribution of

partial coherent X-ray illumination can be taken into account during data reconstructions, leading to much improved data inversion quality. Fig. 8 shows a typical example of improvement of data reconstruction when appropriate partial coherence corrections are integrated in iterative algorithms.

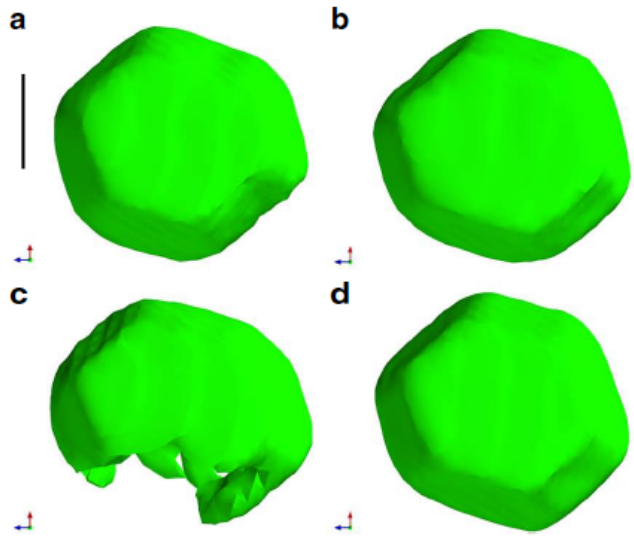

Figure 8 (a–d) Opaque isosurfaces (50% of the maximum) of the reconstructed nanocrystal for differing coherence conditions. (a) Imaged under high-coherence conditions assuming full coherence and (b) using the partially coherent modulus constraint. Images from the low-coherence conditions assuming full coherence (c) and using the partially coherent modulus constraint (d). Image comes from[12]

3 Algorithms of Coherent Diffraction Imaging (CDI) in Bragg Geometry

Diffraction intensities are given by the Fourier Transform of the corresponding direct-space complex density, either in 2D or 3D. Phase information is lost when a detector records diffraction intensities. Oversampling conditions have to be satisfied in all dimensions in reciprocal-space diffraction patterns, with at least 2 pixels between diffraction fringes, in all spatial dimensions, for 2D or 3D diffraction patterns in Fourier space to be successfully reconstructed. Detailed discussions on the phase problem in condensed matter physics and X-ray sciences, as well as oversampling criteria theorem are presented in Chapter 2.

To solve the phase problem by CDI, iterative algorithms are usually used to iterate answers between direct space and reciprocal space, imposing various constraints in both spaces, by repeatedly performing forward and inverse Fourier Transforms. Historically, the first iterative algorithm, Error Reduction (ER) was proposed by R. W. Gerchberg and W. O. Saxton[31], initially successfully utilized in Electron Microscopy to obtain the missing phase information in both direct and reciprocal space. Similar principles apply to X-ray phase retrieval problem; the ER algorithm remains one of the most important building blocks of iterative algorithms in CDI and Ptychography. Bragg-geometry Ptychography will be discussed in details in Chapter 8.

CDI algorithms are presented in projection language[50], which was first introduced by Veit Elser are widely recognized as the most illustrative and understandable way to illustrate their operation. ER algorithm can be illustrated by using projection language as follows;

$$\rho_{n+1} = (\pi_s \pi_m) \rho_n \quad \text{Equation 25}$$

Where π_s and π_m represent direct-space support constraint and reciprocal-space modulus constraint projections respectively. ρ_{n+1} and ρ_n represent the next and current iterates of the sought object (in direct-space) respectively. To start the algorithm, a guessed solution in direct-space is assumed, Fourier Transformed, followed by the reciprocal-space modulus constraint projection; then returned to direct space by performing a Inverse Fourier Transform followed by support constraint in direct-space. This procedure is repeated for a sufficient number of iterations until data convergence has been reached.

There is a serious "twin" solution problem in CDI because the complex conjugate of the position-reversed exit wave function of solution has the same far-field diffraction intensity. Usage of iterative algorithms is unable to differentiate the twin images. The twin solution problem applies most seriously in real direct-space asymmetric objects.

However, if the direct-space asymmetric object is complex with symmetric phase structure, the diffraction intensity of the complex object would be the same as that of the twin object. The twin solution problem can be avoided if direct-space complex objects have asymmetric phase structure if an asymmetric support constraint can be provided.

The Hybrid-Input-Output (HIO) algorithm was later introduced by J. R. Fienup[51,52], in the 1980s, aiming for improvements of problems of stagnation of solutions in local minimums in conventional ER based algorithm. The HIO algorithm can be defined as follows, using the projection language;

$$\rho_{n+1}(u)=\begin{cases}\pi_m \rho_n(u) & \text{if } u \in \text{Criteria} \\ (1-\beta\pi_m)\rho_n(u) & \text{if } u \notin \text{Criteria}\end{cases} \quad \text{Equation 26}$$

Where β is a feedback parameter, it is normally selected to be between 0.5 to 0.9, though it can be selected to be bigger than 1 occasionally[53]. “Criteria” can be conditions that need to be satisfied as direct-space constraints, such as the standard support constraint, positivity density constraint, etc. Support constraint is performed in direct-space, where the density within the support region is kept, and the density that is outside the support region is set to zero.

Another HIO based algorithm developed by Ross Harder is Phase-Constraint HIO (PCHIO)[54], in which direct-space phases are constrained to be within a range with minimum and maximum phase values, usually -0.5π and +0.5 π, and this acts as extra direct-space constraint criterion that shows significantly improved data convergence.

$$\rho_{n+1}(u)=\begin{cases}\pi_m \rho_n(u) & \text{if } u \in \text{support} \cap \phi > \phi_{min} \cap \phi < \phi_{max} \\ (1-\beta\pi_m)\rho_n(u) & \text{if } u \notin \text{support} \cap \phi < \phi_{min} \cap \phi > \phi_{max}\end{cases} \quad \text{Equation 27}$$

The real space phase constraint can be thought of as a generalization of the standard support constraint. The conceptual idea of a phase "support" has been developed into a new algorithm in the work presented in this thesis.

The HIO based algorithm is quite successful for improvement of data convergence comparing with that of using ER alone, however, convergence can only be guaranteed if and only if both direct and reciprocal-spaces can be presented as convex spaces.

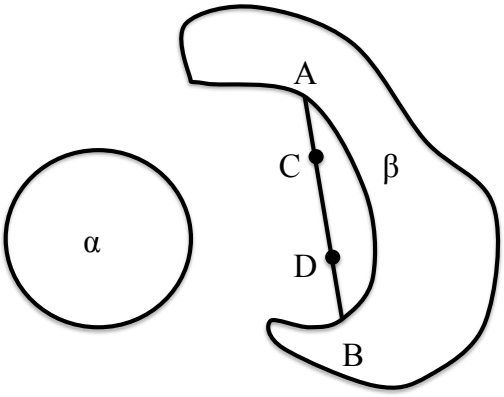

Figure 9 Graphic presentation of convex and non-convex space sets, α is represented as convex space, and β is a non-convex one because points C and D are outside the space β, and they both lie on the shortest distance between point A and point B

Convex space sets are defined as the curvature of the space sets is defined in the way that all the points on the shortest distance between any two points in the space sets are contained within the space sets; while the space sets are defined to be non-convex when there is any point on the shortest distance route that connecting two points within the space sets lying outside the space sets geometry. Fig. 9 shows an example for a convex and a non-convex space sets.

The ER algorithm is less effect when dealing with stagnation of solutions at local minima, which can lie anywhere between or around the straight line linking AB in Fig. 9. Introduction of HIO cannot guarantee solutions to converge, but it provides better chances of leading solutions to global minimum instead of being stuck at local minima.

3:1 Introduction to some well-developed algorithms in Coherent X-ray diffraction imaging (CDI)

Many algorithms are associated with reconstructions of CDI measured data, The three most important are ER, HIO and PCHIO, defined above. Other useful algorithms, which are also widely used, are the difference map[50], which is a generalized form for Hybrid-Input-Output algorithm and shrink-wrap[17], which is extremely useful for compact nano-crystals, such as Gold nano-crystals[12]. Recent developments on highly strained compact objects have demonstrated significant improvements[9,45,46], and combinations of several different algorithms have also been demonstrated to show better results in some cases[45]. However, none of the existing algorithms or combinations of these can in principle guarantee convergence of results of iterative reconstructions. Conventional iterative algorithms often fail when phasing the diffraction patterns of highly strained objects. Usually, the algorithms lead to local minima, and solutions become stuck at these minima, failing to reach data convergence.

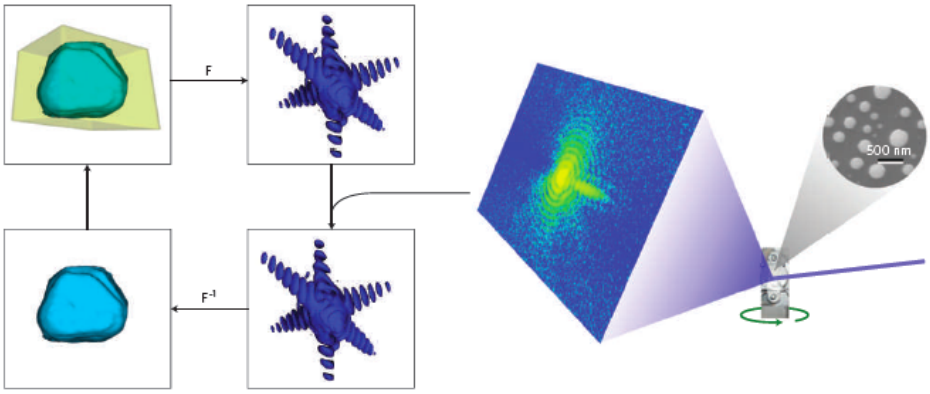

Figure 10 The schematic diagram shows outline of the fundamental underlying algorithm that permits the reconstruction of a sample distribution from its diffraction pattern in Bragg geometry[1].

Fig. 10 illustrates the fundamental principle of CDI iterative algorithms. It works as an iterative procedure using forward and inverse Fourier transforms to connect between direct and reciprocal-spaces, with application of both direct-space support constraint and reciprocal-space modulus constraint. Diffraction data are taken from experiments and used for reciprocal-space constraints, assuming the noise and other imperfections of contributing to measurements are small. Initial guesses can be implemented either in direct space or reciprocal space, whichever suits best. In our case, initial random guesses in direct-space are implemented, comprising an initial guess of the physical support shape in direct space with amplitude of random numbers inside the support, while the amplitude is set to 0 everywhere outside the support. An FFT is performed so that modulus constraint (keeping the phases values while replacing the amplitudes with square root of measured intensity of diffraction data) can be applied in reciprocal space after the first iteration of the algorithms. The algorithm then performs an Inverse Fourier Transform to go back to direct-space to impose support constraint, keeping the amplitude inside the

support the same but points which are outside the support zero (in ER). A χ-square error metrics can be calculated between the amplitudes of the data and the iterate in reciprocal space. Alteration of ER with HIO algorithm shows better convergence and avoids stagnation of reconstructions, because the advantage of Hybrid-Input-Output (HIO algorithm over ER is that an extra feedback parameter β is introduced so that the algorithm is more likely to lift stagnation on the local minimum values of χ-square, in order to reach better solutions closer to the global minimum value of χ-square. Detailed analyses on error metrics of convergence success rates of different algorithms are illustrated in Garth Jonathan William's PhD thesis[10].

3:2 Details illustration of general approaches of all existing CDI algorithms

Detailed descriptions of both difference-map[50] and HIO[51,52] have been illustrated in literature. No algorithms guarantee data convergence because in order to find converged solutions, i.e. global minimum of solutions that satisfying both direct and reciprocal-spaces, one has to consider whether both direct and reciprocal spaces satisfy the criterions of being of convex space sets, details of which has been explained in the introduction of this Chapter[42].

3:3 Constraints in directspace and reciprocalspace

The constraints form the essence of the algorithm since the remainder is just the Fourier Transform. Usually the reciprocal-space constraint is just the "modulus constraint" which keeps the iterated phases but overwrites their amplitude with the measured value.

3:3:1 Constraints in direct-space

Most of currently applied constraints in CDI algorithms are associated with direct-space; the reliable constraints mostly come from *a priori* knowledge of specimens, for example,

the specific amplitude or phase distribution of designed complex objects. The support constraint can be vital if low-resolution information of an object's 3D density can be accurately estimated, and this can be done with TEM and related techniques. The Shrink-wrap algorithm[17] utilizes 3D density of previous iteration of iterative procedure, with appropriate Gaussian smoothing process, to produce updated support for the next iteration of reconstructions. The method is very effective when objects are of weak-phase category, because the supports produced during Shrink-wrap reconstructions are real only. If the object has complex electronic density in direct-space, for example if atoms have some deviation from the ideal lattice positions of a perfect crystal solutions tend to be difficult to seek compared with that of the real density object. Other direct-space constraints include positivity constraint, histogram constraint etc. Furthermore, Guided-Hybrid-Input-Output (GHIO)[55] method is very effective. The GHIO algorithm start with several initial random guesses of both amplitude and phase to start iterative procedure, once first round is finished, the algorithm selects some best results according to specific criteria, such as reciprocal-space error metrics or direct-space surface smoothness etc. to guide the next round of iterations, both for amplitude and phase. After several rounds/generations of GHIO, solutions will normally converge and relatively stable regardless of initial random starts.

An important development was the Fresnel CDI (FCDI) method. FCDI introduces the well-calibrated illumination of X-ray probe as an additional constraint[8,56,57]. By breaking the symmetry between the object, due to the phase curvature of this probe, the

convergence of ER and HIO methods is greatly improved. The FCDI experiment commonly utilizes a Fresnel Zone-plate (FZP), slightly out of focus, to generate a well-defined curved X-ray illumination with a roughly spherical wavefronts. Extra constraints can be applied in this technique, however the constraint is applied as the X-ray probe illumination at the propagation planes where solutions are to be sought. In FCDI the overall complex exit surface wave (ESW), which is measured to be modulus squared, i.e. measured diffraction patterns can be approximated to be modulus squared of the product of complex object function and the complex illumination function of incoming electromagnetic wave function at specified propagation planes. Abbey et al has reported that measurement efficiency has been vastly improved[58] by using polychromatic coherent X-ray diffraction imaging; the multi-modal structure of polychromatic X-ray beam was calculated and introduced into the iterative algorithms for data inversion. However, so far FCDI has studied only real objects where the factorization into a phase from the beam and amplitude from the sample is easiest. In the so-called "keyhole" method[8], three-plane propagation of X-ray wavefields is introduced, the three planes are the sample plane; the pinhole plane (where selection of X-ray harmonics order is performed) and the detector plane. No studies of FCDI technique on complex direct-space object have been made up to now. Studies of highly strained objects with structured illumination CDI can be a effective way to solve ambiguity to ensure unique reconstructions of data, but introduction of curved wavefields could cause extra degrees of ambiguity if they are not well characterised.

Imaging methods based on structured illumination have been widely applied in FCDI and are reputed to work especially well when Fresnel numbers are set to be bigger than 5, originally proposed mathematically by H. M. Quiney et al[15,59], when the X-ray illumination curvature in FCDI geometry is sufficiently large for successful data inversion. Fresnel number is defined as a dimensionless number in diffraction optics[60], and it is proportional to the radius of aperture, in most X-ray cases, radius of a pinhole; and it is inversely proportional to both the detector-to-sample distance, D, and the wavelength of the X-rays.

$$\text{Fresnel Number } F = \frac{\text{pinhole radius } R^2}{D\lambda} \quad \text{Equation 28}$$

Nonetheless, conventional structured illumination methods are only applicable for small phase-curvature direct-space objects. In the experiences published so far, there appears to be no advantage of FCDI over CDI for the case of strong-phase objects. It is possible that FCDI could be worse than CDI if the beam curvature is confused with any (unknown) phase structure in the sample.

Huang et al[45] have proposed the use of a tight support constraint in direct-space to relax the need to constrain the object phase. This generally leads to apparently unique solutions, which is similar to Harder's method of PCHIO. However, while PCHIO works relatively well for weak phase objects, the algorithm normally fails to find sensible solutions for large-phase objects, by failing to fill in the density wherever the phases go out of range.

The highly strained regimes have been heavily explored lately. Several methods[9,45,46,61] have been shown to improve the reconstruction convergence for strong-phase objects. Some assume no a priori information on the object, while others incorporate assumed knowledge of direct-space structures, both in amplitude and phase, whichever can be estimated and utilized to guide reconstructions.

3:3:2 Practical Aspects of Direct-space constraints

For highly strained diffraction patterns, several difficulties may arise due to the complicated nature of their reciprocal-space intensity patterns. In order to have successful inversion, one needs to center the reciprocal-space intensity correctly so that it does not introduce additional phase-ramps in direct-space after Inverse Fourier Transform. The center of highly strained diffraction intensity could be the brightest pixel or the center of mass of the intensity patterns or somewhere in between. In practice, one needs to guess and try to align diffraction intensity until no additional phase-ramps are present in direct-space object following the data inversion process. Our analysis shows that for ER, when the iterative algorithm starts with an initial guess that is very close to the actual complex object in direct space, the algorithms are much more likely to find a converged solution, which is in a close resemblance to that of the correct solution. If starting models have large deviations from the correct solution, the inversion may partially converge, leading to partially correct solutions, however, the solutions are better comparing to that of

random initial starts. For HIO, it is generally found that initial starts of algorithm do not usually affect the final inversion results.

3:3:3 Constraints in reciprocal space

Experimental noises present in reciprocal-space diffraction data can be corrected and taken into consideration with modified reciprocal-space modulus constraint which can lead to improved data reconstructions[48]. Corrections of noise and other imperfections during experimental measurements can be performed with the Maximum Likelihood Estimation (MLE) technique[62].

Maximum likelihood Estimation is a technique used widely in estimations of unknown variables from independent and identically distributed observations following a distribution with an unknown probability density function. The observed known variables and unknown parameters belong to a certain family of distributions, which represented in the form of vectors. Both the likelihood function and logarithm of likelihood function (log-likelihood) are defined as functions of the known and unknown variables, and the likelihood function is to be maximized to obtain the expected/average values of unknown variables in they study. To find these unknown estimated variables, one needs to obtain variables with the highest probability of the specific distribution function, which is a joint mathematical formulation of both known observed variables and unknown variables. The

Maximum Likelihood Estimation technique is not guaranteed to find solutions to a specific problem, because of its assumption on experimental data being independently and identically distributed. Other reasons why it may fail to work is probably due to the complex nature of the experimental dataset, in which a number of solutions are possible with equal probability of several distribution functions.

For datasets from highly strained crystals, the indication of whether reconstructions have reached true convergence may be different from that of conventional weak phase cases. Simple Chi-square values may not be sufficient indication, and it is our impression that Chi-square from the data alone can be misleading indication of data inversion success because some of the more successful inversions (based on their appearance) can have Chi-square values bigger than many of the much less successful reconstructions. Chi-square error metric and correlation coefficient error metric in general X-ray crystallography are defined in the following ways;

$$\frac{\sum_{i=1}^{N}\left(A_i^m - A_i^c\right)^2}{\sum_{i=1}^{N}\left(A_i^m\right)^2} \quad \text{Equation 29}$$

$$\text{Coefficient}\left(A^{m}\right)=\frac{\sum_{i=1}^{N}\left(A_i^{c}-\left\langle A_i^{c}\right\rangle\right)\left(A_i^{m}-\left\langle A_i^{m}\right\rangle\right)}{\left[\sum_{i=1}^{N}\left(A_i^{c}-\left\langle A_i^{c}\right\rangle\right)^{2}\right]^{1/2}\left[\sum_{i=1}^{N}\left(A_i^{m}-\left\langle A_i^{m}\right\rangle\right)^{2}\right]^{1/2}} \quad \text{Equation 30}$$

Where A^m and A^c are measured and calculated amplitudes respectively. Calculated and measured amplitudes can also be used here to define correlation coefficient for amplitudes. $\left\langle A_i^{c}\right\rangle$ and $\left\langle A_i^{m}\right\rangle$ are the expected/average value of calculated/current iteration in reconstruction procedure and measured amplitudes. The summation is all over the all the amplitudes/intensities in the available resolution range in the experiments. In general, the error metrics are used for justification on agreement of experimental data with the final reconstructed solutions. It is rather difficult to say which error metric is better in terms of agreement of agreement of real data, though the selection of specific error metric is dependent to the nature of particular experimental measurement.

3:4 Spatial Resolution of Coherent X-ray diffraction imaging: relationship between spatial resolution and available photon flux density

CDI has advantages over most of its competitive techniques such as TEM mainly for two reasons. First, as a lensless imaging technique, CDI has removed all difficulties and problems associated with lens aberration and imperfections, all of which may result in image quality reduction and extra inaccuracy of high-resolution image reconstructions.

Consequently, removal of lenses in imaging systems make spatial solution only diffraction limited[63], i.e. the resolution is only related to the wavelength of the X-ray beam, and the maximum angle to which a diffraction signal is generated (see below). Theoretically, it should be possible to reach atomic spatial resolution with ultra-intense X-ray source, such as X-ray free electron laser.

Secondly, CDI is a reciprocal-space imaging technique, comparing to most of its counterpart direct-space imaging methods. The maximum attainable resolution is dependent on the maximum attainable high-angle scattering signal-to-noise ratio in reciprocal-space intensity patterns. Nevertheless, the currently available coherent flux of 3rd generation synchrotron facilities still limits the ability to obtain high-quality high-angle scattering signals. The necessary incident flux of X-ray is inversely proportional to the fourth power of the best achievable spatial resolution attainable according to recent studies[64]. To reach the desired spatial resolution, it may be difficult even with upgraded or newly built 3rd generation synchrotron radiation sources worldwide. One of the possible alternatives is to increase further the flux density of the incident X-ray on specimens. However, there is a trade-off between best-achievable spatial resolution and measurement time (also field of view of specimens under investigation). To be able to study larger specimen with large field of view, longer measurement time is needed for scanning because the focusing spots are much smaller, reaching a few nanometer in sizes with highly focused KB mirror system[26]. This may require experimental measurements to be performed with higher degree of quality in much more stable instrumentations and

environmental conditions, in order that X-ray beam drift; temperature variation; environmental humidity fluctuation and sample fluctuation etc. should be kept to a minimum. The detailed discussion on radiation damage on specimens can be found in Chapter 4.

3:5 2D Simulation studies for Test of Robustness of Conventional ER and HIO algorithms

Simulation studies on highly strained 2D objects by using conventional ER and HIO algorithms were performed. Our results show that reconstructions of highly strained object with linear phase ramps work relatively well, even with the sizes of supports being 20 or 30 % bigger than the actual direct-space objects. However, with objects with high degree of phase curvature in direct-space, the reconstructions using conventional ER and HIO usually fail, even when the supports are exactly the same sizes of the actual simulated objects. Random fluctuations occur for both reconstructed amplitudes and phases.

Fig. 11 to 14 show some 2D simulation studies on highly-strained CDI reconstructions, with only initial random amplitude and phase, with ER and HIO algorithms with no phase constraints applied. It is not yet a well-understood problem on the reason why highly strained objects with high phase curvatures are difficult to reconstruct even with

very tight supports in direct-space constraint. However, tight support constraint work relatively well with highly strained objects with linear phase structures.

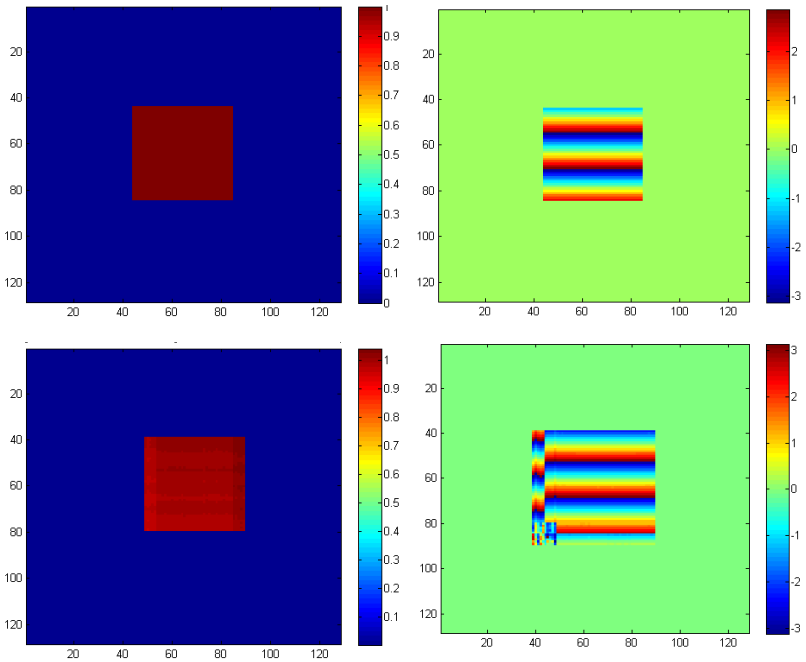

Figure 11 Top Panel: Simulated amplitude and phase; where the support is 2D box with 4 pixels bigger than the original object on each sides of the box. Bottom Panel: Reconstructed amplitude and phase by using ER (500 iterations) + HIO (500 iterations) + ER (500 iterations)

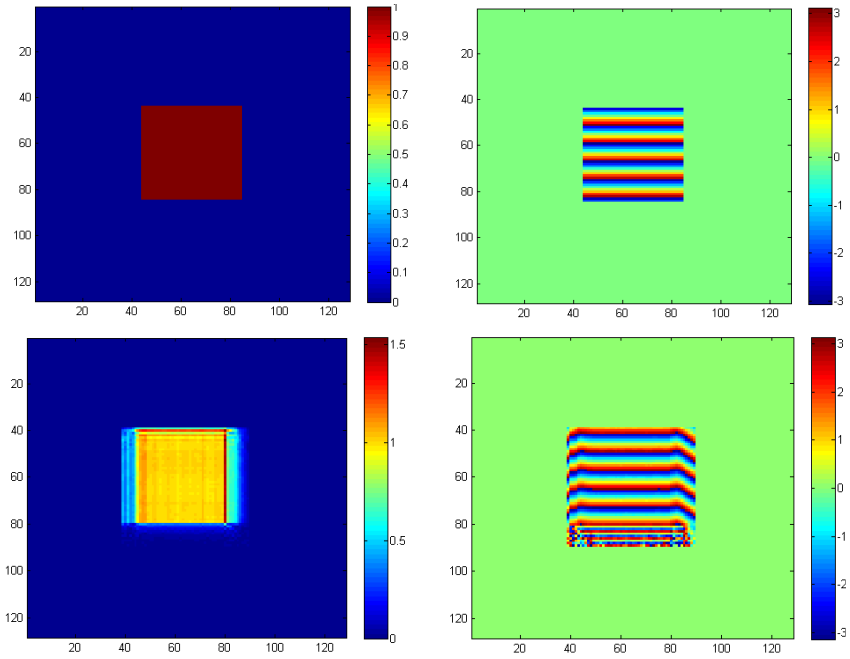

Figure 12 Top Panel: Simulated amplitude and phase; where the support is 2D box with 4 pixels bigger than the original object on each sides of the box. Bottom Panel: Reconstructed amplitude and phase by using ER (500 iterations) + HIO (500 iterations) + ER (500 iterations)

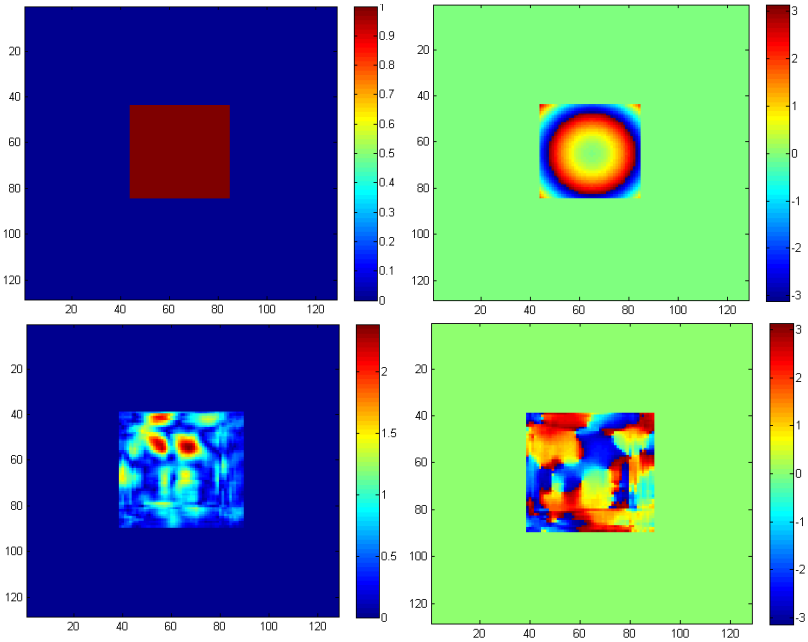

Figure 13 Top Panel: Simulated amplitude and phase of a strong phase structure in 2D; where the support is 2D box with 2 pixels bigger than the original object on each sides of the box. Bottom Panel: Reconstructed amplitude and phase by using ER (500 iterations) + HIO (500 iterations) + ER (500 iterations)

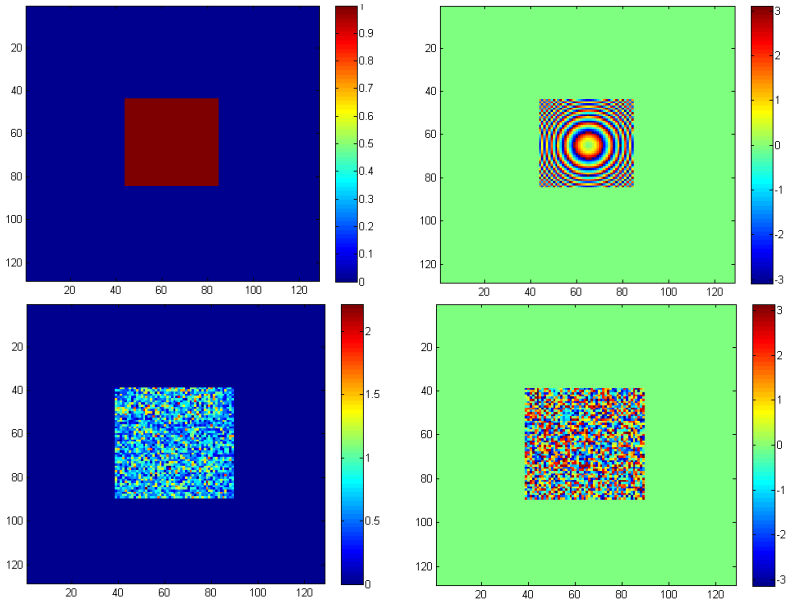

Figure 14 Top Panel: Simulated amplitude and phase of an even stronger phase object with approximately 5 phase wraps; where the support is 2D box with 2 pixels bigger than the original object on each sides of the box. Bottom Panel: Reconstructed amplitude and phase by using ER (500 iterations) + HIO (500 iterations) + ER (500 iterations)

3:6 Simulation studies on Guided-Phase Hybrid-Input-Output (GPHIO) Algorithms with random start

To solve highly strained CDI datasets, a new Guided-Phase approaches has been introduced. Guided –Phase HIO (GPHIO) has utilized prior (approximate) knowledge of the phase structures that are close to that of the actual objects to define an allowed phase range for each pixel, guiding the iterative algorithm to reach data convergence. When the phase ranges are outside the guided ranges, the HIO feedback procedure is performed, in a similar way to that of conventional PCHIO feedback step. Simulation studies on designed highly strained complex objects show that this GPHIO method offers improvements on finding correct-looking solutions.

Fig. 15 illustrates the detailed procedure of GPHIO algorithm with random amplitude and phase start. The phase results after the first cycle of ER-HIO-ER combination are saved and used as starting points for the next ER-HIO-ER cycle.

To start with random guess of electronic density and phase in direct-space of object

$$u_i^n = \left\{ \begin{array}{l} \tau_i,\ i \in Support \\ 0.0,\ \notin Support \end{array} \right\}$$

$$u_i^n = \left\{ \begin{array}{ll} \tau_i & i \in Support \cap \phi > \left(\phi_{\min} + \phi_{result\ of\ current\ iteration}\right) \cap \phi < \left(\phi_{\max} + \phi_{result\ of\ current\ iteration}\right) \\ u_i^{n-1} - \beta\tau_i & i \in Support \cap \phi < \left(\phi_{\min} + \phi_{result\ of\ current\ iteration}\right) \cap \phi > \left(\phi_{\max} + \phi_{result\ of\ current\ iteration}\right) \end{array} \right\}$$

$$u_i^n = \left\{ \begin{array}{l} \tau_i,\ i \in Support \\ 0.0,\ \notin Support \end{array} \right\}$$

New support: reset amplitude to random values but keep the phases of the last results as initial guesses of phases of support;

$$u_i^n = \left\{ \begin{array}{l} \tau_i,\ i \in Support \\ 0.0,\ \notin Support \end{array} \right\}$$

$$u_i^n = \left\{ \begin{array}{ll} \tau_i & i \in Support \cap \phi > \left(\phi_{\min} + \phi_{result\ of\ current\ iteration}\right) \cap \phi < \left(\phi_{\max} + \phi_{result\ of\ current\ iteration}\right) \\ u_i^{n-1} - \beta\tau_i & i \in Support \cap \phi < \left(\phi_{\min} + \phi_{result\ of\ current\ iteration}\right) \cap \phi > \left(\phi_{\max} + \phi_{result\ of\ current\ iteration}\right) \end{array} \right\}$$

$$u_i^n = \left\{ \begin{array}{l} \tau_i,\ i \in Support \\ 0.0,\ \notin Support \end{array} \right\}$$

Figure 15 Algorithms of revised Hybrid-Input-Output with Error-Reduction steps as complimentary analysis.

Fig. 16 clearly show gaps and errors as it might indicate failure of convergence of measurements, and the reconstructed phases show artefacts when comparing with the original designed phases in simulation. These reconstructions were performed with conventional ER + phase-constraint HIO + ER algorithms, with 10 + 10000 + 10 iterations respectively. The result doesn't seem to converge correctly with broken-up

reconstructed density. This is typical example that conventional CDI algorithms fail to work in highly strained cases.

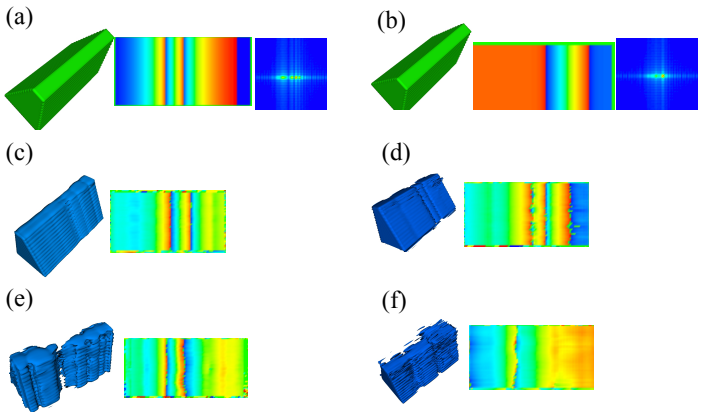

Figure 16 Simulation of complex three-dimensional objects having the uniform density and right hand panel shows the phases, the blue and red colour representing $+\pi$ and $-\pi$ respectively, and the blue-red phase-wraps represent 2 π of phase changes. (a) and (b) are two different simulated amplitude; phase and the corresponding diffraction intensities from left to to right respectively. The right hand side panel is the scalar-cut-plane of phase-values. (c) and (d) are reconstructions (amplitude and phase) by GPHIO algorithm; (e) and (f) are reconstructions by using conventional HIO algorithm with random initial start for both amplitude and phase.

Previous methods reported in the literature for reconstruction with different algorithms for highly strained diffraction patterns on nano-crystalline structures have opened up a new path for better understanding of objects of highly complex wave functions[9,45,46]. Our newly revised HIO algorithm has been tested for simulated datasets, and highly strained simulated data with direct-space phase of up to 8π (which corresponds to 4 phase-wraps) was successfully reconstructed, with both amplitude and phase were in good agreement with initial simulation. This shows significant improvements comparing with results with conventional HIO and phase-constraint PCHIO algorithms. The revised algorithm starts with initial random guesses of amplitude (standard polygon) and phase, followed by standard Error-Reduction algorithm and phase-shrink-wrap (revised) HIO algorithm with

phase maximum and minimum of ½π and -½π respectively. A new complex support is created with amplitudes having values of initial random guesses (standard polygon) and with current values of phases from previous iteration copied to the support. Therefore, the current values of phases are used as guided initial values for the next iteration of revised HIO step. The new HIO algorithm takes the results of the previous phases as initial guesses to be constrained within ±½π for phase values within direct-space object to be reconstructed, alternating with standard ER algorithms to reach final convergence. The revised algorithm performs relatively better than conventional HIO algorithm because it fills the amplitude gaps of the reconstructed direct-space object by allowing phase-ranges to be extended around these regions; with the revised algorithm reconstructions usually converges after 3 steps of revised HIO with around 100 iterations for each step, though sometimes it takes a little bit longer to converge.

3:7 Simulation studies with Guided-Phase Error Reduction (GPER) algorithm

For reconstruction of highly strained complex objects with strong curvatures of phases, random phase start of iterative algorithms will result in completely wrong solutions, with the solutions having no resemblance of the correct answers at all. The reconstructed

phase will most likely result to random phase values in reconstructed phase structures, unfortunately, noise-like features. Introduction of Guided-Phase ER (GPER) can improve reconstructions significantly by constraining direct-space phases within a selected range, allowing for some deviation of phases around the model phases. Fig. 17 illustrates how the GPER works in details.

$$u_i^n = \begin{cases} \text{for } \phi_i > \left(\phi_{\min} + \phi_{\text{FEA simulation}}\right) \cap \phi_i < \left(\phi_{\max} + \phi_{\text{FEA simulation}}\right) \\ \tau_i, \quad i \in Support \\ 0.0, \; i \notin Support \\ \\ \phi_i = \phi_{\min} + \phi_{\text{FEA simulation}}, \quad \text{for } \phi_i < \left(\phi_{\min} + \phi_{\text{FEA simulation}}\right) \\ \tau_i, \quad i \in Support \\ 0.0, \; i \notin Support \\ \\ \phi_i = \phi_{\max} + \phi_{\text{FEA simulation}}, \quad \text{for } \phi_i > \left(\phi_{\max} + \phi_{\text{FEA simulation}}\right) \\ \tau_i, \quad i \in Support \\ 0.0, \; i \notin Support \end{cases}$$

Figure 17 description of Guided-Phase-Error-Reduction (GPER) algorithm, the associated symbols in the description of the algorithm are defined by Ross Harder et al[54].

This method is based on the expected estimation of initial phase models based on various physics models with quantitative calculation, in direct-space regime, and it has some sort of similar principle as one of the Fourier space projection method, the modulus annulus project on measured diffraction intensities[32]. The modulus annulus projection utilizes the fact that due to experimental noises and imperfection of measured data and instrumentations, certain values of inferior and superior bounds are selected to apply to the actual experimental measured intensities.

Fig. 18 shows 3D simulation of complex objects with specifically designed amplitude (uniform) and phase (highly strained) to test robustness of GPER algorithms, with various starting models (or random amplitude and phase starts).

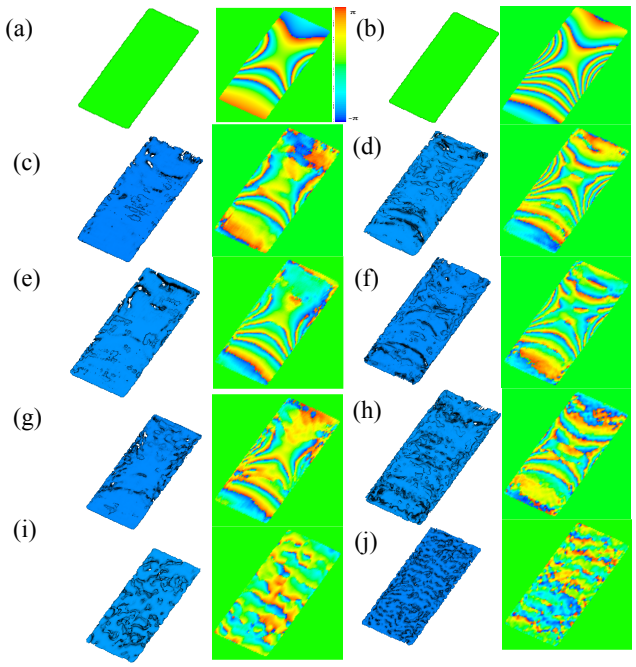

Figure 18 (a) and (b) are designed amplitude and phase of two types of models. The blue/red phase wrap represents phase values when exceeding 2π, the phase scale bars for the following figures are the same in this figure. (c), (e) & (g) are reconstructions with the actual phase and amplitude; slight deviation and large deviation of actual solutions of (a) to start with iterative algorithm, and (d), (f) & (h) are reconstructions with the actual phase and amplitude; slight deviation and large deviation of actual solutions of (b) to start with iterative algorithm. (i) and (j) are reconstructions with random amplitude and phase of direct-space models (a) and (b) respectively

4 Radiation damage of X-rays in materials: theory and importance

The effect of radiation of high energy X-rays, especially those generated from 3rd generation synchrotron Sources has been investigated for a long time. In order to fully utilize the novel capabilities of Coherent X-ray diffraction imaging technique, one has to develop methods to increase best achievable spatial resolution of specimens under study. Theoretically, CDI has sub-atomic resolution potential, however, there are several obstacles need to be conquered to achieve this important goal. To start with this topic, one has to recognize the difference between damage problems in soft condensed matter materials, mostly, biological systems in general, and that of hard condensed matter materials, namely, materials sciences in general. For the former category, one needs to consider and assess the radiation damage incurred during experimental measurements with X-rays. Biological systems are in general very sensitive to radiation damage, and they are considered to be weak scatterers. One usually uses X-rays with energy in the soft regime to study biological specimens by using absorption-contrast based imaging technique, while phase contrast imaging technique is more suitable for hard condensed matter materials. In general, hard-condensed matter materials are highly resistive to radiation damage; on the other hand, absorption contrast imaging of biological specimens could investigate either chemical elements or refractive indices distributions within the specimens, usually by soft X-rays, while hard X-rays penetrate through biological specimens without useful absorption-contrast diffraction patterns produced experiments.

However, the hard X-ray diffraction patterns of biological specimens are still invertible, due to the phase-contrast imaging capability.

Absorption is most important for chemical specificity. Another advantage to using soft x-rays is that you can access the water window that provides a stark contrast between the signal from proteins and the signal from water in an image allowing hydrated samples to be imaged. Hard X-rays do penetrate biological materials but are scattered weakly. However those patterns can still be inverted to get images. In the case of hard x-rays the damage to samples is actually less due to high penetration depth within specimens.

In order to achieve optimum resolution needed for experimental studies, one has to ensure the X-ray dose for measurements is bigger than the minimum required dose for imaging and at the same time smaller than the maximum tolerable dose for a particular biological system in consideration of specific experimental conditions and selected energies of X-ray in each case. To estimate the minimum required dose for imaging, an important paper by Howells[64] uses the Rose criterion for a rough estimation. The Rose criterion[65] states that in order to achieve relatively reliable detectability of a feature against background noise, the signal coming from the feature has to be at least 5 times

bigger than the root-mean-square (RMS) of that of the surrounding background during measurements.

The general method for estimation of dose for required imaging dose is expressed as follows:

$$D=\frac{\mu Ph\upsilon}{\varepsilon\sigma_s}=\frac{\mu Ph\upsilon}{\varepsilon}\frac{1}{r_e^2\lambda^2\left|\tilde{\rho}_r\right|^2 d^4} \quad \textbf{Equation 31}$$

Where $h\upsilon$ is the energy of incident X-ray, σ_s is the coherent scattering cross-section of 3D unit volume, called 3D voxel of experimental specimens, ε is the density of object, μ is the intensity absorption coefficient, P is the number of X-rays scattered into the detector from a given voxel (three-dimensional pixel), r_e is the classical radius of an electron, $\tilde{\rho}_r$ is defined to be the complex electron density, and d is the size of single voxel d x d x d in each dimension.

The cross-sections of coherent X-ray scattering, which is proportional to the fourth power of pixel resolution is expressed as follows;

$$\sigma_s=r_e^2\lambda^2\left|\tilde{\rho}_r\right|^2 d^4 \quad \textbf{Equation 32}$$

The requirement for minimum imaging dose is defined as $N_0 = \frac{P}{\sigma_s}$, where N_0 is the total number of incident X-ray per unit area. This estimation leads to the total number N_0. Because the minimum required dose for experiments is inverse proportional to the cross-section of X-ray coherent scattering, the best available spatial resolution and available integrated photon flux has an inverse fourth-power scaling law relationship.

$$N_0 = \frac{P}{r_e^2 \lambda^2 \left|\tilde{\rho}_r\right|^2 d^4}$$ .Equation 33

The studies utilized the weak-phase-weak-amplitude approximation, provided the fact that the pixel size of best resolution is intrinsically small.

Qun Shen et al[66] have demonstrated that approximation of particles of being 3D spherical geometry yields 3rd power relationship between the best available spatial resolution and coherent X-rays scattering cross-section. They used ensemble-averaged formulation by evaluation of unit 3D volume element as a sphere.

For maximum tolerable radiation dose, a number of measurements have been performed since 1970s, some important results are presented in a table for various X-ray energy range, experiments and samples[64].

For hard condensed-matter materials in general materials sciences, the samples are usually quite tolerant of high-energy X-ray exposure. The best achievable resolution is usually limited by the available coherent flux or more precisely the fluence from a synchrotron source. Fluence in synchrotron X-ray science is usually defined as the integrated electromagnetic radiation energy delivered per unit area per unit time, from a synchrotron source.

This may imply that the rate of increase of spatial resolution of imaging is much slower than the rate of increase of available integrated X-ray flux in an X-ray source. Although for hard condensed-matter materials, radiation damage does not impose a problem for achieving sub-atomic resolution in CDI, the need for ultra-intense coherent X-ray source becomes a necessity for future development of CDI. Larger total integrated available flux may result to more available information on high scattering angle diffraction intensities, leading to much higher spatial resolution in data inversion in CDI, and the diffraction-limited theory could be tested in principle. However, because of the inverse fourth-power

scaling law, one may question on whether there are some alternatives for achieving better spatial resolution for strong scattering hard condensed matters. One of the prominent solutions is to develop better X-ray focusing optics, such as high-resolution KB mirrors[26]. The flux density on the sample can be drastically increased due to small focusing spots, which would help to obtain sufficiently high photon signals for high-angle scattering in reciprocal diffraction intensities. In this way, best-achievable spatial resolution can be significantly improved by using a 3rd generation synchrotron source. Higher resolution capabilities in CDI enable understanding of atomic structural/deformation mechanisms to be studied aiming at much better understanding of physics and chemistry of fundamental behaviors in materials.

Furthermore, due to the fact that for most hard condensed-matter strong scattering materials, the penetration depth increases with increasing incident X-ray energies, thus the overall three-dimensional illumination volume increases with increasing energy of incident X-ray. The surface dose, which is defined as X-ray energy deposited per unit mass decreases with increasing incident X-ray energy. The radiation damage per unit volume is less for higher energy of incident X-ray, but the diffraction signal is weaker too. This is of particular of interest for general strong-scattering materials, where radiation damage may become an issue when longer X-ray exposure time is required for measurements, especially for three-dimensional imaging techniques, such as Transmission X-ray Microscopy. The trade-off relationship between maximizing X-ray

coherent scattering cross-section of and minimizing X-ray radiation damage leads to further work on selection of suitable X-ray energies for specific measurements with particular techniques. X-ray free electron laser source (X-FEL) aims to remove the radiation damage problem by creating a high fluence femto-second pulse that can take a diffraction pattern before the sample is destroyed by the radiation damage of the passing pulse.

Recent studies on radiation-induced effects on crystalline protein structures have suggested that the amount of radiation damage has almost the same regardless of the lengths of the femto-second coherent X-ray pulses for experimental measurements at LCLS[67]. This might indicate that crystalline protein structures can in principle withstand much more radiation doses than previously thought[68].

Simulation studies on X-ray radiation damage[69] by various mechanisms such as photoelectric; elastic or Compton scatter, each of which has specific cross-section, through the mechanism that X-ray depositing energy directly into specimens. In the case of the main source of radiation damage contribution, the photoelectric effect, X-ray florescence or Auger effects are produced with specimens with heavy elements or light elements respectively.

Studies show that the main mechanisms for X-ray damage are specimens' mass loss and decrease in organic chemical bond density. By using Cryogenic approach, such as

freezing of biological samples, prevention of mass loss can be effective but preservation of chemical bonds is less effective[70].

Howells et al have illustrated[64] the relationship between required doses for X-ray imaging vs. attainable resolution, which shows a roughly linear dependence on a log-log plot, shown in Fig. 19, with better resolution with increasing required level of X-ray doses. The relationship between maximum tolerable doses for imaging for various techniques, such as electron crystallography for various biological structures are presented and compared with that of X-ray related techniques. Systematic studies are required for better understanding of achieving the best spatial resolution while keeping the radiation doses below the maximum tolerable dose amount. In the mean time, experimental data have to be of sufficient quality and signal-to-noise ratio (SNR) for determination of useful structures of specimens of interest.

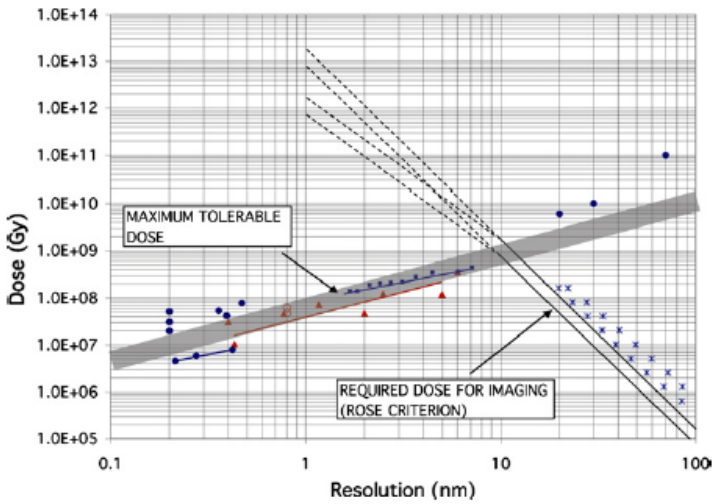

Figure 19 Tolerated dose vs. required dose for various X-ray and Electron crystallography related techniques. Image comes from [64]

Fig. 19 illustrates experimental analysis showing tolerated dose vs. required dose and highlight that this gives a maximum resolution of 10nm for CDI techniques in biology. For hard matter samples the tolerated dose is much higher therefore the maximum achievable resolution will be <10 nm.

Neutrons interact with the atomic nucleus of samples, while X-rays interact with the electrons, The damage mechanism of X-rays and neutrons are very different. Since neutron radiation interacts directly with the nuclei, damage arises because atoms will be displaced, often in cascades, resulting in structural modification of the materials. On the other hand, X-rays produce electrons cascade effect within specimens, resulting in ionization of atoms in the system, so damage arises when atoms will become displaced by Coulomb forces. Neutron radiation damage is more relevant for hard-condensed matter materials, since their energies are much higher than X-rays, which are electromagnetic radiation produced in Synchrotrons. however, despite the differences in interaction mechanisms between the two, both X-ray and neutron irradiations have similar effects on the specimens. It is therefore useful to review the extensive studies of neutron-irradiated materials, which were undertaken for the safe exploitation of nuclear power.

Radiation damage mechanisms on hard-condensed-matter materials have been a popular topic, and radiation damage of metals such as steels with high-energy neutron or ion

bombardments are studied in great details by both theory and experiments[71-73]. The origin of the radiation damage by high-energy neutron irradiation may be the dissipation of recoil energy by atoms that are initially collided with high-energy incident neutrons, and the initial atoms in the system transfer their kinetic energy to other atoms, producing cascade displacements within the system, until all the initial kinetic energy is dissipated to the system. When the energy transferred to the initial or subsequent atoms is greater than that of the binding energy, atoms could be displaced and excited into higher energy states, leaving behind vacant sites as defects, which are called vacancies. Excited atoms arrive at higher energy states as interstitials within the lattice, and they are also considered to be defects. Together with vacancies they leave behind once they are excited, they combine to form Frenkel pairs. The rate of Frenkel pairs formation in a specific system as a function of initial energy transferred to an atom when collided with high-energy neutron or ion particles can be calculated and modeled with a number of approximations.

Experimental studies show that[74] when Xenon ion irradiation has reached the level of 1.5×10^{15} ions/cm^2, dislocation loop formation network has become evident, although the microstructures under study have been maintained upon higher level of Xenon ion exposure. Furthermore, cavities of forms of bubbles and voids kinds are also observed at this level of ion irradiation, the origins of which have been investigated by Kinetic Monte Carlo simulation.

Stoller has described[75] detailed information on methodologies of various simulation techniques for estimation of the behaviors of displacements cascades produced with radiation damage.

5 Strain effect in semiconductors: band structure modifications and transport mobility

Since Silicon and Germanium are indirect-band-gap semiconductors, direct excitation of valence electrons without doping into n or p-type semiconductors would not produce conduction current. N-type semiconductors are produced by addition of certain impurities that produce extra free electrons that add an extra energy level just below conduction band edge, directly below Fermi-level. Therefore, electrons in the new energy level can be easily excited into conduction band, creating electrical current. For p-type semiconductors, extra energy level is created near the valence band edge, directly above the Fermi-level, thus extra holes can be left behind, resulting in hole current, when electrons from the valence band are excited into conduction band. Fig. 20 shows the electronic band structure illustration of introduction of doping in semiconductors, which produce either N or P-type semiconductors.

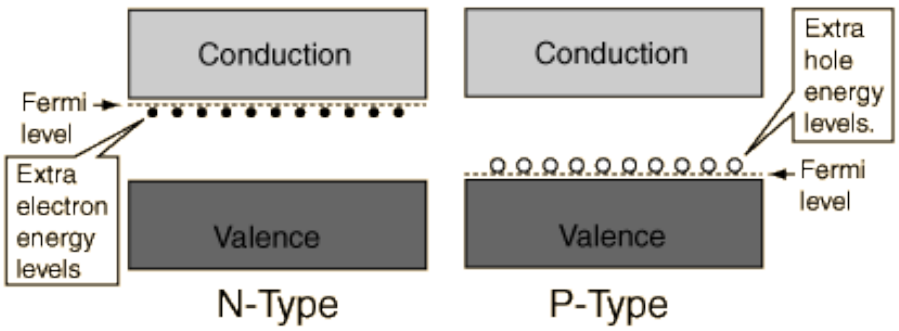

Figure 20 Band Structure of n and p-type doped semiconductors. Image comes from http://hyperphysics.phy-astr.gsu.edu/hbase/solids/dope.html

Paul Drude proposed a simple model[76] [77] in the early 20th century to describe the transport properties of electrons in metals in a classical way, neglecting all quantum mechanical effects. His model gave a simple description of an electron scattering mechanism upon introduction of a constant and uniform electric field. The drift velocity of those electrons is lost during scattering processes; in the meantime, electrons are accelerated due to the electric field, resulting in further scattering processes and a net flow.

The scattering rate, which is the probability of an electron scattered from two different states, $\psi_{E,k}$ to $\psi_{E',k'}$ is dependent on a number of different factors. The scattering coupling strength, the state overlap factor and the availability of the final state all contribute to the final description of the electron-phonon scattering rate. The scattering coupling strength, described between initial and final states can be stated as follow:

$$C_{q,b} = \int \psi^*_{E',k'} H_{q,b}(r) \psi_{E,k} \, dr \quad \text{Equation 34}$$

where $H_{q,b}(r)$ is the phonon-electron interaction, the subscripts q and b describe specific phonon frequency and phonon branch respectively.

The state overlap factor can be illustrated as follow:

$$\mathrm{I}(k,k') = \int_{\text{unit cell}} \psi^{*}_{E,k'} \psi_{E,k} \mathrm{d}r \quad \text{Equation 35}$$

Fig. 21 shows a typical Silicon indirect electronic band structure without doping effect and other possible modifications of the structure by external stimulus. Due to the fact that Silicon has indirect-gap electronic band structures, several bands are present in the energy-momentum dispersion diagram as shown in Fig. 21. Three of which have their maximum values below the energy at the top edge of the valence band, and two of the three bands have maximum values at 0eV, namely the heavy and light-hole bands, with association of heavy and light-hole effective masses respectively. The third band in this group has maximum energy of -0.044 eV, and the corresponding effective mass called the split-off hole effective mass.

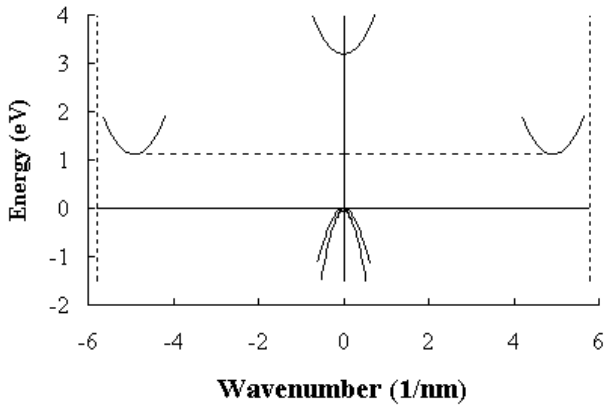

Figure 21 Schematic diagram of the band structure of Silicon. Image comes from: http://ecee.colorado.edu/~bart/book/effmass.htm

Electron states in silicon are composed of all these three different hole states. To account for scattering between heavy-hole and light-hole in valence bands of semiconductors, the angle between the two wave-vectors of heavy-hole and light-hole has to be considered into calculation.

Estimation of the availability of the final states can be calculated by evaluation of the density of state (DOS) of final electron states. Since phonons are bosons, they follow Bose-Einstein statistics, which can be described by the following expression:

$$n(\omega_{q,b})=\frac{1}{\exp(\hbar\omega_{q,b}/k_B T)-1} \quad \text{Equation 36}$$

Where $n(\omega_{q,b})$ is the expected number of particles in an energy state of $\omega_{q,b}$; $\hbar\omega_{q,b}$ is the phonon energy with wave-vector of q in the phonon branch b, and k_B is the Boltzmann constant. The total scattering procedure is composed of phonon absorption and emission, and the scattering mean free time, which is the mean time interval that electron being scattered between two adjacent scattering events as explained previously is inverse of the phonon scattering rate $S(k)$.

The scattering rate is proportional to the summation of probability of all the possible transition rates of an electron from initial state to final state, which can be described in the following way,

$$S(k) = \sum_{k'} P(k, k') = \frac{2\pi}{\hbar} \sum_{k'} \left| \langle k' | H_1 | k \rangle \right|^2 \partial \left(E_{k'} - E_k \right) \quad \text{Equation 37}$$

Where H is the Hamiltonian of the system, and it can be of the form of various kinds, unperturbed or energy-dependent perturbed. $P(k, k')$ is the probability of each individual transition, the summation is over all the possible transitions. The final expression of scattering rate of an electron in a state with energy and phonon wave-vector E and k respectively evaluated by using Fermi's golden rule is:

$$W(k) = \frac{V}{8\pi^2 N M'} \int \frac{C_{q,b}^2 I(k,k')^2}{\omega_{q,b}} \delta_{k \pm q - k', K} \times (n(\omega_{q,b}) + \frac{1}{2} \mp \frac{1}{2}) \delta \left(E_{K'} - E_k \mp \hbar \omega_{q,b} \right) dk$$

Equation 38

Where V is the crystal volume, N is the number of unit cells in the crystal, M' is the reduced mass for the carriers, q is the phonon wave-vector, which is equal to the momentum difference of an electron that undergoes an energy gain after being inelastic scattered by phonon $k' - k$, $n(\omega_{q,b})$ is the probability of absorbing or emitting a phonon

(see Eqn. 38), i.e. the phonon density for absorption as illustrated previously, and δ is the Kronecker delta operation, I (k',k) is the state overlap function (see Eqn. 35) and C(q',b) is the coupling strength (see Eqn. 34).

Various types of scattering processes contribute to fluctuation of momentum relaxation rate, leading to carrier mobility change, both for electrons and holes. Those various scattering processes include lattice scattering, acoustic phonon scattering, piezoelectric scattering, optical phonon scattering, polar optical phonon scattering and impurity scattering, surface roughness scattering.

In order to calculate the electron mobility by using Drude's model, one needs to consider the relationship between the drift velocity of electrons and the scattering rate of electrons (number of times for an electron will be scattered in a unit time) at equilibrium state when the momentum loss rate is zero.

The momentum loss of electrons being scattered in a unit time period is time-dependent and becomes zero when equilibrium state is reached. At equilibrium state, the drift velocity of electrons can be calculated as follows:

$$v = \frac{eE}{mP} = \frac{e\tau}{m}E$$ Equation 39

where e is the electron rest charge, E is the electric field, P is the scattering rate of electron, and τ is the mean time interval between two adjacent scattering events, and m is the classical rest mass of the electron.

The electron drift velocity is proportional to electric field with proportionality variable being the electron mobility μ, the relation can be stated as:

$$v = \mu E$$ Equation 40

Substituting from Eqn. 39 can be defined as follows;

$$\mu = \frac{e\tau}{m}$$ Equation 41

The effective mass can be evaluated by fitting of a paraboloid around either the minimum of the conduction band or the maximum of the valence band of the energy-momentum dispersion relation diagram.

Application of strain can have various effects on the electron/hole transport in semiconductor devices, thus electron/hole mobility can be significantly changed due to the alteration of electron/hole effective mass and momentum relaxation time. The former

alteration is caused in a number of different ways. The major causes are carrier repopulation between bands in the structure due to degeneracy lifting; and the modification of band structure by strain which induces band warping. Band warping is the effect when strains modify the edges of the band structure in the electronic band structure diagram. The latter can be caused by reduction of scattering rates of various origins, such as phonon scattering reduction by modification of electron-phonon coupling rate, as well as other scattering mechanisms such as impurity scattering, lattice scattering and piezoelectric scattering etc. Strain could have effects on scattering rate of various origins, and this may lead to increase or decrease of scattering rate, which in term would probably have effects on carriers' mobility.

The underlying mechanism for variation of momentum relaxation time due to change of rate of various scattering mechanisms in semiconductor by application of strain can be attributed to the fact that the density of state (DOS) of carriers is altered, resulting in change in the scattering coupling strength, for example, the scattering coupling strength of electron-phonon coupling.

Resistivity in semiconductors is inversely proportional to mobility, therefore, application of strains can cause piezoresistivity effect due to change of mobility of carriers caused by modification of semiconductor band structure by applied stresses. Piezoresistivity[78,79] is

defined to be the ratio of resistivity change to the original resistivity value, and it is a vector tensor form.

One of the two major factors contributing to the carriers' mobility change in semiconductors caused by introduction of strains is the change of effective mass of electrons or holes, and subsequently, the valence band warping and shifting[80-83]. The electron effective mass change is due to the change of density of state (DOS), which is mainly induced by electron piezoresistivity. Electron piezoresistivity is most significant in semiconductors with multivalley conduction bands: semiconductors that have indirect band gaps, for example Silicon and Germanium etc[84]. However, the piezoresistivity generated by conduction band warping due to strain is relatively small compared to the piezoresistivity of holes.

Hole conductivity effective mass and hole transport in semiconductors is different from that of electrons. The band warping caused by strain in conduction bands for electron transport is relatively insignificant compared with the band warping effect for hole transport. However, the true nature of this difference between electron and hole transport caused by the same strain effect still needs to be investigated by detailed calculations, with which the effective mass of electrons and holes, as well as the modification of density of state (DOS) needs to be studied.

A number of experiments[82,85-87] suggest that electron mobility can be significantly improved by introduction of strains, although the amount of mobility increase cannot be simply explained by the combination of electron transport modification due to effective mass reduction and the reduction of phonon scattering of various origins. Additional contributions have to be considered in accounting for the observed electron mobility increase. One of the additional factors is the possibility of the reduction of surface roughness leading to surface roughness scattering suppression caused by in-plane tensile stress with applied strain in an actual MOSFET devices.

Application of various types of stresses can result in different changes to the carriers' effective mass, shift of the band edge, as well as warping of the valence band edges, and piezoresistance. Studies have shown that uniaxial stress along [110] direction has effect of warping the [001] band valleys.

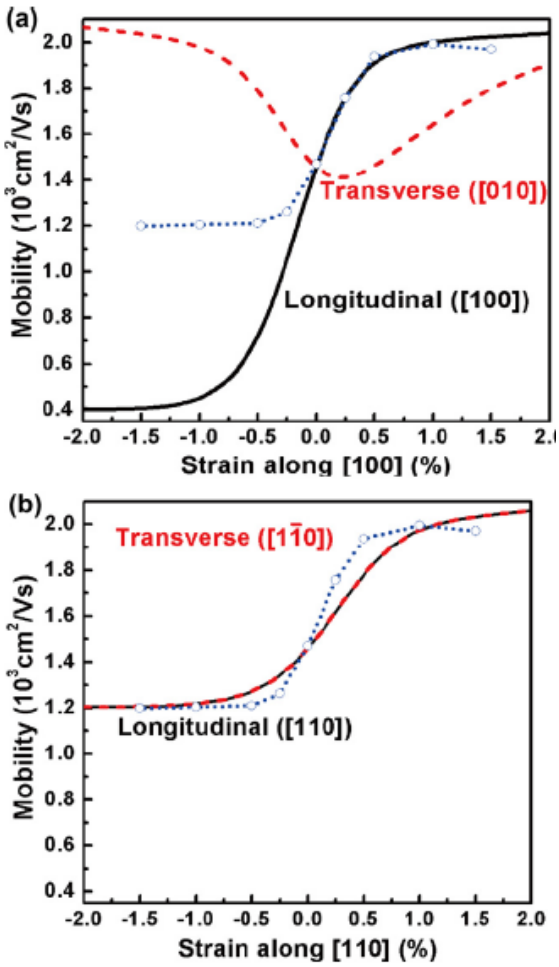

Figure 22 Calculated mobility as a function of uniaxial strain, the solid and dashed lines are for the longitudinal and transverse mobility. Figure comes from[87]

Carrier mobility is a useful predictor of electron/hole transport if and only if the lateral electric field within the devices is relatively low. When the lateral electric field is high, phonon scattering becomes extremely significant, and the semiconductor band structure becomes non-parabolic, both of which would cause saturation of carrier drift velocity. The relationship between carrier transport and mobility is linear in the low lateral field region, but in the high field region, carrier transport, which is determined by carrier drift

velocity becomes saturated above a certain lateral electric field strength. The carrier mobility and the high lateral electric field have the following relation;

$$\mu = \frac{e\tau_0}{m^*} = \left(\frac{\hbar\omega_0}{m^*}\right)\frac{1}{E} \quad \text{Equation 42}$$

Where e is the electron charge, τ_0 is the relaxation time of interaction between electrons and optical phonons, m^* is the effective conductivity mass of electron, $\hbar\omega_0$ is the associated phonon energy at specific electric field, and E is the lateral electric field.

The mobility is now inversely proportional to lateral electric field in the high field case. To apply the linear relationship between drift velocity and lateral electric field into the expression (see Eqn. 43), the drift velocity now becomes a constant value and it reaches saturation.

$$\upsilon_d = \mu E = \left(\frac{\hbar\omega_0}{m^*}\right)^{1/2} \quad \text{Equation 43}$$

It is still under intense debate on whether strain could improve the semiconductor device performance under high lateral field scenarios, when carrier drift velocity saturation occurs[88]. The two known major contributions to the enhanced carrier mobility are reduction of conductivity mass leading to better carrier transport, and the suppression of electron-phonon and other various kinds of scatterings within the devices. Whether

application of strain in devices leading to suppression of scattering is a major factor contributing to carrier mobility enhancement at high lateral electric fields has any effect on performance enhancement is still an open question.

Further investigations still need to be done to be able to understand the underlying mechanisms between carrier mobility enhancement and strain.

Further study of strain-induced effects on major industrial semiconductors, such as silicon, germanium, and GaAs, particularly with various doping introduced, can be of great interests in both semiconductor industry and fundamental condensed matter physics in general. With intense new research undergoing on in alternative/organic semiconductor devices because of the ultimate limits of conventional semiconductor materials due to the widely recognized Moore's scaling law, one needs to first understand fundamental principles on how conventional semiconductors defects/impurities/band structure modifications could influence observed improvement on devices performance. Future studies with various techniques such as high-resolution electron microscope, and hard X-ray diffraction imaging etc. could shed a light on better understanding of conventional semiconductor devices, especially their performance mechanisms under extreme conditions, such as high pressure and high temperature.

Strains may result in changes in the scattering rates of various origins in Silicon based semiconductor devices, which might lead to enhanced or reduced electron or hole

mobility. By using CDI and Bragg-geometry Ptychography, we envisage the physics mechanisms of this evolution of carriers' mobility in Silicon based semiconductor devices, as a function of strain can be better understood. Ultimately, manipulation and fine-tuning of carriers' mobility could be potentially achieved by adjustments of applied external stresses, which would produce strain of desirable amount, and all of which can be imaged by CDI and Bragg-geometry Ptychography, by using state-of-art 3rd generation synchrotron facilities and X-ray free electron laser sources worldwide.

Strain in nano-scale devices is a relatively new subject, whether the strain effects in nano-scale devices is fundamentally different from that of the bulk counterpart is not to be demonstrated with experimental results. Our recent study shows Bragg CDI is a promising technique for characterization of nano-scale devices, with improved spatial resolution and X-ray beam stability, BCDI is expected to provide better quantitative results for devices in nano-scale.

IBM has recently successfully registered a patent application on method to control source/drain stressor profiles for stress engineering[89]. The strains induced by external stresses may have imperative importance in semiconductor devices industry, although more studies are needed for quantitative analysis of the effects produced by introduction of a stressor. Fig. 23. shows a typical example of a SOI/Si_3N_4 stressor cross-sectional layout. Si_3N_4 liner stressor is used to transfer stress into the SOI layer underneath,

resulting to strained state of the SOI layer. It is expected that the strains produced in this way can increase device carriers' mobility, thus improve device performance.

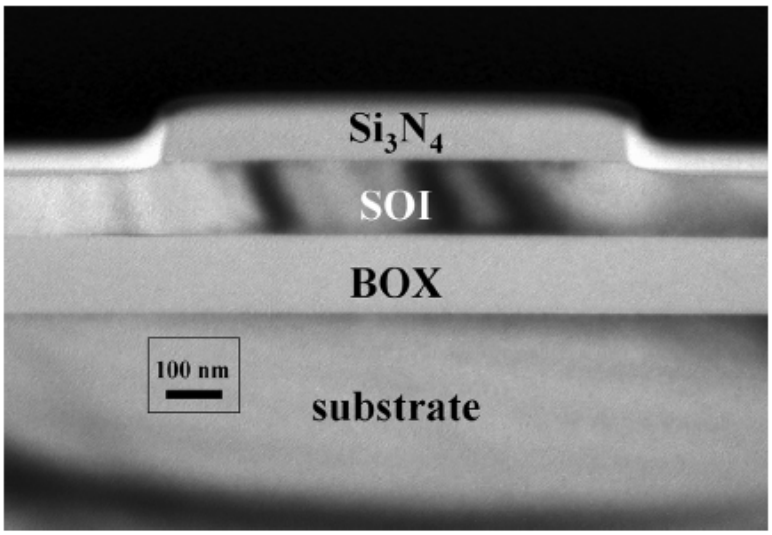

Figure 23 Cross-sectional TEM image of the edge of the SOI/Si_3N_4 stressor structure. Image comes from[90]

6 CDI Experimental work on SOI wafer

We have performed systematic studies of various SOI wafers, aiming at good understanding of strains within SOI due to wafer nano-fabrication processes. We discovered that SOI wafers are in general not homogeneous in strains, and in some cases, significant amount of strains were observed in our measurements. All experiments were done at 34-ID-C at APS.

6:1 Introduction of SOI wafer measurements by using CDI at 34-ID-C at Advanced Photon Source

Coherent X-ray diffraction (CXD) experiments on various SOI wafers were performed during 2010 at APS for better understanding of microstructures of un-patterned SOI wafers. Characterization of SOI wafers by micro-diffraction using coherent hard X-rays provides direct mapping of strains/variation of microstructures within SOI wafers. Silicon-On-Insulator (SOI) technology has been widely recognized as a major industrial breakthrough during the past decade, offering significant improvements of metal–oxide–semiconductor field-effect transistor (MOSFET) device performance. This is measured in terms of lower power dissipation, higher switching frequency and lower parasitic capacitance. SOI based MOSFETs are considered to be one of the best alternatives to conventional bulk-Silicon MOSFET technology, however, fabrication of SOI wafers are significantly more technologically challenging as the dimensions of the devices shrink

dramatically[91]. State-of-Art lithography-based fabrication techniques[92] are starting to be employed to overcome the possibility of strain arising from SOI fabrication[93].

Various methods are used to fabricate Silicon-On-Insulator wafers: hetro-epitaxy, Separation by Implantation of Oxygen (SIMOX) [94,95]and wafer bonding followed by Smart Cut™ technology[96,97]. The SIMOX technique is particularly widely used due to relatively low crystal-defect density, low variation of film thickness and high crystalline-quality leading to high-quality wafers with high charge-carrier mobility. The SIMOX process involves Oxygen ion implantation onto single-crystalline Silicon wafers, during which oxidation occurs; a subsequent high-temperature annealing process recovers the high-quality crystalline structure of film. Smart Cut™ technology involves transferring high-quality single crystalline Silicon thin layer from wafer to wafer after bonding, and is followed by annealing and final polishing processes.

Microstructure of SOI wafers fabricated by various methods might be different; we have also observed that the micro-diffraction patterns vary at different positions on SOI wafer specimens. In many positions along the scan, there was just a single peak recorded, which varied in position on the detector, while in the positions highlighted there were two or even three peaks seen.

With SOI technology, there is concern that crystalline defects and lattice imperfections might cause various problems for high performance devices, by shortening the device

lifetime or reducing the efficiency of performance. This invites the use of high-resolution X-ray diffraction methods. In previous work, SOI bare wafer structure; highly-strained SOI and Strained-Silicon-On-Insulator (SSOI) nanostructures have been studied and characterised by coherent X-ray diffractive imaging technique[45,46,98,99]. SIMOX material is unsuitable for the experiments because the device and substrate "handle" layers would be exactly aligned, so signal from the thin film would always be swamped by that of the substrate.

6:2 Methods of Experiments

All measurements were performed by scanning a focussed 8.902keV X-ray beam across the sample while recording the diffraction pattern of an off-specular 111 reflection on a direct-detection CCD detector positioned 1.8m away from the sample. A grazing incidence angle of 5º was employed. The beam was focussed by Kirkpatrick-Baez (KB) mirrors to a probe size of about 1.5 microns and was made coherent by entrance slits of 10x20 microns placed before the mirrors. The beam was scanned along the direction parallel to the SOI surface and perpendicular to the beam direction (called "X" here) to study the variation of topography and mosaic structure of a typical SOI wafer.

Three-dimensional rocking curves are measured at a particular Bragg reflection of Silicon by rocking specimen around ±0.5 degrees with incidence angle of around 0.5 to 10 degrees. The angle of incidence can be optimized depending on the spacing between adjacent nanostructures and experimental purposes. Generally, higher incidence angles result in smaller X-ray beam footprints, which in turn reduce the scattering and interference effects of two or multiple samples under the X-ray beam illumination volume, if that is more desirable for measurements. Also, if the nanostructures to be measured are composed of the same materials and have the same crystal orientations, signal-to-noise (STN) should be maximized to ensure good quality of diffraction data. To achieve this, it was recently discovered that with higher incidence angle, the substrate-related Crystal Truncation Rod (CTR) contribution to the diffraction intensity, which is usually undesirable, could be substantially decreased, by reducing the substrate illumination area of the X-ray beam resulting to less CTR signals in diffraction data. As a result, the Signal-to-Noise-Ratio (SNR) could be improved leading to better data reconstructions in analysis.

6:3 Results of Experiments

The results show strong variations of the centre of the rocking curves with splitting and de-splitting of peaks along this particular scanning path. The variations of positions of the peak maximum were due to surface topography or structure inhomogeneity of the SOI

wafer, which might be a direct consequence of the film-transfer steps of the wafer fabrication procedure. Since it is possible the defects could affect the electrical properties of the material, it would be useful to apply this method as a routine diagnostic of the film transfer procedure.

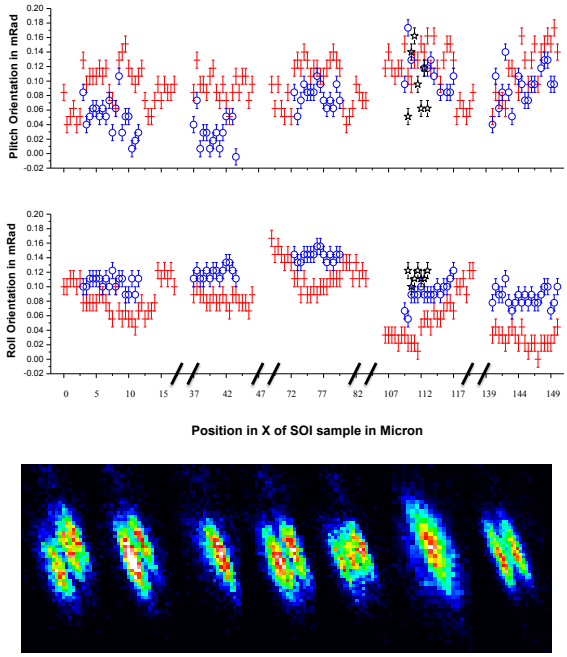

Figure 24 Micro-beam diffraction of a typical SOI wafer. Upper panels: Roll(X direction) and Pitch(Y direction) orientations vs. position along X direction. The red, blue and black symbols represent the various positions of the peak maxima on the CCD. Some points where only a single peak was present have been removed. The pitch direction deviation is slightly bigger than that of the roll direction. The scan was performed with 5° of incidence angle, and 1800mm distance between the CCD detector and the specimen on the off-specular (111) reflection. Bottom panel: appearance on the CCD of micro-beam diffraction patterns at various X positions separated by around 9 microns. The intensity scales are the same for all patterns in the bottom panel. Figure is from [98]

Fig. 24 shows key features extracted from the micro-diffraction measurements, after removal of positions, which showed little variation. The (x,y) position on the detector was converted into (roll,pitch) angular motions of the crystal lattice planes. The same scan performed on a standard Si(111) wafer showed no variation of peak positions, so the observed effect is not a property of the mechanical scanning stage (Newport model MFA) or other instrumentation. The typical distance in X-position from one-peak to two-peak of diffraction patterns or two-peak to three-peak is around 10 steps (5μm), which indicates that an average feature size is about 5μm. A similar scan along the Y-direction showed very little variation of diffraction patterns, presumably because the X-ray beam footprint along that direction is much longer, about 15 μm.

6:4 Discussions of the Results

There are two main explanations for the observed peak-splitting patterns of X-ray micro-diffraction on our SOI wafer samples. Firstly, When mosaic blocks structures of SOI wafers are assumed, the peaks arise from the specific positions of the mosaic blocks within the whole structure; in this case it is the summation of the diffracted intensities which can be very different for adjacent locations due to the variation the orientations of mosaic blocks. This would be expected to give abrupt jumps in otherwise straight lines tracking the peak positions, as illustrated by the solid lines in Fig. 25.

Splitting of peaks into two or three occurs when two distinct orientation are present in the sample at the same time. In a simple incoherent-beam model, the presence of two distinct

peaks, rather than a smeared distribution, would mean that there is a sharp boundary between the grains, as in the classical picture of mosaicity. If clean fractures were present, passing right through the film, as suggested, this might have consequences for the electrical properties of the material. Mosaic structure in thin film single crystalline Silicon would be accompanied by dislocations or lattice faults between the crystal grains.

A coherent X-ray entering more than one mosaic block would result in interference patterns, resulting from linear superposition of the diffracted waves. This leads to an alternative explanation of the splitting of peaks because the contributions of neighbouring grains add coherently. Even if there are continuous variations of orientation between strained regions of single-crystalline structure, distinct peaks will arise because of the coherence. In a general way, the splitting of peaks can be modelled by a spatial variation of real-space phase, which can be linear ramps, parabolic or more complex phase variations. An active field of research is looking into the kinds of phase structure that can explain complex mosaic structures by coherent X-ray diffraction.

The dashed lines in Fig. 25 show schematically what we expect would happen under coherent X-ray illumination conditions. As interference effects turn on there would be a gradual shifting of the peaks, along with intensity variations. Even abrupt boundaries between undistorted mosaic blocks (as illustrated) would lead to smooth variations in peak position. In Fig. 25 we see smooth evolution of the peak positions, but this does not

allow us to tell whether the boundaries between mosaic regions of our SOI sample are abrupt or continuous.

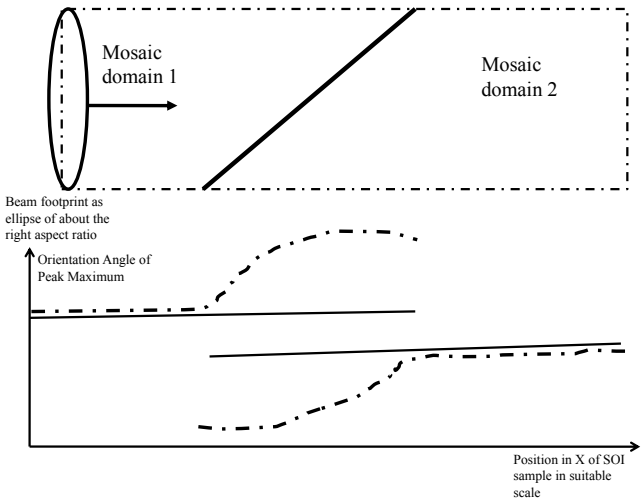

Figure 25 Illustration of the coherent and incoherent limits of diffraction from two overlapping mosaic grains. Upper panel: The black dotted line represents the edge of the object under study. The diagonal line represents a grain boundary separating two crystal mosaic blocks adjacent to each other. Lower panel: lines representing the positions of the peak maximum of diffraction patterns as a function of location of such a multi-grain crystal. The solid and dashed lines represent the expected variation in the fully incoherent and coherent limits respectively. Figure is from [98]

6:5 Conclusion of Experiments

In conclusion, we observed that structures of SOI wafers are in general not homogenous as evidenced by a large amount of structural distortion seen in our micro-diffraction patterns. Two versions of detailed explanations on the physical nature of the peak-splitting micro-diffraction patterns observed in our experiments are illustrated and discussed in the previous sections in this chapter. Coherent X-ray diffraction is a useful technique for direct probing structural inhomogeneities of large-scale single crystalline

structures. When combined with CDI, Bragg-geometry ptychography can be a unique technique for quantitative structural analysis of single crystalline materials of industrial and scientific interests.

7 Coherent X-ray Diffractive Imaging measurements on highly strained SOI nanowires, theory and experiment

7.1 Radiation induced bending of Silicon-On-Insulator nanowires probed by coherent X-ray diffractive imaging

7:1:1 Introduction of Experiment

We have performed CDI experiments at 34-ID-C at APS in which we observed radiation-induced bending of SOI nanowires. One aim of the work is to understand how X-rays radiation affects potential SOI devices. This study is quite time-consuming and the overall experiments took about 2 days of beamtime at 34-ID-C. Several lithographically-produced Silicon nanowires were studied, and the effects of X-rays exposure were very similar, and the thickening Silicon Dioxide layer were observed in all Silicon nanowires, as measured with the (111) Bragg peak on the device layer.

7:1:2 Method of Experiment

The samples were aligned on the off-specular (111) reflections with an incidence angle of 1 degree, and the CCD detector with 20 μm pixels was placed 1.2 meters away from the sample at the correct Bragg angle, theta. Three-dimensional rocking curves were

measured at a particular Bragg reflection of Silicon by rocking specimen around ±0.5 degree in theta steps of 0.005 degree so that oversampling conditions in all three reciprocal-space spatial dimensions satisfied.

7.1.3 Results and Simulation of Measurements

Fig. 26 shows a series of measured diffraction patterns with increasing X-ray illumination dose on a typical SOI nanowire (with spatial dimensions of 1.5μm X 800nm X 170nm). The peak shape is three dimensional in the space of ($X_{detector}$, $Y_{detector}$, θ), so the views shown are two-dimensional scalar-cut-planes in the direction of greatest elongation. It can be clearly seen that the central peak of the pattern is just about to split into two peaks; this might indicate that internal strains are just being developed during measurements, with evolution of peak splitting in the early stage where multi-peak patterns are starting to appear, and finally show gradual increase of peak-splitting in the data for longer X-ray exposure.

The plots of widths of split-peak as a function of X-ray illumination dose for three separate datasets from three different SOI nanowires are shown in Fig. 27. A similar trend is seen in all cases. The peak splitting effect is in both the XY plane of the detector and an offset in the Bragg angle theta. The combined splitting in units of Δq is plotted against exposure time in Fig. 27. This microscope was used to capture the confocal image in Fig. 28 immediately after the dosing series. Fig. 28 shows a height difference

between a dark band and the rest of the surface. The dark band has the shape and size of the X-ray beam footprint due to the angle of incidence of 1 degree. The focal depth of the confocal microscope was measured to be 100nm approximately. It can be recognised that the measured three-dimensional splitting increases approximately linearly with time of exposure of the X-ray beam on the single location on the chosen nanowire.

Simulation results are shown in Fig. 29 with detailed displacement fields of x and z-components with axes marked on Fig. 29 One-dimensional line plot in x-direction of the simulated model (in central line of the top Silicon layer) is illustrated in Fig. 30. The widths of peaks are also roughly proportional to the number of 2π phase-"wraps" in direct-space phase structures of simulated object, as seen in Fig. 31. Fig. 31 displays x-y view of scalar-cut-plane of simulated phases of our direct-space model for various maximum values of applied Gaussian stress function on the oxide layer.

The direct comparison of our measured and simulated diffraction patterns of radiation-induced bended SOI nanowire is shown in Fig. 32. Inspection of these and the data in Fig. 32 reveal a very close resemblance in both two-dimensional scalar-cut-planes and one-dimensional line plots, confirming the appropriateness of our model. The model parameters have been adjusted to get some quantitative understanding of the radiation-induced bending effect on SOI nanowires.

A block of Si illuminated by the focussed X-ray beam should give the diffraction pattern of a slit, i.e. a sinc function, in the two directions perpendicular to the wire; along the length of the wire the pattern is expected to be roughly Gaussian corresponding to the Fourier transform of the beam profile. In this model there would be a single central peak and no splitting. The peak splitting of the 3D diffraction data can only be related to the introduction of a significant strain in the sample that would cause phase shifts exceeding 2π (which is defined as phase-"wrap") between different parts of the illuminated part of the sample[1].

We have used Finite-Element-Analysis (FEA) analysis to simulate the radiation induced bending of our SOI nanowires measured in experiment. Our model introduces strain as a quadratic variation of phase along the sample[100]. This gives rise to a diffraction pattern that resembles a Fresnel integral[100]. Roughly speaking, the number of peaks in the resulting diffraction pattern corresponds to the number of "phase-wraps", i.e. the number of 2π repetitions within the illumination region of the nanowire. The linear splitting of the peak with dose would correspond to a linear increase in the quadratic phase or a linear increase of strain. Specific physical or chemical properties of SOI nanowires could contribute to various patterns of strain leading to this linear dependency.

The beam size used in the simulation agrees well with wire-scan estimates. The model we constructed assumes a similar sized beam for the cause of the damage (stress profile

shown in Fig. 31) as for the diffraction pattern. When one or other width was varied, the agreement of experiment and model was found to become worse. Our analysis shows that the best fit to the measured data in Fig. 32 has Gaussian stress function applied to the oxide layer and X-ray Gaussian probe with FWHM of 0.9 and 1.0 μm respectively.

The other parameter in the model that is very sensitive is the peak value of the applied Gaussian stress profile. This peak stress was varied systematically in Fig.33, which shows widths of the simulated peaks (defined in the same way as for the experimental data in Fig. 27, converted into reciprocal-space lattice units) as a function of maximum values of Gaussian function of stresses applied in the oxide layer. The behaviour is quite accurately linear, as expected from linear response theory, but confirmed through the FEA simulation.

FEA calculations were performed by using the COMSOL Multiphysics® package. A model structure was composed of a Silicon layer of 6μm (x) × 800nm (y) × 170nm (z) on top of a SiO_2 layer, all of which are sitting on bulk Silicon substrate. The SiO_2 layer is divided into two parts: one part designated for the application of isotropic stress with selected box-shaped region directly underneath the top Silicon layer of dimensions of 3μm (x) × 800nm (y) × 600nm (z), the other part with no initial stress applied in the simulation. Since we assume that the underlying mechanism of the peak-splitting effect is a consequence of pressure from the Silicon Dioxide that is closest to the patterned Silicon layer, we model a one-dimensional stress following the shape of the X-ray beam. A one-

dimensional isotropic Gaussian stress was programmed within this box as a function of x only. The simulated Gaussian stress has 0.9 μm FWHM and it is centred in the middle of the wire so that it is symmetric function with a maximum stress of 300MPa (N/m^2).

The output of the simulation is a displacement field within the model Si wire in physical units (m). This has to be converted into a real space phase in order to calculate the expected diffraction pattern. The conversion of $\vec{u}_{x,y,z}$ to a phase requires the experimental diffraction vector $\vec{Q}$, in this case the (111) reflection of Silicon corresponding to the 3.1350Å silicon (111) lattice spacing. The real space phases due to atomic displacements of Silicon (111) reflection can be calculated by the following formula:

$$\text{phases (radians)} = \text{Si(111)}.\vec{u}_{x,y,z} = \frac{\text{direct-space displacements (along } \vec{Q})}{\text{Silicon (111) lattice-spacing}} \times 2\pi \quad \textbf{Equation 44}$$

Where $\vec{Q}$ is the reciprocal-space lattice vector, and $\vec{u}_{x,y,z}$ are direct-space displacement fields in all three spatial directions, the dot product $\vec{Q}.\vec{u}_{x,y,z}$ gives evaluation of phases along direction of $\vec{Q}$.

For transformation to reciprocal space, the FEA object was sampled on a grid of 100, 30 and 12 pixels in x, y and z directions respectively. This object was zero padded into a larger array of 256, 128 and 128 pixels to avoid aliasing effects when the FFT was then calculated.

In order to simulate the diffraction patterns, the X-ray beam profile also has to be taken into account. The beam profile was assumed to be Gaussian amplitude (with zero phase) having a Full Width at Half Maximum (FWHM) of 16 pixels in x direction. The total number of pixels incorporated into our simulations in the x direction was 100. This width was chosen to be the same as the width of the stress profile used to generate the pattern of distortions in FEA. This profile was used as the amplitude of the object whose phase is given by Eqn. 44.

The diffraction pattern $\mathrm{A(q)}$ of an electron density distribution $\rho(x)$ is connected by the analytic continuous Fourier Transform (FT). This is expressed with the following formula:

$$A(q) = \int_{-\infty}^{\infty} \rho(x) \mathrm{e}^{\mathrm{i}qx} \, \mathrm{d}x \quad \textbf{Equation 45}$$

To convert this to numerical Discrete Fourier Transform (DFT), the continuous functions need to be written as arrays of complex numbers. Theoretical oversampling ratios of 2.56, 4.3 and 10.7 were introduced for x, y and z direct-space directions respectively. The

sampled quantities are array of complex numbers: A_j and ρ_k , where the real and reciprocal space variables have become discrete $x = \Delta x.k$, $q = \Delta q.\, j$.

$$A_j = A(\Delta q.j) \quad \textbf{Equation 46}$$

$$\rho_k = \rho(\Delta x.k) \quad \textbf{Equation 47}$$

The DFT connection between arrays is:

$$A_j = \sum_{k=0}^{N-1} \rho_k \, e^{2\pi i jk/N} \quad \textbf{Equation 48}$$

The exponents in the expressions for the FT and DFT have to be the same, which means:

$$\frac{2\pi}{N} = \Delta q.\Delta x \quad \textbf{Equation 49}$$

We note that the physical quantities Δq and Δx have units of m and m^{-1} respectively. N is the dimension of the arrays. Array sizes used in simulations are of N=256, 128 and 128 pixels in x, y and z dimensions respectively.

7:1:4 Discussion

We can compare of the simulated diffraction response in Fig. 33 with the experimental observation as a function of X-ray dose in Fig. 26. Both curves are linear, although different samples have slightly different slopes. Equating the slopes of Fig. 27 and 33 allows us to calibrate the rate of generation of stress by X-ray irradiation of SiO_2. The peak width reaches $0.04nm^{-1}$ after 100mins or 200mins depending on the sample. This corresponds to a peak stress of 185MPa according to the simulation in Fig. 32. The coherent flux of the beamline is not well-calibrated, but is roughly 10^9 photons/sec integrated over the focal spot with an area of $(1.5\mu m)^2$. A 100 min exposure would cause 6×10^{12} photons to be absorbed, depositing an energy of 0.009 J within a volume of 1.5μm×1.5μm×180μm (penetration depth of SiO_2 at 8.9keV), with a mass of 0.9×10^{-12}kg, amounting to a dose of 1×10^{10}Gy (J/kg). Dividing these quantities indicates a stress of 0.0185 Pa/Gy of dose for the first sample, 0.037 and 0.0925 Pa/Gy of dose for the second and third samples respectively.

One can deduce that the underlying mechanism of this peak-splitting effect must be due to the X-ray dose, due to the fact the measurements were performed at exactly the same position on the chosen nanowire with the same experimental parameters for data acquisition. The peak-splitting effect originates from of the accumulated X-ray exposure or received dose.

The reciprocal-space unit lattice-vectors for all directions of experimental measurements are evaluated by the following expressions:

$$\Delta q_{\chi,y} = \frac{\Delta p_{\Delta x,\Delta y} \times P}{D} \times \frac{2\pi}{\lambda} \ (nm^{-1}) \quad \textbf{Equation 50}$$

$$\Delta q_{\theta} = q \times \Delta\theta = \frac{2\pi}{d_{(111)}} \times \Delta\theta \ (nm^{-1}) \quad \textbf{Equation 51}$$

Where $\Delta p_{\Delta x,\Delta y}$ are the reciprocal-space unit vector in $X_{detector}$ and $Y_{detector}$ dimensions, P is widths of peak envelope distribution in pixels on the detector, Δq_{θ} is the reciprocal-space unit vector in θ (rocking) direction, $d_{(111)}$ is the lattice-spacing of Silicon (111) direction, D is sample to detector distance and λ is the wavelength of incoming X-ray.

The 34-ID-C beamline at Argonne has an integral confocal optical microscope used for 3D alignment of the sample in the beam[101]. In Fig. 28 the image contrast indicates that the height difference of radiation-damaged regions of Silicon and oxide and the non-or little damaged ones is of the order of around 10nm. One can see that the burn is clearly extending over the oxide region, rather than the nanowire itself, which appears intact. So we can hypothesize the distortion comes from radiation damage to the Silicon Dioxide.

7:1:5 Conclusion of Experiment

Our results suggest that the observed bending behaviour of SOI nanowires originates from a time-dependent thickening of the Silicon dioxide layer below the patterned Silicon nanostructures during the X-ray irradiation. The rate of thickening of the bottom part of Silicon nanowire layer is proportional to the time of exposure of X-ray, in other words, the accumulated dose. To confirm our radiation induced bending effect model, measurements of three-dimensional rocking curves of different nanowires were performed in a Helium gas-filled chamber. Much less radiation-bending effects were observed with little peak-splitting after 2-hour of exposure, corresponding to the same dose per unit area on the sample.

This observed important peak-splitting behaviour might be related to a specific SOI wafer bonding technique, which can be different from other methods. There have been no observed radiation-induced bending effects in some other measurements of SOI structures[45,102]. Radiation effects in SOI have been reported by the authors of ref [103], who observed structural change due to radiation damage on SOI nano-structures with an oxide layer underneath. However, radiation damage was not observed with SiGe thin-film structures on Silicon substrate only with no oxide layer in between, therefore the report suggests that the causes of radiation damage on Silicon or SiGe structures originated from the oxide layer or the interface between the Silicon and oxide layers [103]. This

conclusion is consistent with what we have observed in our measurements. We envisage CDI can be the next step for direct imaging of structural modification by X-rays radiation damage, lattice distortions induced by structural damage induced by X-ray irradiation can be in principle in the scope of current available Bragg CDI spatial and strain resolution, which are about 30nm and 0.1nm respectively at beamline 34-ID-C at APS. Future developments of coherent X-ray beamlines in 4rd and 4th generation synchrotron worldwide can improve both resolutions and mapping of both isolated and extended 3D crystalline samples under radiation damage of high energy X-rays can be a useful routine technique.

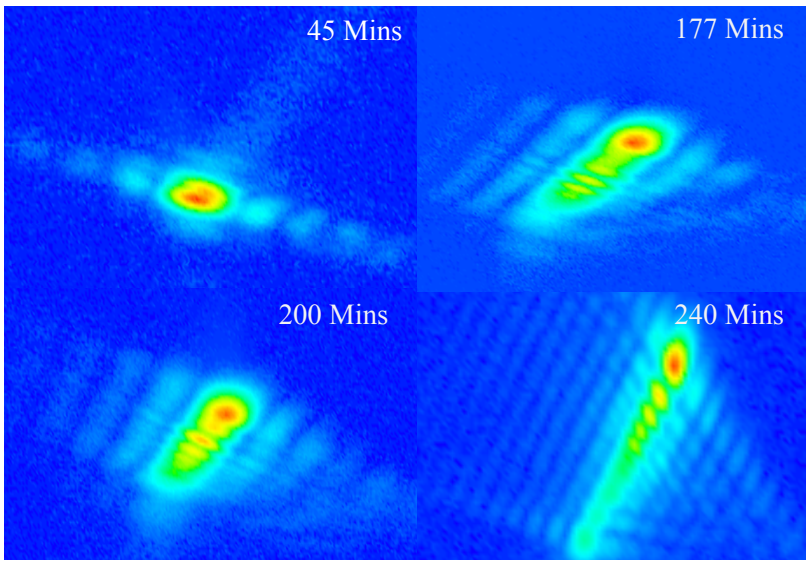

Figure 26 Central slice of intensity of the measured three-dimensional diffraction patterns, showing the evolution of diffraction peak splitting with increasing X-ray doses. Each image shows the same two-dimensional scalar-cut-plane through the full three dimensional diffraction pattern. All of the images are measurements on the same region of a single SOI nanowire. The X-ray probe illumination dimensions of 1.5μm X 800nm X 170nm for length, width and thickness respectively.

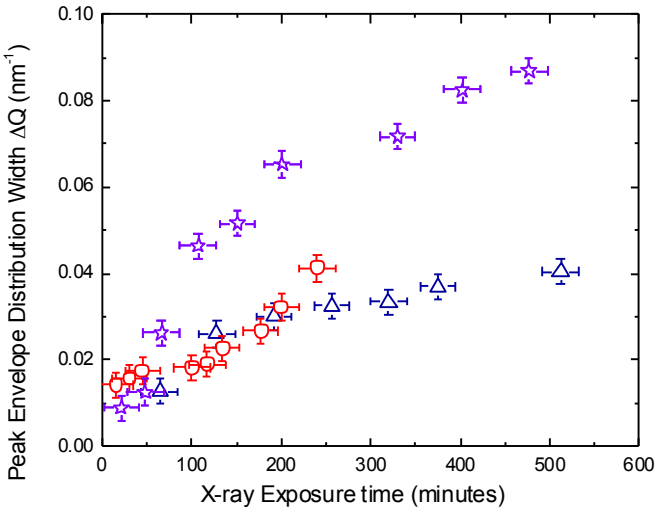

Figure 27 Widths of split-peak distributions (in reciprocal lattice units) as a function of X-ray dose of the measured diffraction patterns. The behaviour is roughly linear for all three different datasets. The blue, red and purple datasets groups were measurements taken for different SOI nanowires with the same spatial dimensions of X-ray probe illumination.

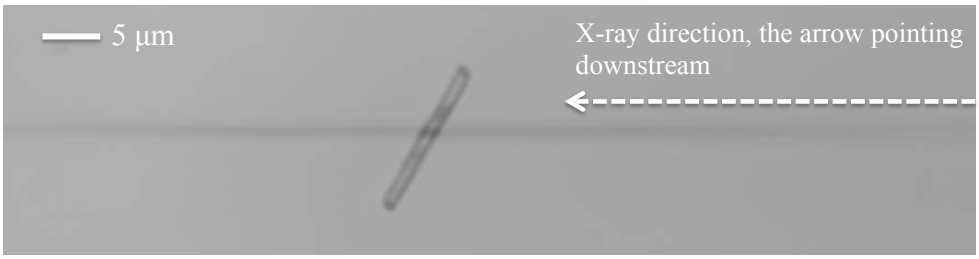

Figure 28 Confocal microscope image of one of the SOI nanowires after dosing with X-rays for about 2 hours. The X-ray beam is inclined at a 1-degree incidence angle, running right to left. The surface of SOI nanowire also appears to have become raised by the beam exposure. The darker colour represents higher level of the SiO_2 surface under the beam illumination footprint. This image was captured with Olympus LEXT instrument with a laser wavelength of 408nm.

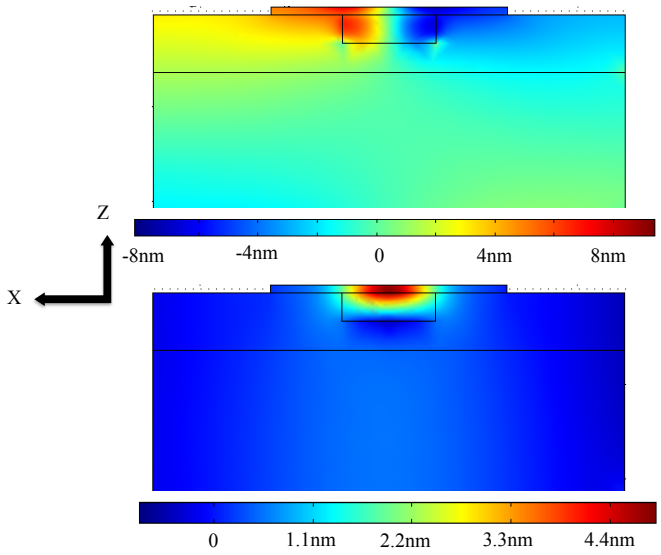

Figure 29 Finite Element Analysis (FEA) calculation result showing x displacements (top) and z displacements (bottom) of a Silicon wire structure modelled on a SiO_2 substrate block and Silicon substrate. An isotropic Gaussian stress of 0.9µm FWHM length, centred in the middle of the SiO_2 block as a symmetric function, has been applied in the box-shaped region below the wire. The maximum stress is $3x10^8$ Pa (N/m^2).

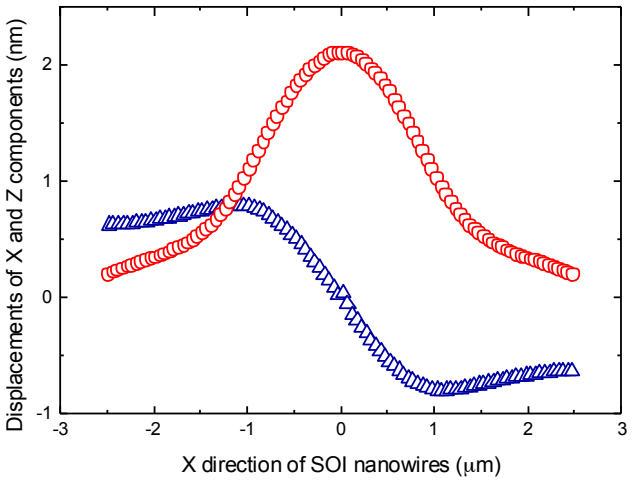

Figure 30 Line plots of the x (blue triangles) and z (red circles) components of displacements from the FEA calculation in Fig 19, extracted from the surface of the central slice of the SOI model system.

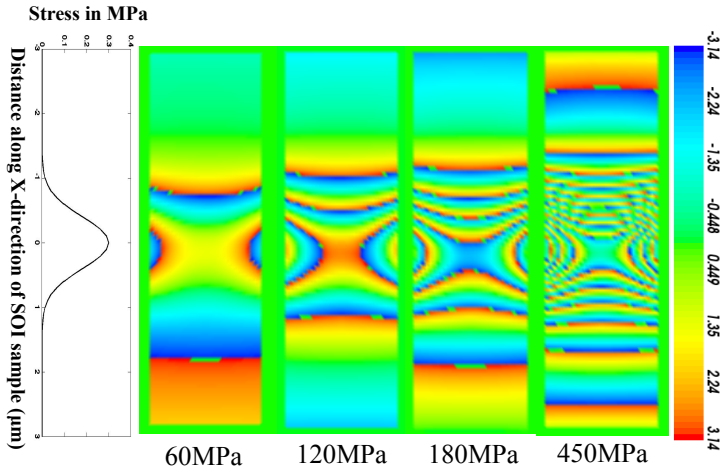

Figure 31 Simulated direct-space phase images of the FEA -calculated displacement fields, as viewed from the top of the Si nanowire (x-y plane). The labels give maximum values of the one-dimensional Gaussian applied stress functions, shown schematically on the left.

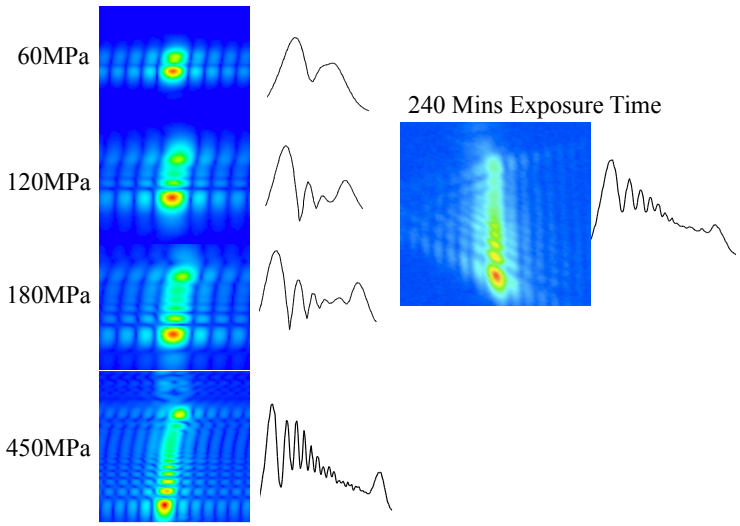

Figure 32 Comparisons of simulated (left) and measured (right) diffraction patterns shown as 2D scalar-cut-plane and line plots.

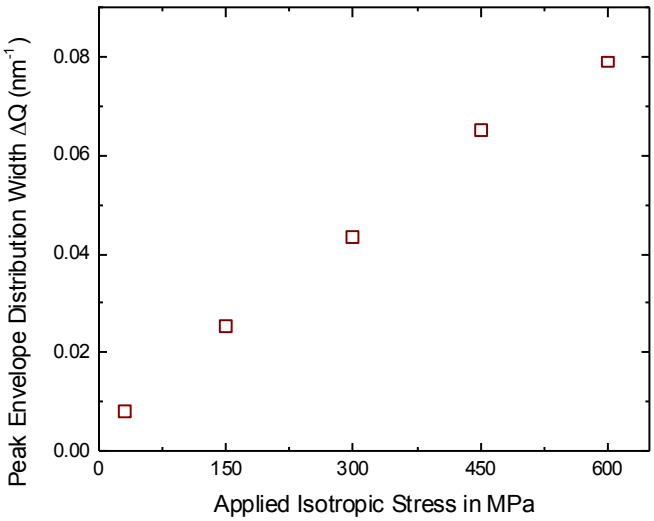

Figure 33 Calculated widths of split-peak distributions (in reciprocal lattice units) of simulated diffraction patterns as a function of values of isotropic stress applied on the Silicon Dioxide layer.

It is clear that X-rays radiation causes Silicon nanowires to bend by thickening of Silicon Dioxide layer underneath. This induces splitting of peaks of diffraction patterns measured in Fourier-space. Those highly strained diffraction intensities can be reconstructed in principle, however, further developments of CDI algorithms have to be performed to enable successful reconstructions of those diffraction patterns. We propose highly strained complex Silicon models can be used to guide CDI reconstructions, imposing extra constraints in direct-space part of the algorithms.

7:2 Mechanical breakdown of bent Silicon nanowires imaged by Coherent X-ray diffraction

7:2:1 Introduction of Experiment

An advantage of BCDI[4,113] over other methods for investigating strain[1] is due to its enormous potential for probing large three-dimensional buried structures without the needs of slicing three dimensional (3D) objects. BCDI allows us to investigate strain on the nanoscale within objects in their as-prepared state. No destructive thinning or other sample preparation is required. BCDI is able to investigate strains, seen as displacements from the atomic positions of an ideal crystal lattice. It allows measurements of strains of individual structures (with dimensions from 10nm to >1μm) while other diffraction techniques obtain results by averaging many copies of the structure of interest[9].

Typically CDI makes use of iterative algorithms such as hybrid-input-output (HIO)[51] and error reduction (ER)[31] to solve the phase problem, using the property that the diffraction pattern is oversampled with respect to the spatial Nyquist frequency. Once phased, the diffraction patterns are transformed to 3D real-space images. However, these iterative algorithms often fail when phasing the diffraction patterns of highly strained objects, with the algorithms failing to converge. Retrieving images from CDI data measured from objects containing large strains is still under development, though there have been several successful attempts[9,45]. Our GPER method uses calculated complex real-space models to

guide iterative algorithms, leading to much better convergence. One reason strong-phase CDI is so difficult is the "propagation uniqueness", whereby equivalent solutions can be generated by propagating along the optical axis, all of which possess the same far-field diffraction patterns[42,45]. Because strain patterns in the sample and X-ray focusing artifacts can have similar phase distributions to an out of focus image, highly strained samples present a uniqueness problem to the phase retrieval algorithms which normally work in the case of lightly strained samples.

Following our last New Journal of Physics paper on radiation induced bending of Silicon nanowires, successful CDI reconstructions of measured highly-strained data have been performed with our phase-guided method. Furthermore, we have observed radiation induced dislocation loop and possible insertion or deletion of atomic planes with Silicon nanowires. This opens up an interesting and promising potential for imaging defects in crystalline structures by using CDI.

Materials undergo elastic deformation whereby the applied external stress and the resulting strain follow a linear relationship, as can be nicely illustrated in stress-strain diagrams. However, when the applied external stresses exceed the elastic limit of the material, the linear stress-strain relations does not hold anymore. The elastic limit for single crystalline Silicon is difficult to measure experimentally, and there is currently no consensus on the exact value. One of the difficulties for accurate measurement in semiconductor or metallic materials is that the complex microstructure couples with the

anisotropy of elastic modulus, so the elastic limit for specimens of different microstructures of the same material can be different[104].

Studies show that the breaking stress of Silicon is measured to be around 1GPa, with some variation depending on different sample preparation procedures[105]. Experimental measurements have shown that the fracture stresses of Silicon wafer with thicknesses of several hundred microns are around several GPa[106], with maximum experimentally determined values of 175 MPa[107]. Other studies have shown experimentally that breaking/fracture of single crystalline Silicon occurs for fracture stresses between 40 to 110 MPa for various indent loads and flaw sizes[108]. Microstructuring of brittle materials such as Si leads to higher values of fracture stress than bulk because the crack/flaw size in microstructures is much smaller, according to Griffith's criterion[109]. Dislocation banding with up to 20% plastic deformation in float-zone Silicon microstructures has been obtained at room temperature from applied stresses of 5 GPa[110]. Studies show that superimposing a confining pressure of around 1.5 GPa on single crystal Silicon produces large plastic strains at 300°C with up to about 1GPa of yield stress[111].

7:2:2 Method of Experiment

Here we study the appearance of dislocations in bulk Silicon by Bragg Coherent X-ray diffraction imaging (BCDI), which is a sensitive method to probe these defect structures[112]. We have imaged dislocations in Silicon nanowires, fabricated using Silicon-on-Insulator technology, during bending by radiation-induced swelling of an adjacent

oxide layer. We introduce a method for phasing the diffraction patterns, Guided-Phase-Error-Reduction (GPER), which makes use of quantitative Finite Element Analysis (FEA) calculations to constrain the phasing. We have observed mixed types of dislocations in the reconstructed nanowire following the highest dose of X-rays. An abrupt change immediately beyond this dose indicates that the nanowires undergo mechanical breakdown upon further X-ray exposure.

The SOI patterned structures used in our studies consisted of 170nm thick Si thin films on top, a 1μm thick SiO_2 layer in the middle and bulk Silicon substrate at the bottom. PMMA resist was used for Electron-beam lithography for patterning of our SOI structures with a lateral dimension of 800nm and a length of 15 μm. Reactive ion etching (RIE) with SF_6 at a flow rate of 30 sccm and DC voltage of 100V was used to etch away the unwanted top layer. Arrays of Si nanowire structures were fabricated with overall dimensions of 15μm x 800nm x 170 nm (length x width x height). A slight undercutting of the resist was obvious in the obtained structures due to the RIE process.

CDI measurements were performed at beamline 34-ID-C of the Advanced Photon Source at Argonne National Laboratory, with an X-ray energy of 8.9 keV selected with a Si (111) monochromator. The X-ray beam was cut to dimensions 30μm and 50μm using slits to preserve the X-ray coherence properties[22]. The coherent beam was then focussed with horizontal and vertical Kirkpatrick-Baez (KB) mirrors. The size of the focus was measured to be slightly less than 1.5μm in both directions using crossed Tungsten wires.

A confocal microscope[24] was used to pinpoint the specific nanowire structures to be measured. Off-specular (111) reflections of Si nanowires were chosen for CDI measurements and the incidence angle was fixed to be 1 degree. The far-field diffraction intensity was measured by a charged coupled device detector with 20 μm pixels, placed 0.7 m away from the sample, orientated at the corresponding (111) Bragg angle. Rocking curves with a range of ±0.5 degree in the rocking angle with 0.02 degree increments were taken, so that the oversampling conditions were fulfilled in all three dimensions. We previously showed[114] that the underlying SiO_2 layer swells gradually after prolonged exposure to such a strongly focused X-ray beam and this causes a local bending of the nanowire over the width of the beam(about 1um) in the middle of its length. A series of 20 measurements were made at intervals of 15 minutes to observe the evolution of the diffraction pattern. Cross sectional slices through these 3D diffraction patterns are shown in Fig. 32 at representative times during the evolution. Fig. 32(d) was the last recorded diffraction pattern before it disappeared. After 240 mins of exposure, the measurement time was increased by a factor of 4 to achieve the same total integrated intensity as earlier measurements of the same nanowire. These measurements record the evolution of Silicon nanowire as it is bent by the swelling of the underlying oxide under irradiation.

7:2:3 Results of Experiment

We have showed previously[114] that the redistribution of intensity in the Bragg peak, and notably the progressive splitting of its center into two distinct side lobes during the time series, could be explained by bending of the SOI wire under radiation-induced stress

from the SiO_2. This was achieved by Finite Element Analysis (FEA) using the COMSOL program. In this work we use that FEA model as a constraint in the GPER data fitting procedure. It was necessary to carry out FEA calculations in the same coordinate system as the measurements, so the simulated nanowires were rotated to the crystallographic orientation that was used in the experiment. A Gaussian X-ray probe with full width at half maximum of 1.5 μm, was then used to simulate the diffraction pattern. Both simulated and measured data for various X-ray exposure doses are presented on the same sampling grid in Fig. 34.

Traditional phasing algorithms utilize a direct-space constraint in the form of a "support", a volume of space in which the solution is allowed to exist. The GPER algorithm generalizes this idea to a 3D complex "support", using the model as an additional direct-space constraint on phases. If the phase values at each voxel of the current iteration lie outside an allowed range from the model they are set to those extreme values, otherwise the phase values are kept unchanged. Typical bounds were $\pm 0.5\pi$ to $\pm 0.9\pi$ depending on the datasets. This extra step is followed by the standard support constraint projection of the ER algorithm, whereby all density points outside the object boundary are set to zero. Various structures of complex "support" models were tested to guide reconstructions; only those close to real structures give good convergence. Once close ranges of models were selected, fixed models were used to guide data inversion with the GPER algorithm.

7:2:4 Discussion

Previous analyses by Huang[45] and Minkevich[9] have demonstrated the power of various direct-space constraints which have led to an improvement in convergence and better filling of the density of reconstructions from CDI data of highly strained objects. Huang et al discovered that implementation of phase-constraint in direct-space is equivalent to the usage of a tight-support constraint and that application of both led to correctly focused solutions[45]. Newton utilized a direct-space density gradient minimization method that is related to compressed sensing techniques[46]. In order to reconstruct highly strained CDI data, it is necessary to use a priori information about the sample[9]; Our method shares similarities with Fresnel CDI (FCDI) which utilizes a known curved illumination [5,8] to avoid the twin confusion problem that is common in phase retrieval. Our method also bears strong similarity to phase retrieval in surface x-ray diffraction where a model of the bulk crystal is used as a reference in phase retrieval to produce an image of the surface structure[115].

The model phase structures of SOI nanowire with various irradiation doses are illustrated in the top panel of Fig. 35. The phases were calculated by taking the scalar product of the displacement with the reciprocal-space Q-vector for the (111) crystallographic planes of the Silicon nanowire. The phases shown in the top panel in Fig. 35 represent projected displacements resulting from strains induced from bending of SOI nanowire, with applied stresses on the SiO_2 underneath the Si nanowire having the

maximum values indicated. The diffraction patterns in Fig. 34 are the Fourier transforms of these model structures.

Fig. 35 middle and bottom panels show amplitudes and phases (scalar-cut-plane) of the final GPER reconstructions of the SOI nanowire with increasing X-ray radiation doses, from 45 mins to 240 mins exposure time respectively. The density is filled in reliably over the body of the nanowire, with some residual modulations associated with its strong phase structure. The two ends of the nanowire reconstructions are rough because the confined X-ray illumination between the ends of the nanowire, as observed previously[116]. The RIE processing step might have resulted in some roughness features on the surface.

We find that solutions are relatively stable after 30 iterations of GPER, the error-metric χ-square is relatively low, and calculated diffraction patterns have around 3 percent deviation from measured data. Reconstructions performed starting with up to 25% values of applied Gaussian stresses of in the FEA models all produce the main features, both phases and amplitudes, though some small derivations of phase features are present. The supports used for the reconstruction were determined from the 3D autocorrelation of the data.

To view the distortions associated with the last state of bending before fracture, we show an image of the difference between the phase of the FEA model and the reconstructed

data for the 240 mins x-ray dose in Fig. 36. Three characteristic phase structures have appeared, each with a distinct phase wrap (-π to π) following an undulating plane traversing a localized region of the nanowire. Fig. 36 (b, c, d) shows these features are present throughout the thickness direction of the SOI nanowire, measured to be 160nm, and extend over 200nm laterally. It is a clear indication of the insertion or deletion of a single plane. This phase is a projection of the lattice distortions onto the (111) Q-vector, which points along the (110) long-axis of the wire, and inclined slightly above the plane. Such a phase wrap is a clear indication of the insertion of a single plane of atoms and the relaxation of the strain field surrounding it. So we identify these features as dislocation loops, viewed edge on, as indicated schematically in Fig. 36(e).

The two structures on the lower side of the wire are roughly planar, while the one on the upper side in Fig. 36 appears doubled, possibly by the merging of two nearby loops. It is important to note that only the component of lattice distortion along the (111) direction is resolved, so some parts of the structure may be concealed. There is also some noise in the images from the phase subtraction procedure, but the presence phase wraps is very clear. Some of the jagged appearance could be due to relative movement of the beam and sample[117] or from fluctuations during the exposure. It is probably significant that all three dislocation loops have formed away from the central region of highest beam intensity, very roughly at its half-maximum point, and that the phase wraps have opposite sign on the two sides. According to the model above of radiation induced swelling of the

underlying oxide, these will be the points of maximum stress gradient with a significant shear component.

A previous Coherent X-ray diffraction study of dislocations in bulk Silicon showed a localized streaking of the Bragg peak whenever the scanned X-ray beam crossed over a dislocation loop[112]. The interpretation of the streaking was due to an extended planar structure trapped between two partial dislocations forming the loop, extending over several hundreds of nanometers. The authors of Ref [112] have not presented any images of the structures obtained by inverting their diffraction patterns; direct comparison with our diffraction patterns is not possible because of the dominant contribution of bending in our data.

The close agreement of the FEA model with the experimental data means we can trust the input parameters quite well. The peak stress within the radiation-sensitive SiO_2 layer was 450MPa for the case when the dislocation structures started appearing. This marks the beginning of plastic deformation and gives an estimate of the elastic limit of Si in this geometry. The COMSOL analysis allows us full access to the elastic stress-tensor components three-dimensionally in the whole nanowire structure. Directly reading from our FEA model, the stress within the Si wire is highly anisotropic. The maximum stresses of the diagonal tensor components near the edges of Silicon nanowires were 330 MPa; the maximum shear stresses were around 176 MPa. This number for the elastic limit of Si is comparable with experimental values for fracture stresses[107,108]. It is possible that there

may be some radiation-induced weakening of the Si, and also that there are unresolved artifacts of the RIE procedure used to make the nanowires giving rise to weak points in the structure.

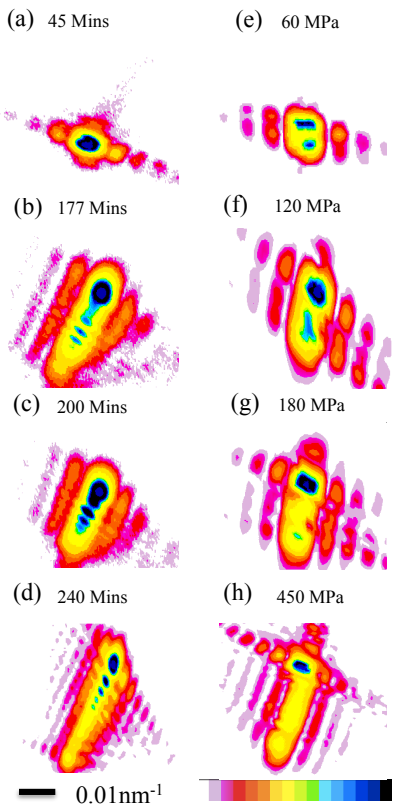

Figure 34 (a)-(d) are experimental diffraction patterns of a Si nanowire as a function of exposure time and (e)-(h) are corresponding simulated patterns as a function of peak applied stress.

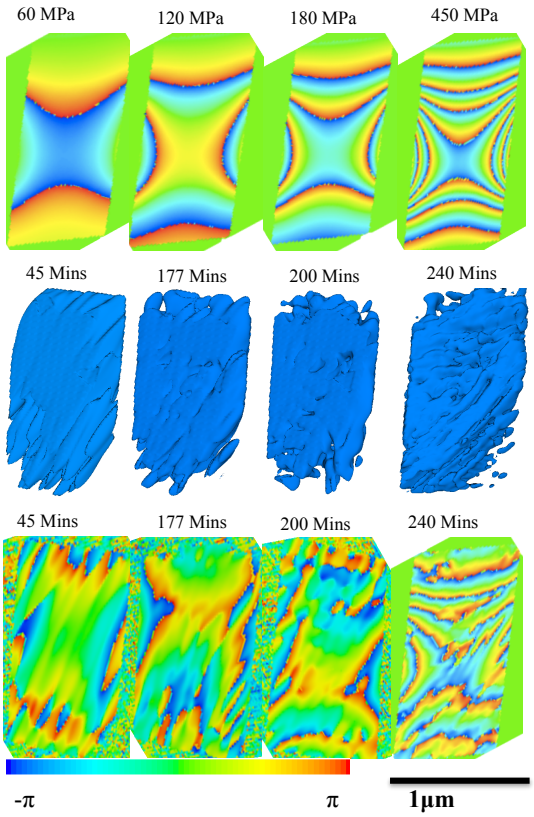

Figure 35 Top panel: cross sectional view of the direct-space phase structures simulated in a nanowire by COMSOL FEA. Middle panel: iso-surface (with contour-level of around 15% of maximum) of reconstructed amplitudes. Bottom panel: cross section of the reconstructed phases near the middle of the nanowire.

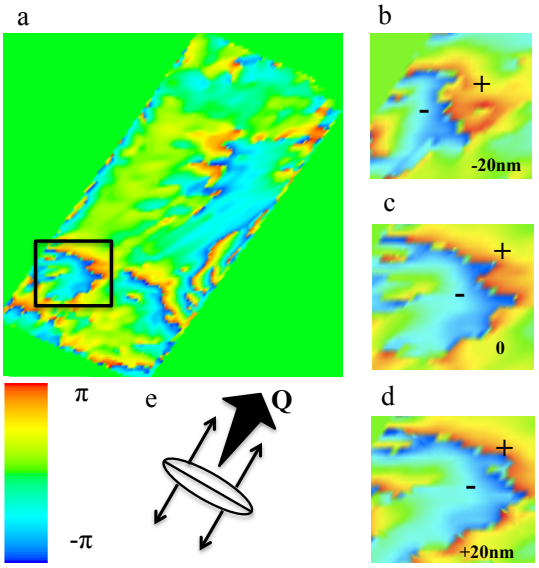

Figure 36 (a) image of the difference between the phase of the FEA model and the reconstructed data for the 240 mins x-ray dose; (b-d) at the center and slices 20nm above and below, (e) shows phase projection of the lattice distortions onto the (111) Q-vector, which points along the (110) long-axis of the wire, and inclined slightly above the plane as indicated by the black tapered arrow.

To test highly strained Silicon nanowire data convergence, a number of reconstructions starting with different initial phase-models were performed; similar reconstructed amplitudes and phases are expected if data are fully converged.

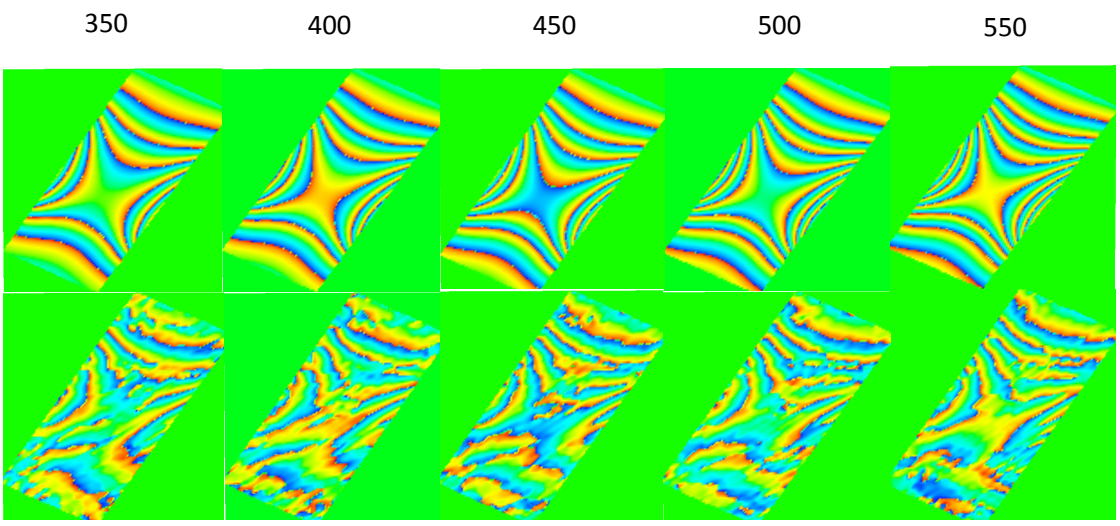

Figure 34 Convergence test for different initial phase-model starts. Top Panel: Simulated phase, Bottom Panel: Reconstructed phase

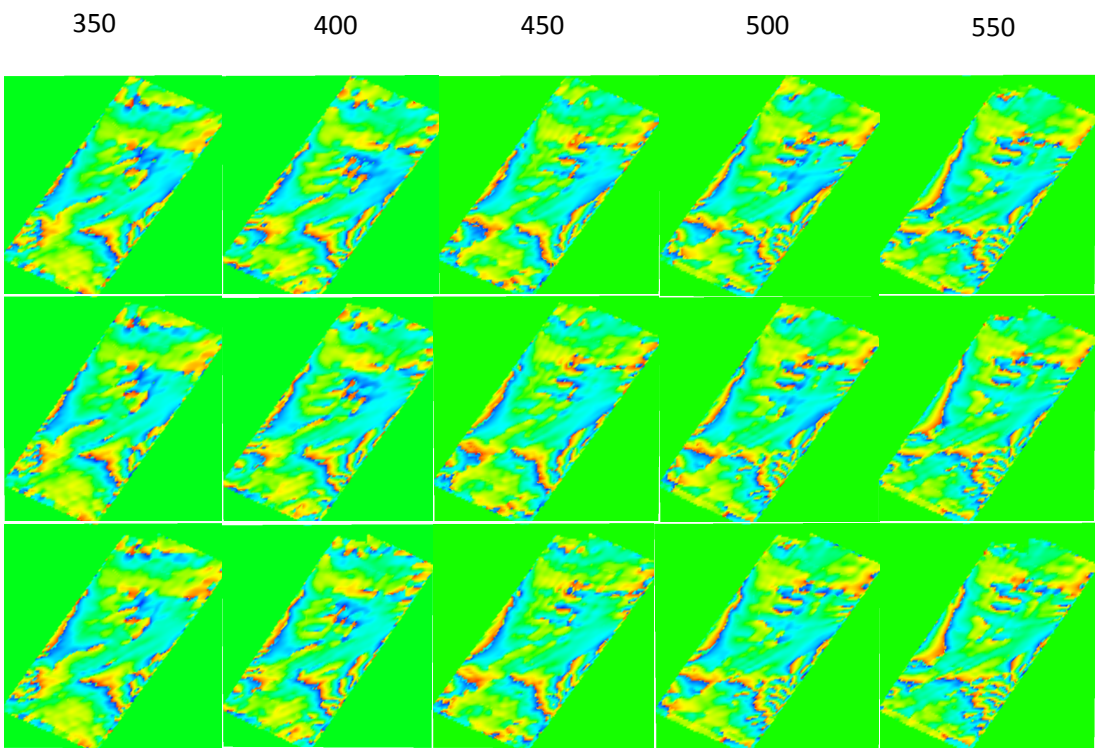

Figure 35 Test for reproducibility of defects of Silicon nanowire due to radiation-induced bending under high dose of X-ray irradiation

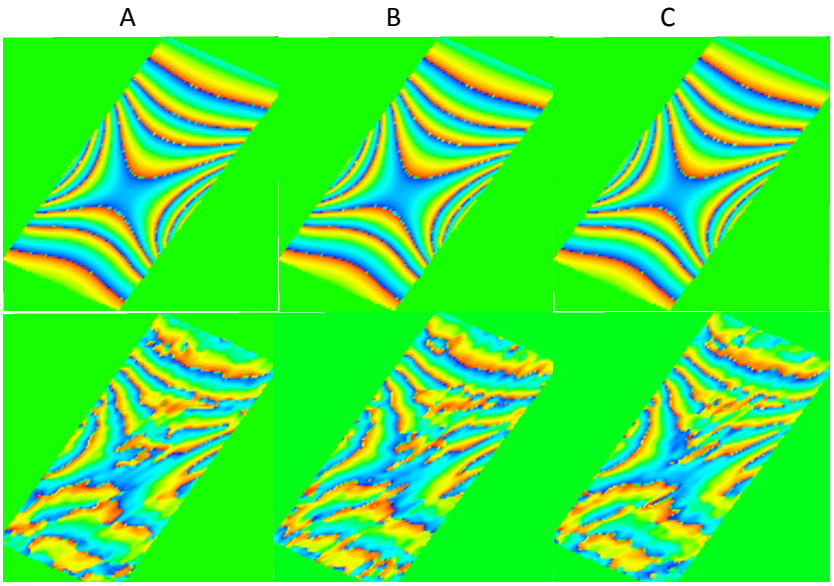

Figure 36 Panel A: Starting amplitude uniform inside the support and zero outside the support; Panel B: Random amplitude inside the support and zero outside the support; Panel C: Another Random amplitude inside the support and zero outside the support. All three reconstructions are phase-guided with phase-model of maximum stress of 450 MPa of initial Gaussian stress.

For the important question of the convergence of the images used in our studies, we have performed two tests and include the results here. In the manuscript, we have added the following sentences about the convergence, Our GPER method gives stable, reproducible results for some range of starting phase structures. For the critical highest strain case, a range of maximum stresses from 350 to 550MPa yields almost identical results, for example. It also converges to the same solution from different initializations of the algorithm with random numbers.

We have varied initial phase structure by applying maximum Gaussian stress at Silicon Dioxide layer underneath Si nanowire with 350, 400, 450, 500 and 550 MPa respectively to test convergence. As the figure illustrates, all of the reconstructed phases have similar

main features, with very little variations of small features. The defect features are also reproducible when changing initial phase structures, and with different initial random amplitude starts. Our analysis shows that our reconstructions converge with relatively high degree of reliabilities. Fig. 37-39 show detailed results of our data convergence test.

7:2:5 Conclusion

Imaging of three-dimensional dislocations by High-Resolution Transmission Electron Microscopy[118] represents an important step towards the understanding of imperfection of semiconductor nanostructures. Previous studies on stacking faults/dislocations on metals suggest[119] that the deformation mechanism of metals is dependent on ratio of stacking fault energy to unstable stacking fault energy. The studies also suggest that quantitative mapping of three-dimensional the deformation mechanism of metals or other materials in general purely by simulations is still at its infancy, because the current simulation methods could only allow investigations on scenarios of high stress with short time-scale[119]. Further experimental evidences have to be obtained along with theory to enable complete understanding of plastic deformation of metals and other materials.

CDI using Bragg peaks from crystalline samples is extremely strain-sensitive which can be used to study highly strained objects. Various dislocation structures in Silicon occur when the applied external stress is close to the elastic limit, i.e. when Silicon begins to

break. Dislocations, which can be edge, screw or mixture of the two types, are found to be present in plastically deformed Silicon of various types[120,121]. Our observed dislocations within SOI under high X-ray doses further demonstrate that BCDI is a good technique for analysing dislocation/defects within nanostructures in a quantitative way. Similar strains and deformations of epitaxial SiGe have been observed in SOI micro-pad structures due to industrial processing [122].

Our studies have demonstrated the novelty of BCDI for successful probing the evolution of nano-scale strains in nanostructured Silicon with increasing X-ray radiation doses. The transformation of SOI nanowire structures can have a crucial influence on nano-mechanics under various device-operating conditions, such as radiation, heat and pressure. Our work provides an improved understanding of dislocation-forming processes in semiconductors in general, and this technique could be promising for pinpointing underlying mechanisms that are responsible for observed improvements on carrier mobility in SOI-based electronic devices[123].

The causes of bending of Silicon nanowire is mainly due to the swelling of Silicon Dioxide layer underneath of Silicon nanowire upon intense X-ray irradiation. The effect of oxide swelling under radiation has been well-understood[124] for a long time, however, what we are reporting is the localised effect this has on the strain in a nano-sized electronic structure, which is new.

The bending of Silicon nanowire can also be induced by oxidation of itself upon intense X-ray irradiation over a long period of time. The rate of oxidation of Silicon nanowire could be increased by irradiation of X-rays causing damage on the illuminated spot on the nanowire.

7:3 Simulations on highly strained twinned micro-crystals

Simulations of twinned micro-crystals with single, double or multiple phase-wraps are useful for understanding and analysing the origin of split-peaks in measured CDI diffraction patterns. Phase-wraps in both directions, i.e. both positive and negative phase gradients when reaching $+\pi/-\pi$ boundary are simulated so that comparisons of corresponding diffraction patterns can be done. Recent report shows extremely complex multi-peaks CDI measurements performed in Diamond I-16[125]; developments of effective iterative algorithms have been undergoing to understand and to successfully reconstruct such complicated diffraction patterns aiming at better understanding of structures; physical and chemical properties domains of twinned micro-crystals. The twinned crystal case is very difficult to solve mainly due to fact that the extra contribution from mis-orientation of crystals produce extra large phase ramps in the direct-space object. This results in further asymmetry of the diffraction intensities, and the highly strained diffraction feature might overlap with the strains due to atomic displacement projection in one single crystal orientation. This in turn results in the diffraction intensities with superposition of various phase origins. Figs 37-40 illustrate various simulations studies on highly strained twinned crystals. The resulting diffraction intensities are rather complicated with two or even multiple peaks overlapping in the patterns, posing substantial difficulty to any CDI data inversion procedure.

Fig. 40-43 illustrate various simulations studies on highly-strained twinned crystals, the resulting diffraction intensities are rather complicated with two or even multiple peaks in the patterns, posing various difficulties in CDI data inversions.

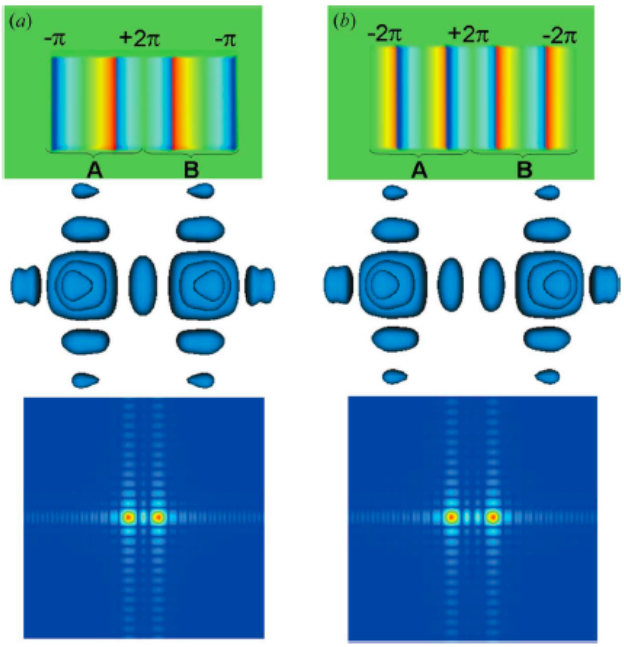

Figure 37 (Top) Two bicrystals shown as a translucent three-dimensional box withcolours representing the phase change. The two twins (A and B) have the same dimension (24 _ 24 _ 24 grid points) but different slopes of the phase ramps: (a) 1.5_, (b) 2_. (Middle) Calculated three-dimensionalcoherent diffraction patterns of the two twinned objects. (Bottom) Isoscalar plane cut of the diffraction patterns[125].

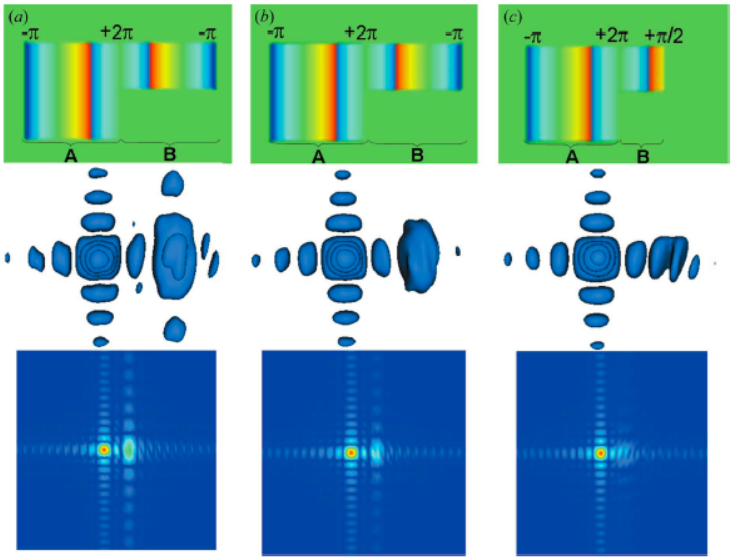

Figure 38 (Top) Three bicrystals shown as a translucent three-dimensional box with colours representing the phase change. The two twins within each bicrystal have different dimensions: (a) (24 _ 24 _ 24) and (24 _ 12 _ 24), (b) (24 _ 24 _ 24) and (24 _ 12 _ 12) and (c) (24 _ 24 _ 24) and (12 _ 12 _ 12) grid points. (Middle) Calculated three-dimensional coherent diffraction patterns of the two twinned objects. (Bottom) Isoscalar plane cut of diffraction patterns[125].

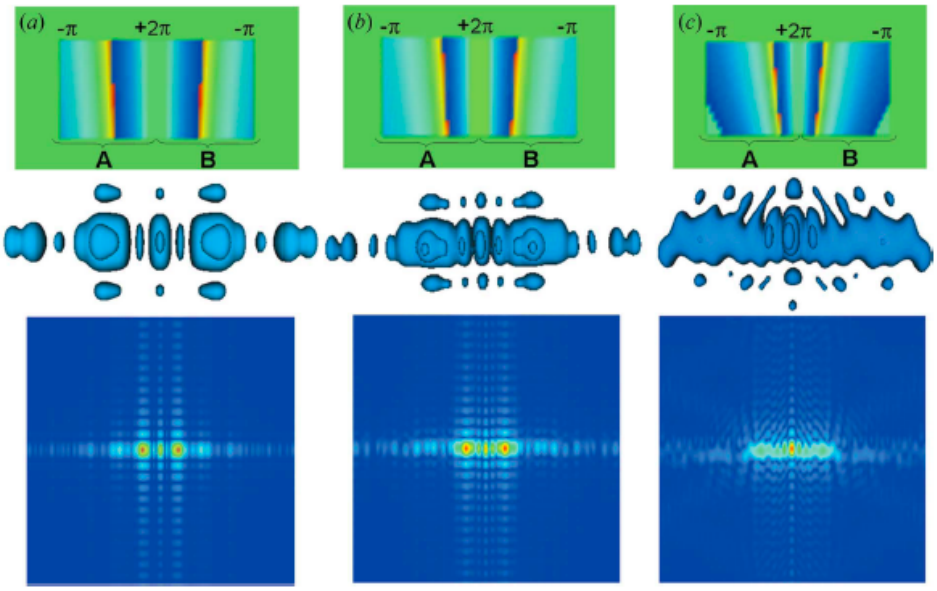

Figure 39 (Top) Three bicrystals shown as a translucent three-dimensional box with colours representing the phase change. The two twins have the same dimension (24 _ 24 _ 24 grid points) and the same overall variation of the phase ramp. However, the curvature of the parabolic function changes in the three objects. The change has been modelled by displacing the minimum of the parabolic function by 78 (a), 35 (b) and 15 (c) pixels from the object. (Middle) Calculated three-dimensional coherent diffraction patterns of the twinned objects. (Bottom) Selected isoscalar plane cut for the diffraction patterns[125].

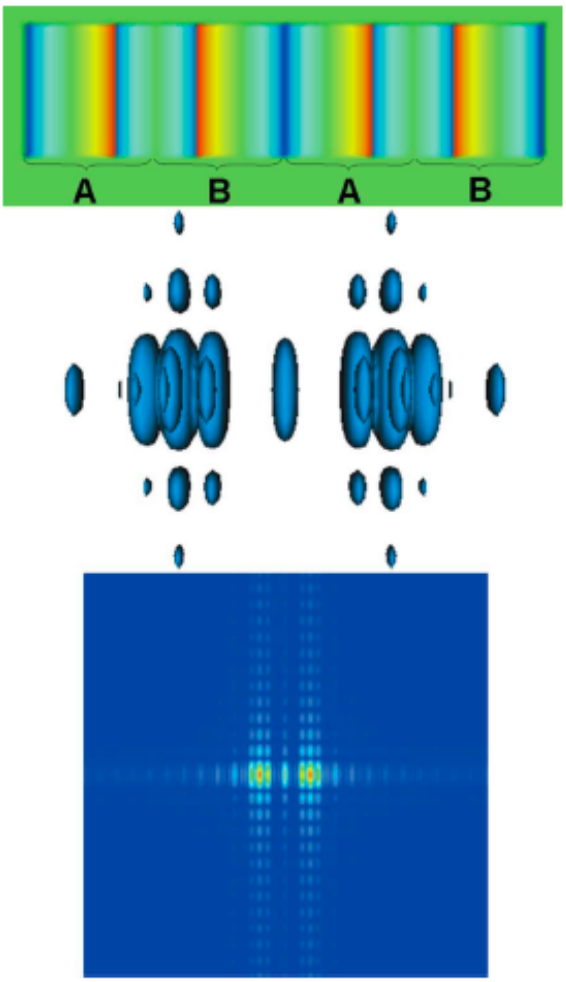

Figure 40 (Top) Twinned crystal with four domains (ABAB) shown as a translucent three-dimensional box with the domain dimensions and phase ramps. (Middle) Calculated three-dimensional coherent diffraction pattern. (Bottom) Isoscalar plane cut of the diffraction pattern showing the speckles within the split peaks[125].

7:4 FEA Simulation of differential-strained Gold Nano crystals induced by thiol adsorption using COMSOL Multiphysics

Finite-Element-Analysis (FEA) studies on strains evolution due to adsorption of thiol particles on both curved and flat surfaces of of gold nano-crystals has been modelled, and experimental results have demonstrated the power of CDI technique for investigation of strains generated by formation of thiol-based self-assembled monolayers (SAM) on the surface of the gold nano-crystal[6]. Fig. 44 has shown the corresponding FEA calculations performed in COMSOL Multiphysics package.

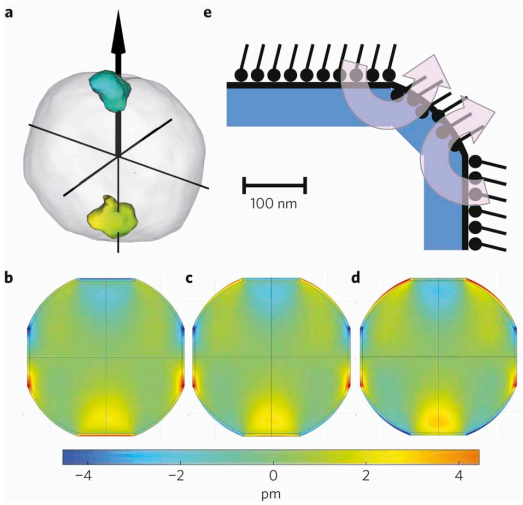

Figure 41 a, Image of the measured crystal with a single contour of the difference density Δρ(r) superimposed, coloured according to its phase. b, Calculated vertical component of the displacements of a model facetted gold nanocrystal with a tensile surface stress σ_S=1.5 N m^{-1} applied to the facets alone. c, The same as in b with a tensile surface stress σ_S=0.75 N m^{-1} applied to the facets and a compressive surface stress σ_S=−0.75 N m^{-1} applied to the spherical surface regions. d, The same as in b with a compressive surface stress σ_S=−1.5 N m^{-1} applied to the spherical surface regions alone. A sphere of radius 145 nm is attached to a skin layer of 5 nm thickness used to apply the stress. Four 40° facets intercept the sphere, also with 5 nm skins. e, Schematic of the relative motions at the nanocrystal surface induced by thiol adsorption: the crystal's flat facets are observed to contract inwards relative to its spherical regions. Figure is from [126]

8. Bragg-geometry Ptychography: theory and applications

8:1 Bragg-geometry ptychography: difficulties and applications

Ptychography, both in forward transmission and far-field Bragg geometries, has demonstrated the ability to solve compact or extended structures with complexity[127-129]. Recent work on studies of magnetic domain structures under evolution of magnetic hysteresis loops by using forward transmission geometry ptychography was reported[130]. The detailed e-PIE[129,131] and difference-map[127,132] ptychographycal algorithms are explained in details. Ptychography is able to solve complex direct-space structures because of the overlap constraints in ptychography is apparently a much stronger constraint when compared to the support constraint in CDI.

The overlap constraint are illustrated in great details in previous work, and the fundamental principle behind the overlap constraint is that the complex wave-function of the direct-space wavefields when incident X-rays illuminates and exits the sample, is the product of the complex X-ray probe wave-function and the complex sample exit-wave-function. This multiplicative relationship acts as direct-space constraint in general ptychography iterative algorithms. The goal is to minimize the discrepancy between the complex wave-function from the inverse Fourier transform of complex diffraction

function in the detector plane (after Fourier-space modulus constraint projection) and the complex wave-function formed by simple multiplication of complex probe function and current object function at each specified position at sample. The minimization procedure results in an update step for both complex probe and object functions. Fig. 45 describes the classical ptychographycal iterative engine from the Rodenburg's earlier work[129].

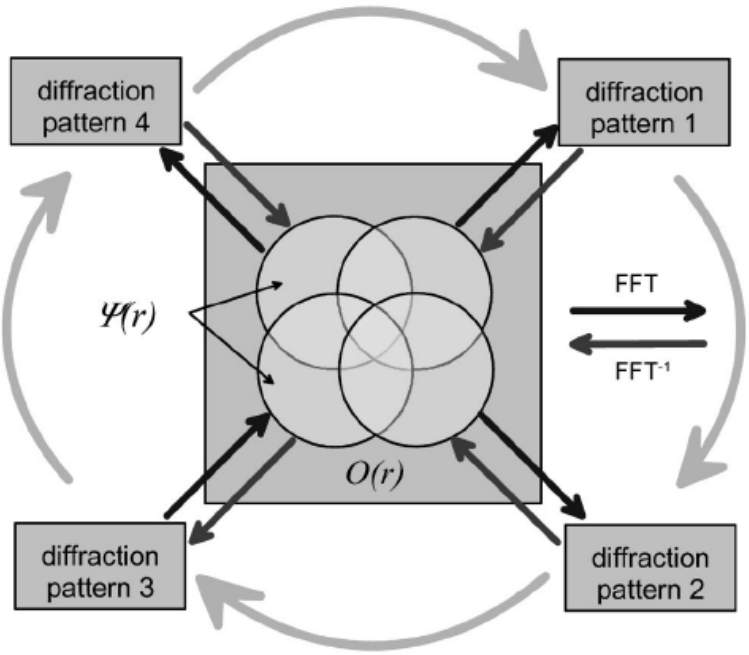

Figure 42 Illustration of the earliest ptychographycal iterative engine. The update of object and probe function is in a sequential order. Image is from[129]

Nevertheless, there is possible a uniqueness problem is still not completely resolved by using better constraint alone, there have been some concerns on accurate reconstructions of phase structures of objects when the probe structures are unknown, because the phase structures of probe and the object can be cancelled out by each other if they both have

linear components. This manifests itself as a phase gradient on the reconstructed image and probe. The phase gradient on the probe will be in the opposite sense to the phase gradient on the image. In chapter 2:3 and 2:4 the uniqueness problem has been discussed in detail. This is simply a symmetry of the solution, rather than a genuine non-uniqueness. To improve the feasibility of successful recovery of both amplitude and phase of measured objects, systematic setups for measurements of probe structures have been developed at the c-SAXS beamline at the Swiss Light Source (SLS). Ptychography with a round region of interest scan (round-ROI)[133] method has been developed and proven to improve data convergence and to reduce ambiguities in data reconstructions. The round_ROI scan is a system of concentric circles with some offset to break the symmetry. Illustration of round_ROI scan and conventional grid scan methods can be found in Fig. 46, with both scan methods having the same number of scanning positions. It is advantageous over conventional rectangular-grid-scan due to its ability to break down translation symmetry that causes the reconstructed object phase to have contributions from the probe. One benefit of the round_ROI scan is that the analytical descriptions of the scan positions can be preserved.

Demonstrations of Bragg-geometry Ptychography have shown the applicability of such technique with high degree of spatial resolution and reliability[102,122,134] . Ptychography, in Bragg geometry has better applications in compact or extended highly crystalline structures with its special emphasis on surface sciences, and three-dimensional atomic

displacements fields can be reconstructed for a single compact isolated structure. Studies on isolated single crystalline structures by Bragg CDI have been investigated by current state-of-art instrumentations at available beamlines worldwide, such as 34-ID-C at Advanced Photon Source (APS) and ID-01 at the European Synchrotron Radiation Facilities (ESRF). By comparison, Bragg-geometry Ptychography is considered advantageous over conventional Bragg CDI because of its much stronger direct-space overlap constraints implemented in the iterative algorithms for reconstructions and its arbitrarily large field of view. Such powerful direct-space constraint could in principle improve experimental data quality by providing abundant two or three-dimensional datasets with relatively high degree of overlapping of datasets, usually between 50 to 80 percent. The overlapping degree has some maximum threshold due to the fact that various kinds of noises are present in experiments and the instrumentation instability, as well as limitation of detectors should be taken into account. For comparison, conventional Bragg CDI has to rely on every single two-dimensional data sections to be of good quality in order to have reliable 2D or 3D reconstruction. Furthermore, Bragg-geometry Ptychography is believed to be much more successful for solving highly strained direct-space structures due to the nature of its data acquisition and algorithms, while such problems remain a difficulty in conventional Bragg CDI though many attempts have shown improvements, and this is discussed in chapter 3 in details. Our group has performed measurements with round-ROI-scan method at 34-ID-C at APS for zeolite crystals and SOI micro-squares. Our initial data show some encouraging results;

however further studies are to be done aiming at better understanding of Ptychography in Bragg-geometry.

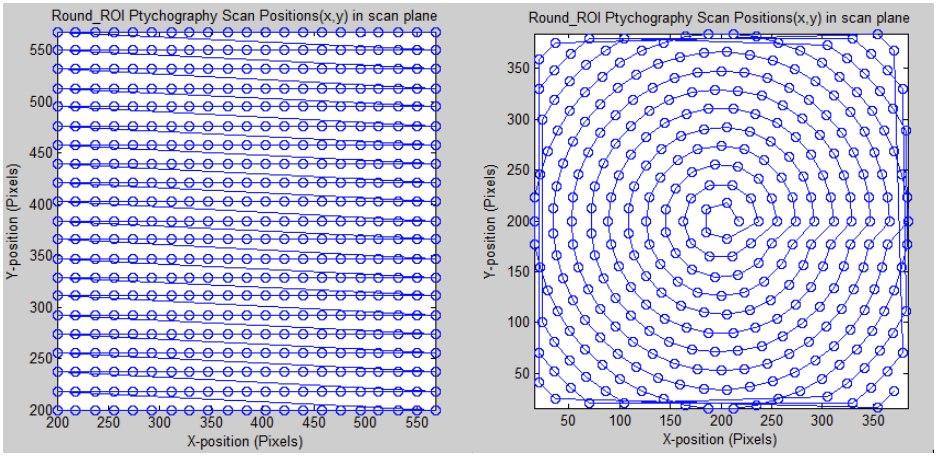

Figure 43 Two types of ptychographical scan methods: left picture represents conventional grid scan; right picture represents round-ROI-scan method. Both scan methods have the same number of scan positions and about the same overlap.

Bragg-geometry Ptychography is a combination of Bragg CDI and scanning X-ray Microscopy, the Bragg-geometry measurements are performed with conventional reflection or Laue geometry Bragg CDI, either 2D Bragg diffraction or 3D Bragg rocking curve, with multiple positions on specimens of particular scanning patterns, usually grid scan or round-ROI-scan type.

Bragg Ptychography in reflection-geometry is different from conventional transmission-geometry Ptychography because the experimental setup geometry is not co-linear comparing to that of its transmission-geometry counterpart. One of the major obstacles for successful data inversion of reflection-geometry Bragg ptychography is the fact that the optical path length difference (OPLD) in Bragg reflection geometry during 2D scans

of ptychographical series are changing during the scan, mainly because the OPLD within specimens under investigation for different 2D scans is different depending on the geometry of the setups, and crystalline orientation etc. i.e. the angles of diffractometer are varying for different 2D scans collection. Fig. 48 shows the detailed illustration of how various ptychographical 2D scans result in different OPLDs, consequently, the probe structures are varying during scans. The larger incidence angles measurements in Bragg reflection geometry would in principle result to smaller variation of OPLD within specimens, while lower incidence angles would lead to bigger OPLD resulting to large phase shifts of X-ray probe within specimens under study. The resulting phase shifts would cause the fluctuation of X-ray probe, which in turn change probe structure according to crystal geometry of Bragg reflection and the orientation of the diffractometer in experiments.

One of the fundamental hypotheses of ptychography is that probe structure is assumed to be constant during 2D scans. To overcome this problem, we have developed modified Bragg-geometry ptychography technique by introducing rotation matrices that transform the ptychographical scanning directions perpendicular to the X-ray beam direction. This modification could manually keep the OPLDs constant when scanning object perpendicular to the beam. Fig. 47-48 shows a modified scanning method that keeps the OPLDS fixed during 2D scans alongside its unmodified counterpart. Our preliminary results show that Bragg-geometry Ptychography on Laue geometry works well for both Zeolite and gold nanocrystals, and the thickness of the crystals studied are around a few

microns, which means the OPLDs are relatively small comparing to that of reflection geometry measurements.

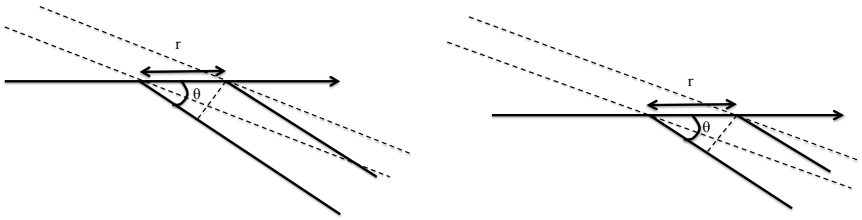

Figure 44 OPLDs for scanning with modification of rotation matrices. The left picture represents OPLD with one position, and the right picture represents OPLD of the next scan. $OPLD = r[1 - \cos(\theta)]$

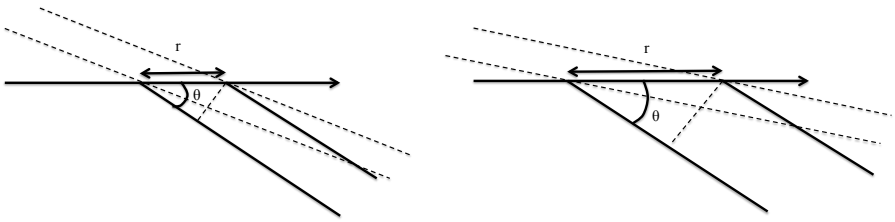

Figure 45 OPLDs for scanning without modification of rotation matrices. The left picture represents OPLD with one position, and the right picture represents OPLD of the next scan. $OPLD = r[1 - \cos(\theta)]$

8.2 Ptychography studies on Siemens-star test sample for solution uniqueness

The uniqueness problem has been a big un-solved problem causing solution ambiguities in conventional CDI technique, in which the X-ray probe structure cannot be reconstructed separately from the objects and where the direct-space constraints have been quite limited, though a number of new advancements of direct-space constraints in CDI have been developed[9,45,46,61]. Ptychography has revolutionized CDI method with which extra overlapping constraints that are applied for much better data convergence mainly due to the highly redundant information that is provided by the datasets. Nevertheless, the uniqueness of the reconstructed solution is still a conceptual problem even in Ptychography, a number of measurements have been performed and the results are illustrated as follows.

Figure 46 Schematic diagram for Siemens-star Test pattern with 36 spokes; sample is made of Tungsten, 1.5 microns thick, for hard X-ray measurements. Fabricated by zoneplates.com, Courtesy Dr. Graeme Morrison, University College London, UK

Transmission geometry Ptychography setup was used to study oversampling and uniqueness theories. The Siemens-star test pattern (Fig. 49) that is used for this investigation is a phase object, from which phase-contrast diffraction data is obtained due to its strong scattering nature. Reconstructions of Siemens-star object with flat phase across all spokes is expected from the sample fabrication procedure, but our preliminary reconstructions show slight variation of phase values over the different spokes due to slight mis-centering and incorrect data pixel alignments in reconstruction procedure. These phase ramps can be arbitrarily removed, as explained above. When measured with 8.9keV energy, absorption contrast is very poor, resulting to poor contrast in reconstructed object amplitude. The following results show phase of reconstructed test object and amplitude of reconstructed X-ray probe. The actual experimental detector to sample distance was set to 550mm, however, incorrect detector to sample distances were entered in data reconstructions to test robustness of solution uniqueness of difference-map algorithm for Ptychography. The measurements were taken by Maria Civita, Nicolas Burdet, Xiaowen Shi, Xiaojing Huang, Ian Robinson at beamline 34-ID-C, Advanced Photon Source in July 2012.

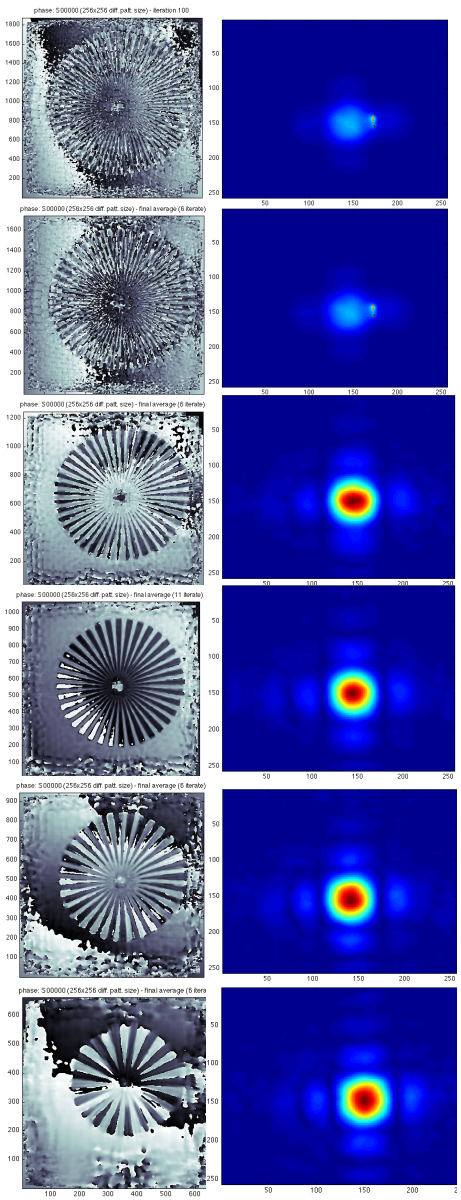

Figure 47 Reconstructed Object phase (left) and probe amplitude (right) for: actual sample-detector distance of 550mm. from top to bottom: incorrect distance of: 275mm, 350mm, 450mm, 550mm, 650mm, 1100mm respectively. Reconstructions were performed with difference-map algorithm, Courtesy Mr. Nicolas Burdet, University College London, UK

The Siemens-star test patterns have almost perfect circular symmetry; and the reconstruction results with artificially chosen detector-to-sample distances in the reconstruction parameter all look real, the number of spokes of the reconstructed Siemens-star vary linearly with entered detector to sample distances, the numbers increase with reducing detector to sample distances in reconstructions. Moreover, most of the reconstructed X-ray probes look real and plausible as well, with a bunch of them looking extremely similar. However, with the reconstructed Siemens-star spokes increasing artificially for smaller detector distances, there is a sudden transition for reconstructed X-ray probe structures, with probe fringes beginning to disappear. Also, the intensity of the reconstructed X-ray probe begins to reduce as well with larger number of spokes for artificially reduced detector distances.

For direct-space objects with high degree of spherical symmetry with round roi scans performed in Ptychography measurements, the uniqueness of the solutions is not guaranteed as our experimental analysis shows. A number of different solutions are obtained with substantial difficulties to distinguish the incorrect reconstructed results with that of the actual correct test pattern if the correct answers are not known in advance when real samples rather than test samples are used. To be able to obtain unique solutions, one has to at least ensure that the sample objects have relatively asymmetric phase structures, or structural X-ray illumination with curved wave front by FCDI technique is used for experimental measurements.

9 Conclusion and Future Outlooks

9:1 BCDI vs. Bragg-geometry Ptychography: what we have learnt

9:1:1 Advantages and difficulties of BCDI

BCDI has the overwhelming advantage for its ability to investigate nano-scale strains, with atomic spacing sensitivity in hard-condensed matter materials, such as gold nanocrystals and silicon nanostructures. This makes BCDI a unique technique for investigating three-dimensional buried structures, with dimensions from a few nm to a few microns, if the coherent X-ray beam bigger than the size of the objects. The maximum achievable spatial resolution for BCDI is estimated to be around 30 nm, though the best achievable spatial resolution for a particular experiment has to be dependent on various sample, instrumentation and detector properties.

BCDI is able to study three-dimensional buried structures without destructive slicing of samples, so that the investigated samples are in their native states. Single isolated structure can be studied by BCDI and separation of signals of sample from substrate can be achieved when the crystallographic orientation or lattice spacing of sample is different from that of the substrate. The measurement time of BCDI is typically short, compared with other three-dimensional imaging techniques, such as Transmission X-ray Microscopy (TXM) and high-resolution electron microscopy (HREM). However, strong oversampling in all three reciprocal-space dimensions enables the possibility of high quality of data reconstructions, for 2D or 3D displacement fields, with 2D or 3D datasets

respectively. Full three-dimensional strain-tensors can be resolved when data is measured for three different Bragg reflections with none coplanar with each other. Newton has demonstrated the power of BCDI for retrieving 3D displacement tensor in a single isolated ZnO nanocrystal[2].

Relative good signal-to-noise (SNR) can be achieved for BCDI if the X-ray beam flux is sufficiently high and the object scattering signal is relatively strong, and these can be easily achieved for strong scattering hard-condensed-matter objects. Nevertheless, biological imaging using CDI in general has more difficulties to overcome mainly due to weak scattering signals and X-ray radiation damage on specimens. Some aspects of radiation damage have been discussed in chapter 4.

Time-resolved BCDI is able to study in situ evolution of various structures under external conditions, such as excitation by laser beam, the pump-probe experiment. Pico-second X-ray pulses have been achieved in 3rd generation synchrotron sources, while femto-second X-ray pulse has been available in X-ray free electron laser facilities worldwide, in both soft and hard energy regime.

There are still many difficulties associated with BCDI and CDI in general. BCDI is not capable of studying extended objects, when objects are bigger than the beam. Also, X-ray beam structure can not be resolved by using BCDI, therefore, in general, BCDI is only reliable for investigation of objects that are much smaller than the beam, for which case

the beam structure within object has negligible phase curvature and relatively uniform amplitude, which can be considered to be relatively flat[24].

Beside, strong direct-space constraints are lacking in BCDI, when diffraction intensities tend to be relatively asymmetric, some a priori information is required[9,45,135], usually in the form of a well-defined support, for data reconstruction to converge. For FCDI, initial knowledge of X-ray beam profile is needed[5] for correct data reconstructions.

Difficulties arise when studying objects which are highly strained, the reconstructions often fail due to solutions becoming stagnated at incorrect local minima of the two spaces, direct and reciprocal-space of datasets. Because of the propagation non-uniqueness effect (discussed in Chapter 3), extra constraints are needed to arrive at correctly-focused solutions, which would typically require additional knowledge of either amplitude or phase of studied specimens.

No reconstruction convergence is guaranteed for BCDI or CDI in general with the current suite of algorithms. The nature on whether two spaces, both direct and reciprocal parts are convex is fundamentally difficult to determine.

For high spatial resolution of BCDI, much higher flux density is required, where 3rd generation synchrotron sources have limited coherent flux density. The trade-off between radiation effect and maximum obtainable scattering angle signal is important, especially

in the field of biological imaging. This is discussed in details because it is related to radiation damage in chapter 4.

9:1:2 Advantages and difficulties of Bragg-geometry ptychography

Ptychography, has overwhelming advantage of its ability of providing redundant information due to its strong overlapping direct-space redundancy in the experiment. Both e-PIE and difference-map algorithms are able to retrieve complex X-ray probe structures simultaneously with complex objects. It is able to investigate extended structures, without limits on spatial sizes in principle, in 2D. 3D structures can be studied when combining conventional ptychography with tomography, which is becoming called "Ptycho-tomo". Because its ability to retrieve X-ray probe separately from the object wave function, various kinds of X-ray illumination structures can be used depending on nature of particular measurement to enable better convergence. Recent work has found small advantages form optimising the choice of illumination[136].

However, certain ambiguities occur for structural determination of both X-ray probe and object, because the simple multiplicative relationship between probe and object. Poor choice of probe, sample or scan pattern can provoke factorisation artefacts. This may impose limits on types of structures to be studied, and associated ambiguities are discussed in details in chapter 8.1.

Due to its overlapping constraint nature, time-resolved ptychography is technologically challenging because sample structures can be changing during one set of ptychographical acquisition for a single dataset. Furthermore, radiation damage may cause sample

structures to evolve, and the amount of radiation damage is different for different positions on samples due to different prior doses. This disadvantage of ptychography is particularly important for soft biological specimens, where tolerance of radiation damage is extremely low comparing that of hard-condensed-matter specimens. While Stability issues are always important, they are especially limiting when data acquisition time is long.

Development of 3D ptychography[137] with multi-slice approach has shown promising applications in materials sciences. Future development of 3D ptychographical techniques can be vital for understanding structures/morphologies of 3D materials, of course, without limitations of sizes.

9:2 Developments of Bragg-geometry Ptychography

Our newly developed Guided-Phase Error Reduction (GPER) algorithm has been proven to improve significantly the data convergence of reconstructions of diffraction patterns of highly strained SOI nanowires caused by X-ray radiation-induced bending. Simulations show that there are significant improvements on convergence. Further developments have been made to utilize this algorithm to solve reconstructions of experimental data with highly strained features, and we used our simulated model of direct-space phase values to guide reconstructions of real data and successful inversions have been obtained.

In the future, we plan to measure strain patterns of SiGe nanowires and quantum dot based FET transistors by using nano-focused X-ray beam Bragg geometry ptychography technique at beamline 34-ID-C at APS. The CDI method removes various aberration effects of a conventional lens-based system, it uses iterative algorithms to retrieve phase information lost during measurement, and is therefore sensitive to internal strains associated in nanostructure systems with phase-contrast imaging technique. It can provide us with shape information and quantitative strain measurements of the internal structures of single crystalline micro- and nanostructures. Combining conventional CDI with coherent scanning X-ray microscopy, i.e. ptychography with nano-focused beam studies enable us to directly extract structures of X-ray beam and our patterned SiGe nanowires within FET devices. Circular scans with nano-focused beam with around 100nm X 100nm focus spot should enable us to achieve appropriate degree of

overlapping of the scanning patterns, thus reconstructions of two-dimensional amplitude and displacements of our Silicon-On-Insulator wires can be attempted, reconstruction of beam profile can be performed in the mean time. We plan to develop algorithms that are suitable for reconstructions of three-dimensional Bragg-geometry ptychography studies on isolated compact object.

We propose to perform circular scans with a circular Fresnel zone-plate (FZP), with a focusing spot of around 100nm X 100nm, and appropriate guard and standard pinholes; slits will be placed before X-ray beam entering the FZP to make the beam coherent. The selected region of the zone-plate will be calculated with knowledge of the transverse coherence lengths of X-rays at beamline 34-ID-C or other relevant beamlines at APS. Measurements on our individual SiGe nanowires and quantum dots within devices of dimensions of around 400μm X 400μm X 160nm, with 50% to 70% degree of overlapping of two-dimensional Bragg diffraction patterns will be attempted. High-accuracy piezo-electric motor stage setup is required to accurately monitor the scanning positions in both dimensions of the plane perpendicular to the X-ray beam propagation direction. Reconstructions of density and phase of both the SOI crystal and probe will be studied by extended ptychographic iterative engine (ePIE). Suitable attenuation and a beamstop will be used in this proposed experiment. Both transmission and Bragg reflection geometries are to be employed. Our previous measurements on transmission geometry have been analyzed and our reconstruction results have shown very useful

information. An appropriate detector should be used depending on experimental setups and the purposes of measurements for specific objects.

We envisage our model-guided method can be applied to various structures/systems with interesting physical and chemical properties. Simulations studies are to be used to have some rough estimation of strain mechanisms. These will be used as references to guide data inversion in CDI and related techniques. Other simulations methods such as boundary element method (BEM)[138] as well as FEA are important for understanding deformation and mechanical breakdown of nano-scale systems caused by various kinds of external factors, such as mechanical stress; high heat; high pressure and electrical or magnetic fields.

The new emerging technique of X-ray free electron laser has been attracting enormous interests and attentions in the past a few years, both in the soft[63] and hard X-ray energy regimes[139,140]. The question of whether the use of femto-second X-ray pulses could reduce radiation damage substantially comparing to that of longer pulses is one of the main issues determining the future research direction of single macro-molecular imaging with state-of-art XFEL sources worldwide. A recent study[67] has shown that the usage of sub-pico second X-ray pulses produce very similar results in macromolecular crystallographic reconstructions comparing to that of much longer pulses, indicating that the underlying mechanism of damage is not having a big effect between 5fs and 200fs. This may suggest that the goal of X-ray free electron lasers for atomic resolution single

macro-molecular imaging, both in theory and experiments are promising. If experiments can reproduce what is predicted in theory successfully, the conclusion can be a significant milestone for solving complex structures of materials of scientific interests, both for soft and hard condensed-matter-physics.

9:3 Future Experiments

Lattice mismatches in materials in general can cause epitaxial strains, either in the tensile or compressive form[141], which is usually determined by the elastic properties of the materials and the direction of the normal forces applied. Compressive strains and tensile strains can be generated when the normal forces are exerted inwards or outwards on materials respectively. Fig. 51 illustrates typical lattice mismatch behaviour, where the arrows pointing at the direction of displacement of atoms caused by the epitaxial strains. In the example shown, the effect of mismatch between the substrate and the film lattice constants causes a lateral compression force, straining the film. Its Poisson ratio then determines the amount of expansion of the film lattice out of plane. The resulting strain exists throughout the film, so long as it remains less than a critical thickness.

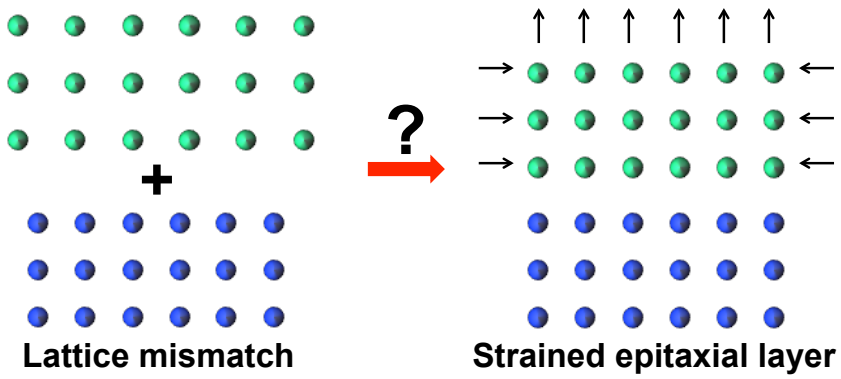

Figure 48 Schematic diagram for illustration of strains generation of epitaxial layer caused by lattice mismatch. Courtesy Dr. Sanliang Ling, Department of Physics and Astronomy, University College London, UK

It is recognized that semiconductor device carrier mobility can be substantially improved with applications of strain-technology, which is a crucial step for performance improvements in Silicon-based semiconductor devices. It has been found that strains induced in Silicon-based devices during fabrication processes can result in enhanced channel mobility[91]. Furthermore, it was reported that Silicon nanowires down to 10nm x 20nm cross-sections with doping can exhibit substantial improvements of thermoelectric efficiency compared to bulk Silicon devices at various temperatures[142]. Band gaps of strained nano-sized semiconductors can be modified[143] and strained Silicon band gaps have been theoretically predicted to switch from indirect to direct[144]. This might advance device performance by the reduction of operating voltage to reduce the amount of heat dissipation across devices, and might even one day lead to the creation of Si light-emitting diode (LED).

Studies on porous Silicon nanowires devices and SiGe core-shell nanowire-based Nanowire-Field-Effect-Transistors are to be performed in the near future for obtaining both quantitative and precise information on structural or morphological dependence on performances of various nanostructure semiconductor devices, which are crucial elements aiming at better understanding of the nature of Silicon nanostructure based devices with improved comprehension of quantum confinements in various dimensions. Recent

studies show SiGe cylindrical core-shell nanowire based NWFETs demonstrate significant improvements on electron/hole charge carriers mobility and device efficiency[145]. We hope by using our novel Bragg CDI and two or three-dimensional pychography techniques, further studies could be vital for pinpointing underlying mechanisms that are responsible for these observed improvements. This may open a new path for direct-observation and in situ characterisation of nanostructure semiconductor devices ranging from sensors and optoelectronic devices.

Reference and Notes

1 Robinson, I. & Harder, R. Coherent X-ray diffraction imaging of strain at the nanoscale. *Nat Mater* 8, 291-298, doi:10.1038/nmat2400 (2009).

2 Marcus C. Newton, Steven. J. Leake., Ross Harder and Ian K. Robinson. Three-dimensional imaging of strain in a single ZnO nanorod. *Nature Materials* 9, 120-124, doi:10.1038/nmat2607 10.1038/NMAT2607 (2009).

3 Jianwei Miao, P. C., Janos Kirz & Sayre, D. Extending themethodology of X-ray crystallography to allow imaging of micrometre-sized non-crystalline specimens. *Nature* 400, 342-344 (1999).

4 Pfeifer, M. A., Williams, G. J., Vartanyants, I. A., Harder, R. & Robinson, I. K. Three-dimensional mapping of a deformation field inside a nanocrystal. *Nature* 442, 63-66, doi:10.1038/nature04867 (2006).

5 Williams, G. *et al.* Fresnel Coherent Diffractive Imaging. *Physical Review Letters* 97, doi:10.1103/PhysRevLett.97.025506 (2006).

6 Usuda, K., Numata, T., Irisawa, T., Hirashita, N. & Takagi, S. Strain characterization in SOI and strained-Si on SGOI MOSFET channel using nano-beam electron diffraction (NBD). *Materials Science and Engineering: B* 124-125, 143-147, doi:10.1016/j.mseb.2005.08.062 (2005).

7 Robinson, I. Imaging matter in different spaces. *Physics* 4, doi:10.1103/Physics.4.22 (2011).

8 Abbey, B. *et al.* Keyhole coherent diffractive imaging. *Nature Physics* 4, 394-398, doi:10.1038/nphys896 (2008).

9 A. A.Minkevich, E. F., T.Slobodskyy, M.Riotte, D.Grigoriev, T.Metzger, A.C.Irvine,V.Novák, V.Holý, T.Baumbach, . Strain field in (Ga,Mn)As/GaAs periodic wires revealed by coherent X-ray diffraction. *EPL (Europhysics Letters)* 94, 66001, doi:10.1209/0295-5075/94/66001 (2011).

10 Williams, G. J. Microscopy of Au Microcrystals by Coherent X-Ray Diffractive Imaging. *PhD thesis* (2004).

11 Steven J. Leake, Marcus C. Newton, Ross Harder and Ian K. Robinson. Longitudinal coherence function in X-ray imaging of crystals. *OPTICS EXPRESS* 17, 15853-15859 (2009).

12 Clark, J. N., Huang, X., Harder, R. & Robinson, I. K. High-resolution three-dimensional partially coherent diffraction imaging. *Nat Commun* 3, 993 doi:10.1038/ncomms1994 (2012).

13 Nugent, K. A. Coherent methods in the X-ray sciences. *Advances in Physics* 59, 1-99, doi:10.1080/00018730903270926 (2010).

14 Vartanyants, I. *et al.* Coherence Properties of Individual Femtosecond Pulses of an X-Ray Free-Electron Laser. *Physical Review Letters* 107, doi:10.1103/PhysRevLett.107.144801 (2011).

15 Quiney, H. M. Coherent diffractive imaging using short wavelength light sources. *Journal of Modern Optics* 57, 1109-1149, doi:10.1080/(2010).

16 From lecture notes from Dissemination of IT for the Promotion of Materials Science (DoITPoMS), University of Cambridge, **http://www.doitpoms.ac.uk/**

17 Marchesini, S. *et al.* X-ray image reconstruction from a diffraction pattern alone. *Physical Review B* 68, doi:10.1103/PhysRevB.68.140101 (2003).

18 Center for X-ray Optics and Advanced Light Source, L. B. N. L. X-RAY DATA BOOKLET.

19 Elements of Modern X-ray Physics, By Jens Als-Nielsen and Des McMorrow, John Wiley & Sons, Ltd.

20 Ariel Lipson, S. G. L., Henry Lipson. Optical Physics. *Cambridge University Press.* 4th edition.

21 C. Scheringer, X-ray Bragg scattering in the Born-Oppenheimer approximation, Acta Cryst. (1979). A35, 340-342

22 J. L. Libbert, J. A. P. a. I. K. R. Asymmetric Fraunhofer Diffraction from Roller-Blade Slits. *Journal of Synchrotron Radiation* 4, 125-127 (1997).

23 VLIEG, M. L. A. E. Angle Calculations for a Six-Circle Surface X-ray Diffractometer. *J. A.ppL Cryst.* 26, 706-716 (1993).

24 Loren Beitra, Moyu Watari, Takashi Matsuura, Naonobu Shimamoto Ross & Robinson, H. a. I. Confocal Microscope Alignment of Nanocrystals for Coherent Diffraction Imaging. *AIP Conf. Proc.* 1234, 57-60, doi:10.1063/1.3463273 (2010).

25 Schroer, C. Focusing hard x rays to nanometer dimensions using Fresnel zone plates. *Physical Review B* 74, doi:10.1103/PhysRevB.74.033405 (2006).

26 Hidekazu Mimura, S. H., Takashi Kimura, Hirokatsu Yumoto, Daisuke Yamakawa,, Hikaru Yokoyama, S. M., Kouji Inagaki, Kazuya Yamamura, Yasuhisa Sano, & Kenji Tamasaku, Y. N., Makina Yabashi, Tetsuya Ishikawa and Kazuto Yamauchi. Breaking the 10 nm barrier in hard-X-ray focusing. *Nature Physics* 6, 122-125, doi:10.1038/nphys1457 10.1038/NPHYS1457 (2010).

27 I.L. Karle, H. Hauptman, J. Karle and A.B. Wing, Crystal and Molecular Structure of p,p'-Dimethoxybenzophenone by the Direct Probability Method. *Acta Cryst.* 11, 257-263 (1958).

28 GABOR, D. A New Microscopic Principle. *Nature* 161, 777-778 (1948).

29 Gabor, D. Microscopy by Reconstructed Wave-Fronts. *Proceedings of the Royal Society A: Mathematical, Physical and Engineering Sciences* 197, 454-487, doi:10.1098/rspa.1949.0075 (1949).

30 MULVEY, M. E. H. A. T. The Formation of the Diffraction Image with Electrons in the Gabor Diffraction Microscope. *Journal of the Optical Society of America* 42, 763-769 (1952).

31 Saxton, R. W. G. a. W. O. A Practical Algorithm for the Determination of Phase from Image and Diffraction Plane Pictures. *Optik* 35, 237-246 (1972).

32 Thibault, P. Pierre Thibault_PhD_Thesis_2007. *PhD thesis* (2007).

33 J. Miao, J. K. a. D. S. The oversampling phasing method. *Acta Crystallographica Section D; Biological Crystallography* D56, 1312-1315 (2000).

34 C. E. Shannon, "Communication in the presence of noise", Proc. Institute of Radio Engineers, vol. 37, no. 1, pp. 10–21, Jan. 1949. Reprint as classic paper in: Proc. IEEE, vol. 86, no. 2, (Feb. 1998)

35 D., S. Some implications of a theorem due to Shannon. *Acta Cryst.* 5, 843 (1952).

36 E. M. Hofstetter, Construction of time-limited functions with specified auto-correlation functions, *IEEE Transactions on Information Theory* 10, 119 (1964).

37 A. M. J. Huiser, A. J. J. Drenth, and H. A. Ferwerda, On phase retrieval in electron-microscopy from image and diffraction pattern, *Optik* 45, 303 (1976)

38 A. M. J. Huiser, and H. A. Ferwerda, On the problem of phase retrieval in electron microscopy from image and diffraction pattern. 2. Uniqueness and stability., *Optik* 46, 407 (1976)

39 Song, C. *et al.* Phase retrieval from exactly oversampled diffraction intensity through deconvolution. *Physical Review B* 75, doi:10.1103/PhysRevB.75.012102 (2007).

40 R. H. T. Bates, Fourier phase problems are uniquely solvable in more than one dimension 1. underlying theory, *Optik* 61, 247 (1982)

41 R. H. T. Bates, Uniqueness of solutions to two-dimensional Fourier phase problems for localized and positive images, *Computer Vision Graphics and Image Processing* 25, 205 (1984)

42 John C.H. Spence, M. H., L.D. Marks, J. Miao. Lensless imaging- a workshop on ‘‘new approaches to the phase problem for non-periodic objects’’. *Ultramicroscopy* 90, 1-6 (2001).

43 Pierre Thibault, V. E., Chris Jacobsen, David Shapiro and David Sayre. Reconstruction of a yeast cell fromX-ray diffraction data. *Acta Crystallographica Section A* A62, 248-261 (2006).

44 Rodenburg, J. M. The phase problem, Microdiffraction and Wavelength-limited resolution- A Discussion, *Ultramicroscopy* 27, 413-422 (1989).

45 Huang, X., Harder, R., Xiong, G., Shi, X. & Robinson, I. Propagation uniqueness in three-dimensional coherent diffractive imaging. *Physical Review B* 83, doi:10.1103/PhysRevB.83.224109 (2011).

46 Newton, M., Harder, R., Huang, X., Xiong, G. & Robinson, I. Phase retrieval of diffraction from highly strained crystals. *Physical Review B* 82, doi:10.1103/PhysRevB.82.165436 (2010).

47 Unpublished work done by Bean et al, London Centre for Nanotechnology, University College London, U.K.

48 Dilanian, R. A. *et al.* Coherent diffractive imaging: a new statistically regularized amplitude constraint. *New Journal of Physics* 12, 093042, doi:10.1088/1367-2630/12/9/093042 (2010).

49 Huang, X., Harder, R., Leake, S., Clark, J. & Robinson, I. Three-dimensional Bragg coherent diffraction imaging of an extended ZnO crystal. *J Appl Crystallogr* 45, 778-784, doi:10.1107/S0021889812018900 (2012).

50 Elser, V. Phase retrieval by iterated projections. *J. Opt. Soc. Am. A* 20, 40-55 (2003).

51 Fienup, J. R. Phase retrieval algorithms-a comparison. *Applied Optics* 21, 2758-2769 (1982).

52 Wackerman, J. R. F. a. C. C. Phase-retrieval stagnation problems and solutions. *Optical Society of America* 3, 1897-1907 (1986).

53 Martin Kohl, A. A. M., and Tilo Baumbach. Improved success rate and stability for phase retrieval by including randomized overrelaxation in the hybrid input output algorithm. *Optics Express* 20, 17093-17106 (2012).

54 Harder, R., Liang, M., Sun, Y., Xia, Y. & Robinson, I. K. Imaging of complex density in silver nanocubes by coherent x-ray diffraction. *New Journal of Physics* 12, 035019, doi:10.1088/1367-2630/12/3/035019 (2010).

55 Miao, J. *et al.* Three-Dimensional GaN-Ga2O3 Core Shell Structure Revealed by X-Ray Diffraction Microscopy. *Physical Review Letters* 97, doi:10.1103/PhysRevLett.97.215503 (2006).

56 Nugent, K., Peele, A., Chapman, H. & Mancuso, A. Unique Phase Recovery for Nonperiodic Objects. *Physical Review Letters* 91, doi:10.1103/PhysRevLett.91.203902 (2003).

57 H. M. Quiney, K. A. N., A. G. Peele. Iterative image reconstruction algorithms using wave-front intensity and phase variation. *Optics Letters* 30, 1638-1640 (2005).

58 Brian Abbey, L. W. W., Harry M. Quiney, David J. Vine, Guido A. Cadenazzi,, Clare A. Henderson, K. A. N., Eugeniu Balaur, Corey T. Putkunz, Andrew G. Peele, & McNulty, G. J. W. a. I. Lensless imaging using broadband X-ray sources. *Nature Photonics* 5, 4, doi:10.1038/nphoton.2011.125 10.1038/NPHOTON.2011.125 (2011).

59 H. M. Quiney, K. A. N., and A. G. Peele. Iterative image reconstruction algorithms using wave-front intensity and phase variation. *Opt. Lett.* 30, 1638-1640 (2005).

60 Yanjun Li and Emil Wolf, Focal shifts in diffracted converging spherical waves. *Optics Communications* 39, 211-215 (1981).

61 Newton, M. Compressed sensing for phase retrieval. *Physical Review E* 85, doi:10.1103/PhysRevE.85.056706 (2012).

62 Thibault, P. & Guizar-Sicairos, M. Maximum-likelihood refinement for coherent diffractive imaging. *New Journal of Physics* 14, 063004, doi:10.1088/1367-2630/14/6/063004 (2012).

63 Chapman, H. N. *et al.* Femtosecond diffractive imaging with a soft-X-ray free-electron laser. *Nature Physics* 2, 839-843, doi:10.1038/nphys461 (2006).

64 Howells, M. R. *et al.* An assessment of the resolution limitation due to radiation-damage in x-ray diffraction microscopy. *J Electron Spectros Relat Phenomena* 170, 4-12, doi:10.1016/j.elspec.2008.10.008 (2009).

65 A. Rose, in Advances in Electronics, L. Marton, (Ed Vol. 1, 131–166, New York, 1948.

66 Qun Shen, I. B. a. P. T. Diffractive imaging of nonperiodic materials with future coherent X-ray sources. *J. Synchrotron Rad.* 11, 432-438 (2004).

67 Boutet, S. *et al.* High-resolution protein structure determination by serial femtosecond crystallography. *Science* 337, 362-364, doi:10.1126/science.1217737 (2012).

68 Howells, M. R., Hitchcock, A. P. & Jacobsen, C. J. Introduction: Special issue on radiation damage. *Journal of Electron Spectroscopy and Related Phenomena* 170, 1-3, doi:10.1016/j.elspec.2009.01.004 (2009).

69 Richard Neutze, R. W., David van der Spoel, Edgar Weckert & Hajdu, J. Potential for biomolecular imaging with femtosecond X-ray pulses. *Nature* 406, 752-757 (2000).

70 Jacobsen, T. B. a. C. Soft X-ray radiation-damage studies in PMMA using a cryo-STXM. *J. Synchrotron Rad.* 10, 280-283 (2002).

71 Zheng, Y. *et al.* Investigation of Radiation Damage in Stainless steel, Tungsten and Tantalum by Heavy Ion Irradiations. *Nuclear Physics A* 834, 761c-763c, doi:10.1016/j.nuclphysa.2010.01.139 (2010).

72 Busby, S. J. Z. a. J. T. Structural materials for fission & fusion energy. *materials today* 12, 12-19 (2009).

73 Ackland, G. Materials science. Controlling radiation damage. *Science* 327, 1587-1588, doi:10.1126/science.1188088 (2010).

74 Ye, B. *et al.* Irradiation effects in UO2 and CeO2. *Journal of Nuclear Materials*, doi:10.1016/j.jnucmat.2012.09.035 (2012).

75 Stoller, R. E. Primary Radiation Damage Formation. 293-332, doi:10.1016/b978-0-08-056033-5.00027-6 (2012).

76 Drude, Paul . "Zur Elektronentheorie der metalle". Annalen der Physik 306 (3): 566 (1900)

77 Drude, Paul "Zur Elektronentheorie der Metalle; II. Teil. Galvanomagnetische und thermomagnetische Effecte". Annalen der Physik 308 (11): 369 (1900)

78 Todoroki, A., Samejima, Y., Hirano, Y. & Matsuzaki, R. Piezoresistivity of unidirectional carbon/epoxy composites for multiaxial loading. *Composites Science and Technology* 69, 1841-1846, doi:10.1016/j.compscitech.2009.03.023 (2009).

79 Michael Mayer, O. P. a. H. B. Complete set of piezoresistive coefficients of CMOS -diffusion. *J. Micromech. Microeng.* 8, 158-160 (1998).

80 Xu, H. *et al.* Effects of Shell Strain on Valence Band Structure and Transport Properties of Ge/Si1-xGexCore–Shell Nanowire. *Japanese Journal of Applied Physics* 49, 04DN01, doi:10.1143/jjap.49.04dn01 (2010).

81 Xu Hong-Hua(许洪华), L. X.-Y. 刘., He Yu-Hui(何毓辉),, Fan Chun(樊春), D. G. 杜., Sun Ai-Dong(孙爱东), & Han Ru-Qi(韩汝琦), a. K. J.-F. 康. Valence band variation in Si (110) nanowire induced by a covered insulator. *Chin. Phys. B* 19, 014601-014601-014605 (2010).

82 Chu, M., Sun, Y., Aghoram, U. & Thompson, S. E. Strain: A Solution for Higher Carrier Mobility in Nanoscale MOSFETs. *Annual Review of Materials Research* 39, 203-229, doi:10.1146/annurev-matsci-082908-145312 (2009).

83 Ma, J.-L. *et al.* Valence band structure and hole effective mass of uniaxial stressed Germanium. *Journal of Computational Electronics* 10, 388-393, doi:10.1007/s10825-011-0374-7 (2011).

84 Murphy-Armando, F. & Fahy, S. Giant piezoresistance in silicon-germanium alloys. *Physical Review B* 86, doi:10.1103/PhysRevB.86.035205 (2012).

85 Jooyoung Song, B. Y., Weize Xiong and Yuan Taur. Gate-Length-Dependent Strain Effect in n- and p-Channel FinFETs. *IEEE Transactions on Electron Devices*, 56, 533-536 (2009).

86 Chan, C.-H. *et al.* Optical characterization of InAlAs/InGaAs metamorphic high-electron mobility transistor structures with tensile and compressive strain. *Thin Solid Films*, doi:10.1016/j.tsf.2012.03.060 (2012).

87 Chen, F. *et al.* Conduction band structure and electron mobility in uniaxially strained Si via externally applied strain in nanomembranes. *Journal of Physics D: Applied Physics* 44, 325107, doi:10.1088/0022-3727/44/32/325107 (2011).

88 Kobayashi, M., Cai, J. & Haensch, W. On the high-field transport and its temperature dependence in deca-nanometer fully depleted silicon-on-insulator field-effect-transistor. *Applied Physics Letters* 99, 092104, doi:10.1063/1.3626849 (2011).

89 US 2012/0001228 A1, Pub. Date: Jan.5, 2012

90 Murray, C. E. *et al.* Nanoscale silicon-on-insulator deformation induced by stressed liner structures. *Journal of Applied Physics* 109, 083543, doi:10.1063/1.3579421 (2011).

91 Ieong, M., Doris, B., Kedzierski, J., Rim, K. & Yang, M. Silicon device scaling to the sub-10-nm regime. *Science* 306, 2057-2060, doi:10.1126/science.1100731 (2004).

92 Henry, M. D., Shearn, M. J., Chhim, B., Scherer, A. Ga+beam lithography for nanoscale silicon reactive ion etching. *Nanotechnology* 21, 245303, doi:10.1088/0957-4484/21/24/245303 (2010).

93 Drake, T. S., M.L. Lee, A.J. Pitera,. E.A. Fitzgerald, D.H. Anjum, J. Li, N.K. R. Hull, and J.L. Hoyt, . Fabrication of Ultra-Thin Strained Silicon on Insulator. *Journal of Electronic Materials* 32, 972-975 (2003).

94 Jaju, V. in *Advances in MOSFETs EE530* (2004).

95 Fujioka, H. Method of manufacturing semiconductor on insulator. (1991).

96 Bich-Yen Nguyen, G. C., and Carlos Mazuré. A Review of SOI Technology and its Applications. *Journal Integrated Circuits and Systems* 4, 51-54 (2009).

97 B. Aspar, M. B., H. Moriceau, C. Maleville, T. Poumeyrol, A.M. Papon. Basic mechanisms involved in the Smart-Cut process. *Microelectronic Engineering* 36, 233-240 (1997).

98 Shi, X., Xiong, G., Huang, X., Harder, R. & Robinson, I. K. Structural inhomogeneity in silicon-on-insulator probed with coherent X-ray diffraction. *Zeitschrift für Kristallographie* 225, 610-615, doi:10.1524/zkri.2010.1354 (2010).

99 Xiong, G. *et al.* Elastic relaxation in an ultrathin strained silicon-on-insulator structure. *Applied Physics Letters* 99, 114103, doi:10.1063/1.3637634 (2011).

100 Cha, W. *et al.* Exploration of crystal strains using coherent x-ray diffraction. *New Journal of Physics* 12, 035022, doi:10.1088/1367-2630/12/3/035022 (2010).

101 Loren Beitra, M. W., Takashi Matsuura, Naonobu Shimamoto Ross Harder and Ian Robinson. Confocal Microscope Alignment of Nanocrystals for Coherent Diffraction Imaging. *AIP Conference Proceedings* CP1234, 57-60 (2010).

102 Godard, P. *et al.* Three-dimensional high-resolution quantitative microscopy of extended crystals. *Nat Commun* 2, 568, doi:10.1038/ncomms1569 (2011).

103 Polvino, S. M. *et al.* Synchrotron microbeam x-ray radiation damage in semiconductor layers. *Applied Physics Letters* 92, 224105, doi:10.1063/1.2942380 (2008).

104 Prohászka, J., Mamalis, A. G. & Gaál, Z. The cause of the uncertainty of the elastic limit. *CIRP Journal of Manufacturing Science and Technology* 2, 70-74, doi:10.1016/j.cirpj.2009.09.002 (2009).

105 Namatsu, H., Kurihara, K., Nagase, M., Iwadate, K. & Murase, K. Dimensional limitations of silicon nanolines resulting from pattern distortion due to surface tension of rinse water. *Applied Physics Letters* 66, 2655, doi:10.1063/1.113115 (1995).

106 Willoughby, J. C. M. a. A. F. W. Fracture of Silicon Wafers. *Journal of Crystal Growth* 85, 83-90 (1987).

107 Olson, C. R., Kuryliw, E., Jones, B. E. & Jones, K. S. Effect of stress on the evolution of mask-edge defects in ion-implanted silicon. *Journal of Vacuum Science & Technology B: Microelectronics and Nanometer Structures* 24, 446, doi:10.1116/1.2162566 (2006).

108 Y. L. Tsai and J. J. Mecholsky, J. Fractal fracture of single crystal silicon. *J. Mater. Res* 6, 1248-1263 (1991).

109 Griffith, A. A. The Phenomena of Rupture and Flow in Solids. *Philosophical Transactions of the Royal Society A: Mathematical, Physical and Engineering Sciences* 221, 163-198, doi:10.1098/rsta.1921.0006 (1921).

110 J.L.Demenet, J. R. a. On a change in deformation mechanism in silicon at very high stress: new evidences. *Scripta Materialia* 45, 1259-1265 (2001).

111 Castaing, J, Veyssiere, P., Kubin, L.P., and Rabier, J. The plastic deformation of silicon between 300°C and 600°C, (1981) *Philos Mag A* 44, 1407

112 Jacques, V. *et al.* Bulk Dislocation Core Dissociation Probed by Coherent X Rays in Silicon. *Physical Review Letters* 106, doi:10.1103/PhysRevLett.106.065502 (2011).

113 Williams, G., Pfeifer, M., Vartanyants, I. & Robinson, I. Three-Dimensional Imaging of Microstructure in Au Nanocrystals. *Physical Review Letters* 90, doi:10.1103/PhysRevLett.90.175501 (2003).

114 Xiaowen Shi, G. X., Xiaojing Huang, Ross Harder & Robinson, a. I. Radiation-induced bending of silicon-on-insulator nanowires probed by coherent x-ray diffractive imaging. *New Journal of Physics* 14, 13, doi:10.1088/1367-2630/14/6/063029 (2012).

115 D K Saldin, R. J. H., V L Shneerson and W Moritz. Phase retrieval methods for surface x-ray diffraction. *J. Phys.: Condens. Matter* 13, 10689-10707 (2001).

116 Gang Xiong, X. H., Steven Leake, & Marcus C Newton, R. H. a. I. K. R. Coherent x-ray diffraction imaging of ZnO nanostructures under confined illumination. *New Journal of Physics* 13, 11, doi:10.1088/1367-2630/13/3/033006 (2010).

117 Jesse N. Clark, C. T. P., Evan K. Curwood, David J. Vine, & Robert Scholten, I. M., Keith A. Nugent,and Andrew G. Peele. Dynamic sample imaging in coherent diffractive imaging. *Optics Letters* 36, 1954-1956 (2011).

118 J. S. Barnard, J. S., J. R. Tong, P. A. Midgley. High-Resolution Three-Dimensional Imaging of Dislocations. *Science* 313, 319 (2006).

119 Van Swygenhoven, H., Derlet, P. M. & Froseth, A. G. Stacking fault energies and slip in nanocrystalline metals. *Nat Mater* 3, 399-403, doi:10.1038/nmat1136 (2004).

120 Dash, W. C. Evidence of Dislocation Jogs in Deformed Silicon. *Journal of Applied Physics* 29, 705, doi:10.1063/1.1723255 (1958).

121 Eymery, J. *et al.* Dislocation strain field in ultrathin bonded silicon wafers studied by grazing incidence x-ray diffraction. *Physical Review B* 65, doi:10.1103/PhysRevB.65.165337 (2002).

122 S. O.Hruszkewycz, M. V. H., C. E.Murray, J.Bruley, J.Holt, A.Tripathi, O. G.Shpyrko, I.McNulty, M. J.Highland, P. H.Fuoss, . Quantitative Nanoscale Imaging of Lattice Distortions in Epitaxial Semiconductor Heterostructures Using Nanofocused X-ray Bragg Projection Ptychography. *Nano Lett*, doi:10.1021/nl303201w (2012).

123 Xiang, J. *et al.* Ge/Si nanowire heterostructures as high-performance field-effect transistors. *Nature* 441, 489-493, doi:10.1038/nature04796 (2006).

124 Ionizing Radiation Effects in MOS Devices and Circuits T. P. Ma (Editor), Paul V. Dressendorfer (Editor) ISBN: 978-0-471-8489-6

125 Aranda, M. A. *et al.* Coherent X-ray diffraction investigation of twinned microcrystals. *J Synchrotron Radiat* 17, 751-760, doi:10.1107/S0909049510039774 (2010).

126 Moyu Watari, Rachel A. McKendry, Manuel Vögtli, Gabriel Aeppli, Yeong-Ah Soh, Xiaowen Shi, Gang Xiong, Xiaojing Huang, Ross Harder and Ian K. Robinson. Differential stress induced by thiol adsorption on facetted nanocrystals. *Nature Materials*, 862–866, doi:10.1038/nmat3124 10.1038/NMAT3124 (2011).

127 Thibault, P. *et al.* High-resolution scanning x-ray diffraction microscopy. *Science* 321, 379-382, doi:10.1126/science.1158573 (2008).

128 Dierolf, M. *et al.* Ptychographic X-ray computed tomography at the nanoscale. *Nature* 467, 436-439, doi:10.1038/nature09419 (2010).

129 Rodenburg, J. *et al.* Hard-X-Ray Lensless Imaging of Extended Objects. *Physical Review Letters* 98, doi:10.1103/PhysRevLett.98.034801 (2007).

130 Tripathi, A. *et al.* Dichroic coherent diffractive imaging. *Proc Natl Acad Sci U S A* 108, 13393-13398, doi:10.1073/pnas.1104304108 (2011).

131 Maiden, A. M. & Rodenburg, J. M. An improved ptychographical phase retrieval algorithm for diffractive imaging. *Ultramicroscopy* 109, 1256-1262, doi:10.1016/j.ultramic.2009.05.012 (2009).

132 Thibault, P., Dierolf, M., Bunk, O., Menzel, A. & Pfeiffer, F. Probe retrieval in ptychographic coherent diffractive imaging. *Ultramicroscopy* 109, 338-343, doi:10.1016/j.ultramic.2008.12.011 (2009).

133 Dierolf, M. *et al.* Ptychographic coherent diffractive imaging of weakly scattering specimens. *New Journal of Physics* 12, 035017, doi:10.1088/1367-2630/12/3/035017 (2010).

134 Berenguer de la Cuesta, F. *et al.* Coherent X-ray diffraction from collagenous soft tissues. *Proc Natl Acad Sci U S A* 106, 15297-15301, doi:10.1073/pnas.0905151106 (2009).

135 Minkevich, A. *et al.* Selective coherent x-ray diffractive imaging of displacement fields in (Ga,Mn)As/GaAs periodic wires. *Physical Review B* 84, doi:10.1103/PhysRevB.84.054113 (2011).

136 Guizar-Sicairos, M. *et al.* Role of the illumination spatial-frequency spectrum for ptychography. *Physical Review B* 86, doi:10.1103/PhysRevB.86.100103 (2012).

137 A. M. Maiden, M. J. Humphry, and J. M. Rodenburg. Ptychographic transmission microscopy in three dimensions using a multi-slice approach. *J. Opt. Soc. Am. A* 29, 1606-1614 (2012).

138 Murray, C. E. *et al.* Probing strain at the nanoscale with X-ray diffraction in microelectronic materials induced by stressor elements. *Thin Solid Films*, doi:10.1016/j.tsf.2012.05.043 (2012).

139 Young, L. *et al.* Femtosecond electronic response of atoms to ultra-intense X-rays. *Nature* 466, 56-61, doi:10.1038/nature09177 (2010).

140 Chapman, H. N. *et al.* Femtosecond X-ray protein nanocrystallography. *Nature* 470, 73-77, doi:10.1038/nature09750 (2011).

141 Cao, J. & Wu, J. Strain effects in low-dimensional transition metal oxides. *Materials Science and Engineering: R: Reports* 71, 35-52, doi:10.1016/j.mser.2010.08.001 (2011).

142 Boukai, A. I. *et al.* Silicon nanowires as efficient thermoelectric materials. *Nature* 451, 168-171, doi:10.1038/nature06458 (2008).

143 Ki-Ha Hong, Jongseob Kim, Sung-Hoon Lee, and Jai Kwang Shin. Strain-Driven Electronic Band Structure Modulation of Si Nanowires. *Nano Lett* 8, 6 (2008).

144 Zhao, X., Wei C. M., Yang, L. & Chou, M. Y. Quantum Confinement and Electronic Properties of Silicon Nanowires. *Physical Review Letters* 92, 236805, doi:10.1103/PhysRevLett.92.236805 (2004).

145 Xiang, J. *et al.* Ge/Si nanowire heterostructures as high-performance field-effect transistors. *Nature* 441, 489-493, doi:10.1038/nature04796 (2006).

Appendex

(1) C code for COMSOL to pythonphasing conversion:

```
/*****************************************/
/* This includes all the necessary files */
/*****************************************/
#include "sp4util.h"
#include <stdio.h>
#include <math.h>


/*********************************************/
/* reads x,y,phase format file and outputs sp4 */
/*********************************************/

ERRORCODE Txt3DToSp4Ian2
(
   Sp4Array* NewSp4,
   Sp4Array* tempSp4,
   char* filename
)

{
uint32_t
nn[3],ndim,i,IndexIm,IndexRe,iterator,ix,iy,iz,size1,size2,size3,
index;
double Imag;
FILE *file;
ERRORCODE err;
file=fopen(filename,"r");
char s[100];
char *token;

/*
while(fgets(s,10,file)!=NULL)
    printf("%s\n",s);
    printf("stringlength %d\n",strlen(s));
*/
i=0;
while(fgets(s,1024,file)!=NULL)
           {
     //printf("%s stringlength %d\n",s,strlen(s));
     token=strtok(s," ");
```

```
      //printf(" x coord: %s",token);
      token=strtok(NULL," ");
      //printf(" y coord: %s",token);
      token=strtok(NULL," ");
      //printf(" z coord: %s",token);
      token=strtok(NULL," ");
      /* IndexRe=(i)*2;
      IndexIm=(i)*2+1; */
      Imag=atof(token);
      //printf("%s %10.2f %5d \n",token,Imag,i);
      //tempSp4->data[i*2]=Imag;
      //tempSp4->data[i*2+1]=Imag;
      tempSp4->data[i*2]=Imag;
      /* tempSp4->data[i*2+1]=1.0*sin(Imag); */
      //printf("phase %s\n",token);
      //printf("i %d noElements %d\n",i,NewSp4->nelements);
      i+=1;
      }

//printf("%i",tempSp4->nelements);

//printf("find the seg fault");

fclose(file);
Sp4ArraySave(tempSp4, "temp2.sp4");
size1=NewSp4->nn[0];
size2=NewSp4->nn[1];
size3=NewSp4->nn[2];

//printf("size1, size2, size 3 (%i,%i,%i)",size1,size2,size3);

iterator=0;

for(ix=0; ix <NewSp4->nn[0]; ix++)
  for(iy=0; iy < NewSp4->nn[1]; iy++)
    for(iz=0; iz < NewSp4->nn[2]; iz++)
       {
       index = 2*(iz+size3*(iy+size2*ix));
    if (tempSp4->data[iterator*2] == 0.0)
    {
     NewSp4->data[index]   = 0.;
                NewSp4->data[index+1] = 0.;
    }
    else
    {
            NewSp4->data[index]   = 1.0*cos(tempSp4-
>data[iterator*2]);
                NewSp4->data[index+1] = 1.0*sin(tempSp4-
```

```
>data[iterator*2]);




    }

    iterator+=1;

    }



return SUCCESS;

}
```

(2) C code for simulation of 3D Gaussian amplitude of X-ray probe function

```
/*****************************************/
/* This includes all the necessary files */
/*****************************************/
#include "sp4util.h"
#include <stdio.h>
#include <math.h>
//#include <myFunction.h>



/*********************************************/
/* reads x,y,phase format file and outputs sp4 */
/*********************************************/

ERRORCODE Txt3DToSp4Ian5
(
   Sp4Array* NewSp4,
   Sp4Array* tempSp4
//   char* filename
)

{
uint32_t
nn[3],ndim,i,ic,IndexIm,IndexRe,iterator,ix,iy,iz,size1,size2,siz
e3,index,index2;
double Imag, phase1;
//FILE *file;
ERRORCODE err;
//file=fopen(filename,"r");
char s[100];
char *token;
double g_sigma = 80.00;
Sp4Array in_local;
Sp4Array* in;
Sp4Array gauss;
Sp4Array tempSp4b;
uint32_t n=tempSp4->nelements;
uint32_t i_iter;
uint32_t i_1;
uint32_t i_2;
uint32_t i_3;
```

```
uint32_t n_iter;
double sum=0.0;



size1=NewSp4->nn[0];
size2=NewSp4->nn[1];
size3=NewSp4->nn[2];


Sp4ArrayInitAsOther(&gauss,NewSp4);
for(i_3=0;i_3<size3; i_3++)
{
    for(i_2=0;i_2<size2; i_2++)
    {
     for(i_1=0;i_1<size1; i_1++)
     {
                        index=2*(i_3+size3*(i_2+size2*i_1));



                       gauss.data[index] = ((double) 1.0
*exp(((0.8660254*i_3+0.5*i_1)-
((0.8660254*size3+0.5*size1)/2))*((0.8660254*i_3+0.5*i_1)-
((0.8660254*size3+0.5*size1)/2))/(-2*g_sigma*g_sigma)));


           gauss.data[index+1]=0.0;
                     //}
                       // }
     //    sum+=gauss.data[index];

     }
    }
}

Sp4ArraySave(&gauss, "gauss.sp4");


Sp4ArraySave(tempSp4, "temp.sp4");


//printf("size1, size2, size 3 (%i,%i,%i)",size1,size2,size3);

iterator=0;

for(ix=0; ix <NewSp4->nn[0]; ix++)
```

```
  for(iy=0; iy < NewSp4->nn[1]; iy++)

    for(iz=0; iz < NewSp4->nn[2]; iz++)

       {

       index = 2*(iz+size3*(iy+size2*ix));

phase1=atan2(tempSp4->data[index+1], tempSp4->data[index]);

                          NewSp4->data[index] =((tempSp4-
>data[index] * gauss.data[index])

                          NewSp4->data[index+1] = ((tempSp4-
>data[index] * gauss.data[index+1])) + ((tempSp4->data[index+1] *
gauss.data[index]));









    iterator+=1;

//



        }

return SUCCESS;

}
```

(3) Matlab Code for GPHIO algorithm

```
if strcmp(ALG,'GPHIO')

    phi_max=max(params.phase_range);
    phi_min=min(params.phase_range);

    ph=angle(pnm);   %phase after modulus constraint


    %angle1=angle(pnm);
    %angle2=angle(pn);
    %anglen=angle(pn);
    ph_m=params.model_phase;   %model phase

    supportph=( ph < (ph_m+phi_max) & ph > (ph_m+phi_min ) );

    supportgp=support.*double(supportph); %create new support
from old one and ph

    pn= ((pnm.*supportgp)+(1-supportgp).*(pn-beta*pnm));


end
```

(4) Matlab Code for GPER algorithm

```
if strcmp(ALG,'GPER')

    phi_max=max(params.phase_range);
    phi_min=min(params.phase_range);

    ph=angle(pnm);   %phase after modulus constraint
    ph2=angle(pn);

    %angle1=angle(pnm);
    %angle2=angle(pn);
    %anglen=angle(pn);
    ph_m=params.model_phase;   %model phase

    %supportph=( ph < (ph_m+phi_max) & ph > (ph_m+phi_min ) );

    %supportgp=support.*double(supportph); %create new support
from old one and ph

    ind = find((ph - ph_m) > phi_max);
    %ph2(ind) = ph(ind);
    ph2(ind) = ph_m(ind) + phi_max;

    ind2 = find((ph - ph_m) < phi_min);
    %ph2(ind2) = ph(ind2);
    ph2(ind2) = ph_m(ind2) + phi_min;

    ind3=  find((ph - ph_m) > phi_min & (ph - ph_m) < phi_max);

    ph2(ind3) = ph(ind3);
```